Online Fault Diagnosis Techniques for Interturn Short-Circuits in Switched Reluctance Motors

A Thesis Submitted

in Partial Fulfilment of the Requirements

for the Degree of

DOCTOR OF PHILOSOPHY

by

Mahetab Alam

(2018EEZ0009)

DEPARTMENT OF ELECTRICAL ENGINEERING

INDIAN INSTITUTE OF TECHNOLOGY ROPAR

MARCH, 2024

Mahetab Alam: *Online Fault Diagnosis Techniques for Interturn Short-Circuits in Switched Reluctance Motors*

Dedicated to My Family

Declaration of Originality

I hereby declare that the work which is being presented in the thesis entitled **Online Fault Diagnosis Techniques for Interturn Short-Circuits in Switched Reluctance Motors** has been solely authored by me. It presents the result of my own independent investigation/research conducted during the time period from August 2018 to July 2023 under the supervision of Dr Saifullah Payami, Assistant Professor, Indian Institute of Technology Ropar. To the best of my knowledge, it is an original work, both in terms of research content and narrative, and has not been submitted or accepted elsewhere, in part or in full, for the award of any degree, diploma, fellowship, associateship, or similar title of any university or institution. Further, due credit has been attributed to the relevant state-of-the-art and collaborations with appropriate citations and acknowledgments, in line with established ethical norms and practices. I also declare that any idea/data/fact/source stated in my thesis has not been fabricated/ falsified/ misrepresented. All the principles of academic honesty and integrity have been followed. I fully understand that if the thesis is found to be unoriginal, fabricated, or plagiarized, the Institute reserves the right to withdraw the thesis from its archive and revoke the associated Degree conferred. Additionally, the Institute also reserves the right to appraise all concerned sections of society of the matter for their information and necessary action (if any). If accepted, I hereby consent for my thesis to be available online in the Institute's Open Access repository, inter-library loan, and the title & abstract to be made available to outside organizations.

Mahtab
Signature

Name: Mahetab Alam
Entry Number: 2018eez0009
Program: PhD
Department: Electrical Engineering
Indian Institute of Technology Ropar
Rupnagar, Punjab 140001

Date: 4|3|2024

Acknowledgement

I take this opportunity to acknowledge my heartfelt gratitude to all those people who directly or indirectly helped me to carry out this research work successfully. I am heartily thankful to my supervisor, Dr. Saifullah Payami, whose encouragement, guidance and support through out my research work enabled me to develop an understanding of the subject. I appreciate his sincere help in terms of contributions of time, ideas so as to make my Ph.D. experience stimulating and productive. The joy and enthusiasm that he has for his research was contagious and motivational for me, even during tough times in the Ph.D. pursuit. I express my gratitude for his willingness to help and timely advices on issues, even beyond the scope of doctoral studies.

I would like to acknowledge the financial, academic and technical support of the Indian Institute of Technology Ropar for this research. I am sincerely grateful to Dr. C.C Reddy, Dr. A. V Raviteja, Dr. Kalaiselvi. J and Dr. S.S. Padhee for assessing the work and giving invaluable suggestions as members of Doctoral committee.

The members of the Power Group have contributed immensely to my personal and professional time during my stay in the institute. The group has been a source of friendships as well as good advice and collaboration. I especially thank Mr. Vaibhav Shah, Mr. Zeeshan Rayeen, Mr. Baibhav Gupta, Mr. Abdul Azeem, Mr. Digamber Kumar, Mr. Manish Kumar, and Mr. Gautam Kumawat for their valuable advices during my course of research and personal life. I would like to express gratitude to the services being offered by Mr. Dilbag, Mr. Jaspreet and Mr. Devendra staff of power electronics and machine laboratory of Electrical Engineering department. Last but not the least I would like to thank my family, my parents who educated me, for always believing in my capabilities and for encouraging me to pursue my dreams.

Certificate

This is to certify that the thesis entitled **Online Fault Diagnosis Techniques for Interturn Short-Circuits in Switched Reluctance Motors**, submitted by **Mahetab Alam (2018eez0009)** for the award of the degree of **Doctor of Philosophy** of Indian Institute of Technology Ropar, is a record of bonafide research work carried out under my guidance and supervision. To the best of my knowledge and belief, the work presented in this thesis is original and has not been submitted, either in part or full, for the award of any other degree, diploma, fellowship, associateship or similar title of any university or institution.

In my opinion, the thesis has reached the standard fulfilling the requirements of the regulations relating to the Degree.

Saifullah

Signature of the Supervisor
Dr Saifullah Payami
Electrical Engineering
Indian Institute of Technology Ropar
Rupnagar, Punjab 140001
Date: 4 March 2024

Abstract

Fault diagnosis is crucial to any electric drive system, ensuring their reliable operation. The significance of fault ride-through capability, which denotes the ability of an electric motor to endure faults and maintain operational integrity, is of paramount importance. For this objective, the first step involves the application of fault diagnosis methods to identify any motor fault precisely at the incipient stage. With the increasing demand for rare-earth free alternatives to traditional motors, switched reluctance motors (SRMs) have gained significant attention in different applications due to their specific features. However, to make this technology more commercially available, the different aspects, such as their designs, control strategies, and mitigation of acoustic noise and torque ripples, have been extensively researched, leaving behind the area of fault diagnosis relatively. Interturn short circuits (ITSCs), accounting for 21% of all the electrical faults inside any machine, are responsible for catastrophic failures leading to a complete winding short circuit if left unchecked due to the generation of local hotspots. The inherent problems of torque ripple, noise and vibrations associated with SRMs are also escalated when the machine is subjected to ITSCs. These faults are even difficult to diagnose as the fault features are least apparent in the electrical parameters in ITSC of fewer turns. Also, most of the diagnosis techniques for ITSCs in SRMs suffer from several issues, like lower sensitivity where the system can not detect ITSC if a lower number of turns are short-circuited. Also, there are interference of load variation on the detection reliability in which the fault index might initiate false alarm without any fault. Some of the methods are dependent on the control strategy on which the motor is operating. The thesis delves into an attempt to devise sophisticated online fault diagnosis techniques for ITSCs, considering the research gap in the existing literature. Three online diagnosis techniques have been formulated and validated experimentally on a test rig of four-phase 8/6 SRM. The first method targets low and medium-speed applications operating under chopped current control with 4% least severity detected. The second method is based on the signal injection technique applicable to the SRMs independent of control strategies. It is capable detecting ITSC of 2 turns. The third technique eliminates the additional hardware used for diagnosing the fault utilized in the second method and is also independent of the control strategies. All the techniques have been tested under different operating conditions (load/speed variations) and also under transient conditions, proving the robustness of the proposed schemes. The background, formulation and experimental results of all the schemes are discussed in detail in the subsequent chapters of the thesis.

Keywords: Online fault diagnosis; switched reluctance motors; interturn short circuits (ITSC); sensitivity; detection reliability; signal injection

List of Publications

Journals

1. M. Alam, N. Gugulothu and S. Payami, “A Novel Diagnosis Method for Interturn Short-Circuits in SRMs by Tracking Post Turn-Off Phase Currents Under Current Chopping Control,” in *IEEE Transactions on Industrial Electronics*, vol. 71, no. 1, pp. 49-58, Jan. 2024, doi: 10.1109/TIE.2023.3243297.

2. M. Alam and S. Payami, “A Novel Control-Independent Online Fault Diagnosis of Interturn Short Circuits in SRMs Using Signal Injection Technique,” in *IEEE Transactions on Industrial Electronics*, vol. 70, no. 3, pp. 2157-2167, March 2023, doi: 10.1109/TIE.2022.3169709.

3. M. Alam and S. Payami, ”Diagnosis of Interturn Short-Circuits in SRMs by High-Frequency Switching of Phases Amid Low-Torque Unaligned Rotor Positions,” in *IEEE Transactions on Industrial Electronics*, vol. 70, no. 8, pp. 7537-7546, Aug. 2023, doi: 10.1109/TIE.2023.3241386.

Conferences

1. Alam, M. Shah, V. Payami, S.: “Online Fault Diagnosis of Static and Dynamic Eccentricity in Switched Reluctance Motors using Park Vector Algorithm,” *IET Conference Proceedings*, pp. 885-889, doi: 10.1049/icp.2021.1055 IET Digital Library.

2. V. Shah, M. Alam and S. Payami, ”A Novel Direct Torque Control Scheme for High-Speed Control of Switched Reluctance Motor Using 4-Level Torque Controller,” *The 10th International Conference on Power Electronics, Machines and Drives (PEMD 2020)*, Online Conference, 2020, pp. 966-971, doi:10.1049/icp.2021.0974.

3. V. Shah, M. Alam and S. Payami, ”High Torque/Ampere Direct Torque Control of Switched Reluctance Motor Drives,” *2019 National Power Electronics Conference (NPEC)*, Tiruchirappalli, India, 2019, pp. 1-6, doi: 10.1109/NPEC47332.2019.9034777.

Patents

1. M. Alam, S. Payami,” SYSTEM AND METHOD OF IDENTIFYING AND LOCATING FAULTS IN SWITCHED RELUCTANCE MACHINE”, Indian Patent Application No: 202111040046, Filing Date: 03/09/2021.

2. S. Payami, M. Alam,” SYSTEM AND METHOD FOR DIAGNOSING FAULT IN SWITCHED RELUCTANCE MOTORS”, Indian Patent Application No: 202111007144, Filing Date: 19/02/2021.

3. M. Alam, S. Payami, A. Iqbal ,” ONLINE FAULT DIAGNOSIS TECHNIQUE

FOR INTER-TURN FAULTS IN SWITCHED RELUCTANCE MACHINES", US Provisional Patent No: 63425525, Filing Date: 2022.

Contents

List of Figures

List of Tables

Nomenclature

ω	Angular speed.
θ	Rotor position.
D	Duty ratio.
f_{inj}	Frequency of injected voltage.
I_{av}	Average current.
i_{peak}	Peak of the high-frequency/pulsed current.
i_{pulse}	Instantaneous value of the pulse current.
I_{rms}	RMS current.
L_{eff}	Effective inductance of the faulty phase.
L_f	Inductance of the shorted turns.
L_{hh}	Inductance of the remaining healthy turns.
L_h	Inductance in healthy condition.
L_z	Phase inductance ($z \rightarrow A$ to D phases).
M	Mutual inductance.
N	Speed in rpm.
N_{ph}	Total number of turns.
P_c	Copper loss.
S_{ITSC}	Severity of ITSC.
T	Pulse period.
T_{load}	Load torque.
T_m	Maximum torque.
v_{inj}	Injected voltage.
δN_{ph}	Total number of shorted turns.
$\mathcal{R}$	Reluctance.
ϕ_h	Flux linked by remaining normal/healthy turns.
τ_h	Time constant around aligned position under healthy condition.

τ_{ITSC}	Time constant around aligned position under faulty condition.
θ_a	Aligned rotor position.
θ_r	Inductance regain period after the end of saturation to unsaturated condition.
θ_u	Unaligned rotor position.
θ_{off_z}	Turn-off angle($z\rightarrow$ A to D phases).
θ_{offset}	Offset angle after phase turn-off ensuring appropriate region for tracking.
$\triangle T_f$	Post-fault torque ripple.
$\triangle T_h$	Pre-fault torque ripple.
I_{sat}	Current saturation limit.
i_s, i_{sp}	Currents in the shorted-turns and shorted path.
I_t	Tracking current initial.
i_z	Phase winding currents ($z\rightarrow$ A to D phases).
L_a	Aligned inductance under healthy condition.
L_{ITSC}	Aligned inductance under faulty condition.
N_h	Remaining normal/healthy turns.
$peak_h$	Peak value of the counter under healthy condition.
$peak_{ITSC}$	Peak value of the counter under faulty condition.
R_{ITSC}	Phase resistance under faulty condition.
R_{ph}	Phase resistance under healthy condition.
T_{elec}	Electromagnetic torque.
t_f	Phase current fall time.
t_{hz}	Pulse duration corresponding to the target decay time for healthy condition ($z\rightarrow$ A to D phases).
t_{ITSC-z}	Pulse duration corresponding to the target decay time for faulty condition ($z\rightarrow$ A to D phases).
t_r	Phase current rise time.
V_{dc}	DC link voltage.
W	Magnetic co-energy.
x	Threshold voltage.
y	Threshold factor.

Chapter 1

Introduction & Literature Review

1.1 Introduction

Electric motors have found extensive application in several sectors like industrial and transportation systems since their invention many years ago. During their early usage, the safety measures mainly comprised very basic components aimed at ensuring operational safety. However, as human society progressed, the consistent and reliable functioning of these motors became a fundamental requirement. However, electric motors are often operated in harsh environments, increasing the likelihood of different faults occurring within the motor. Typically, these malfunctions are irreversible and can extend the impact to the motor drives, resulting in additional harm to other components. Using electric motors for safety-critical purposes becomes unfeasible without effectively managing these faults. It is especially concerning given that even minor issues in such contexts can yield substantial financial repercussions. Electric motors must maintain their stable performance even under fault conditions. Consequently, the capacity to withstand faults and continue operating, known as fault ride-through capability, holds immense importance. Owing to this objective, the initial step involves the application of fault diagnosis methods to identify any motor fault precisely at the early stage. Subsequently, tolerant strategies must be implemented to prevent unmanageable breakdowns and mitigate the potential for significant financial setbacks. Integrating fault diagnosis and fault tolerance strategies is a significant approach to enhancing the ability of motors to endure and recover from faults while operating. This thesis investigates the fault diagnosis techniques for inter-turn short circuits (ITSCs) in switched reluctance motors (SRMs), which would help devise tolerant strategies or take appropriate remedial actions at the right time.

SRMs have gained significant attention in various applications, such as green energy harvesting, household appliances, and hybrid electric vehicles. This popularity is mainly because they are easy to manufacture and cost-effective due to the lack of magnets and windings on the rotor [1–3]. SRMs are operated in a magnetic saturation region to ensure optimal performance, making their control more complex. One key advantage of SRMs is their fault tolerance due to phase in-dependency, enabling them to continue operating at reduced performance even under faulty conditions [4]. However, SRMs face certain challenges such as excessive noise, vibrations, and torque ripple, even when in a healthy condition. These issues become more pronounced when the machine experiences fault [5].

As a result, it is not always recommended to use SRMs under faulty conditions. Therefore, fault diagnosis is crucial to detect problems, enabling prompt remedial action to overcome failure. Compared to conventional AC motors, SRMs have received limited attention in the area of fault diagnosis, as most research has focused on developing control strategies and methods to reduce torque ripple. On the other hand, fault diagnosis for conventional AC motors, like induction motors (IMs), has matured over decades of research.

In SRMs, faults can be majorly classified into two types: those in the power electronic converter and those inside the motor itself. When there are issues with the power electronics components, it leads to converter failures, and various diagnosis techniques are available in the literature to address these problems [6–8]. Motor body faults can be divided into two categories: electrical faults, such as open and short circuits in the stator windings, and mechanical faults, like eccentricity and bearing failures. Stator winding failure is a more common fault and can significantly impact the performance of SRM if left unchecked. Short circuit faults (SCFs) can cause more severe damage than open-circuit faults (OCFs). In short circuits of fewer turns/inter-turn short circuits that account for approximately 21% of the faults in any machine, local hotspots are created within the winding due to circulating currents, leading to an increase in the internal temperature of the motor along with the escalation of inherent issues in SRMs. If this fault is not addressed, it can lead to irreversible failure by damaging the faulty phase winding. Hence, diagnosing ITSC at an early stage is very critical so that remedial action can be taken.

This chapter details the basics of SRMs, prominent faults and their effects on the motor performance, and literature on inter-turn short circuits and their diagnosis techniques. An exhaustive literature comparing the existing fault diagnosis technique for conventional motors and SRMs is also included to highlight the necessity of intensive research concerning the faults in SRMs.

1.1.1 Characteristics & Control Strategies of SRMs

Various types of electric motors have been explored for their suitability in industrial and automotive applications. Recently, permanent magnet (PM) machines, including brush-less DC machines, surface-mounted permanent magnet synchronous machines (SM-PMSM), and interior PMSMs (IPMSM) with different magnetic configurations (axial and radial flux), have gained popularity in various applications [9–12]. PM machines offer advantages that make them the top choice for electrified transportation. However, the availability of permanent magnet resources is limited, and their prices are rising, primarily due to supply chain issues and increasing demand from industries like automotive and other sectors [13]. Consequently, price-sensitive markets like electric bikes, scooters, and electric vehicles (EVs) seek to avoid the price fluctuations of neodymium and other rare-earth metals. While ferrite permanent magnets provide a lower-cost and more stable supply alternative, they only offer about one-third of the residual magnetic flux compared to high-energy magnets. Besides, they are prone to demagnetization in the field weakening region [14]. Therefore, there is a rising interest in rare earth-free motors.

Due to their sturdy construction and affordability, SRMs are considered strong contenders for e-bike and e-scooter power trains [15]. Their uncomplicated rotor design makes them suitable for cost-effective, high-speed applications like vacuum cleaners and air blowers. SRMs are also known for their ability to function in harsh environments, making them valuable for initiating and providing secondary electrical power in more electric aircraft engines [16]. However, performance, compactness, and minimal noise are crucial in passenger vehicles. Although numerous research articles propose SRM designs with torque and power density comparable to traditional IPMSMs, there has not been a single commercially available electrified passenger vehicle with an SRM drive, except for prototypes [17, 18]. This underscores the need for further development in this category of the motor.

Table 1.1: Comparison of electric motor performances

	SM PMSM	**IPMSM**	**IM**	**SyncRel**	**SyncRel (Ferrite)**	**SyncRel (NdFeB)**	**SRM**
Speed (rpm)	1500	1500	1497	1500	1500	1500	1500
I_{ph-pk} (A)	100	100	100	100	100	100	100
T_{avg} (Nm)	126.56	130.47	95	91.26	102.22	114.52	91.85
T_{ripple} in %	12.9	14.3	10.5	16.9	15.1	17.8	45
pf	0.88	0.90	0.76	0.70	0.79	0.91	0.65
$V_{ph-peak}$ (V)	150	152	125	137	135	131	100

Table 1.1 lists the comparison of electric motors based on different parameters [19]. The axial length of the motors is the same (84 mm). All the models are excited with

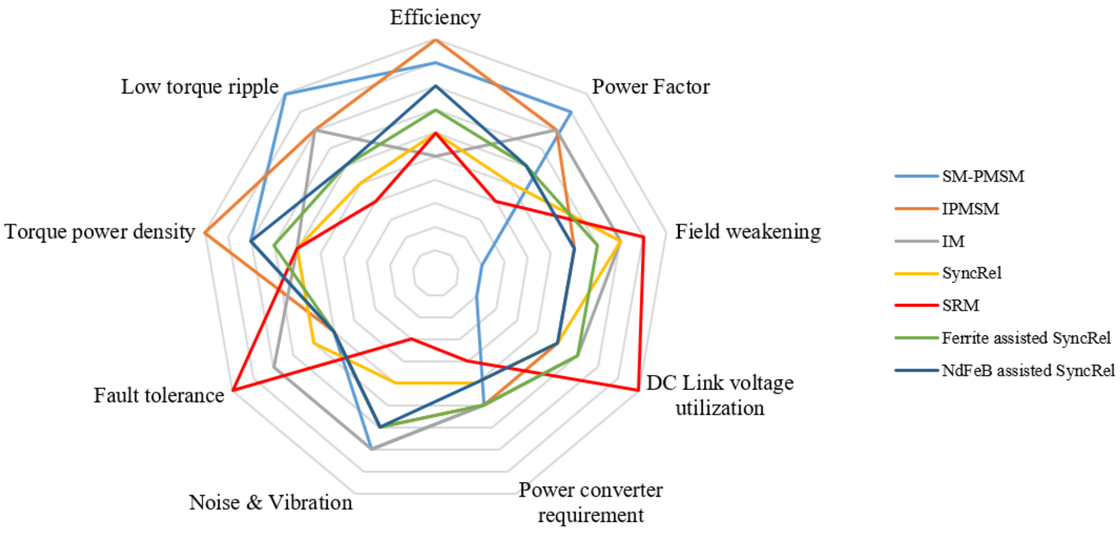

Figure 1.1: Comparison of electric motors based on different indices.

a current density of 6 A/mm^2. SRM produces 70% of IPMSM torque with a 45% torque ripple. Also, the power factor of the SRM is very low. A more comprehensive comparison based on the nine indices for the specifications mentioned above is depicted in Figure 1.1. PM-assisted motors have a higher efficiency due to excitation by the magnet. Due to additional copper losses in the rotor, IMs have lower efficiency than reluctance types. SRMs have superior fault-tolerant features due to their robust rotor structure and modular windings compared to PM-assisted motors. Non-reluctance types have low noise and vibration due to homogeneous force distribution on the stator. Due to non-homogeneous radial field density, SRMs exhibit the highest noise and vibration levels. They also have a comparatively high torque pulsation. An unconventional type of power electronic converter is needed for SRM drives. The asymmetrical half-bridge (AHB) stands out as the most widely adopted choice. However, this particular topology demands a more intricate power converter design. This complexity arises from the fact that it is a less commonly used converter setup and because it necessitates a substantial DC-link capacitor. A total DC-link voltage can be applied to phase terminals, thereby utilizing high DC-link voltage. Constant permanent magnet excitation offers benefits within the constant torque speed range. Nonetheless, it presents drawbacks when operating at high rotational speeds. Consequently, the extended speed range of PM synchronous machines is constrained by the limited capacity of their DC-link voltage and current. Additionally, the efficiency of these machines decreases when they engage in field weakening operations. However, SRMs offer better performance in the field weakening region.

Figure 1.2 illustrates the common operating modes of the AHB [20]. In the excitation stage, both switches are actively ON. During this period, the phase voltage equals the DC-link voltage, causing quick increase in the phase current. In the freewheeling state, the lower switch remains ON, while the upper switch is turned OFF. Consequently, the phase voltage drops to zero, and the phase current decreases. In the demagnetization state, neither switch is activated. In this mode, a negative DC-link voltage is applied to the phase winding, and the current gradually reduces until it reaches zero. The phase voltage of the SRM can be deduced as

$$u_k = R_k i_k + L_k(\theta, i_k)\frac{di_k}{dt} + \frac{\partial L_k(\theta, i_k)}{\partial \theta}\omega i_k, \tag{1.1}$$

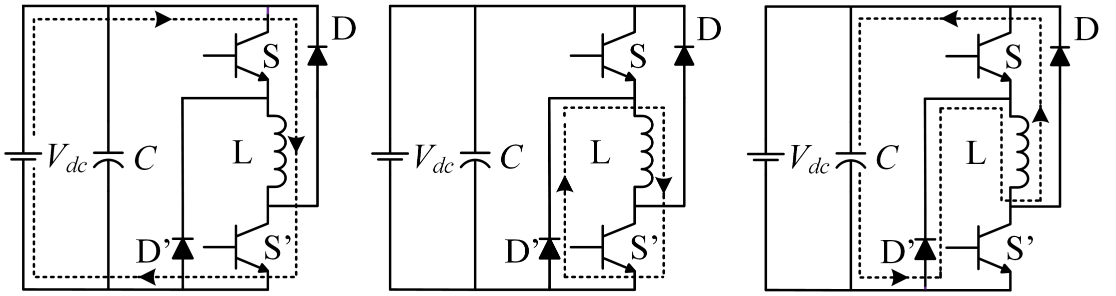

Figure 1.2: Working states of AHB (a) Excitation state (b) Freewheeling state (c) Demagnetization state.

where u_k is the phase voltage, i_k is the phase current, $L_k(\theta, i_k)$ is the phase inductance, ω is the angular speed, and θ is the rotor position [1]. The mechanical equation describing the dynamic behavior is deduced as

$$J\frac{d\omega}{dt} = T_e - T_L - F\omega, \tag{1.2}$$

where J is the rotor inertia, ω is the angular speed, T_e is the electromagnetic torque, T_L is the load torque and F is the damping coefficient. The electromagnetic torque produced due to the principle of minimum reluctance is given by

$$T_e = \sum_{k=1}^{m} \frac{i_k^2}{2} \frac{\partial L_k(\theta,\ i_k)}{\partial \theta} \tag{1.3}$$

The operation of SRM is quite different from that of synchronous motors as it relies on reluctance torque rather than a continuous torque. This unique characteristics results in some challenges, including significant torque ripple and and a magnetization behavior that is highly nonlinear. The generation of torque depends on the precise switching action based on the rotor position. One common method of controlling SRMs is by adjusting the angle at which switching occurs known as angle control where appropriate turn-on and turn-off angles are selected. Current control such as soft/hard chopping are also frequently used. Current chopping control is typically applied in low and medium-speed operations where there is enough time for the current to reach its maximum value, allowing for adjustments to achieve the desired performance. On the other hand, angle control is utilized during high speed operations where there is not sufficient time for the current to reach its peak. In such cases, the focus shifts to controlling the on/off angles to enable more efficient current flow. The effect of ITSCs in SRMs under both the control schemes are discussed in detail in the subsequent chapters.

1.2 Literature Review

1.2.1 Faults in SRMs

A list of possible SCFs and OCFs in a typical SRM drive excited by an asymmetrical bridge is depicted in Table 1.2 and Table 1.3, respectively. The circuit conditions for possible short circuit and open circuit faults are shown in Figure 1.3 and Figure 1.4, respectively [21]. Some of them strictly require the phase to be disabled, although in some cases, there are possibilities of utilizing the phase even in abnormal conditions at the cost of deteriorated performance. As mentioned, SRMs are also susceptible to mechanical faults such as eccentricity and bearing failures, affecting motor performance adversely. Eccentricity exists in a motor when there is an uneven air gap between the stator and the rotor poles. There is also the possibility of sensor failures within the drive. However, as the thesis deals with the electrical fault within the motor, the mechanical or sensor faults

Table 1.2: Short Circuit Faults

Serial	Fault Description	Continued Operation
1	Upper Switch	Possible
2	Lower Switch	Possible
3	Upper Diode	Disable Phase
4	Lower Diode	Disable Phase
5	Part of a winding	Possible
6	Full Winding	Possible
7	Full phase (motor)	Disable Phase
8	Full phase (converter)	Disable Phase
9	Power bus to phase winding	Unlikely
10	Power bus to part of winding	Unlikely
11	Phase to ground	Disable Phase
12	Power Short	Disable Drive

Table 1.3: Open Circuit Faults

Serial	Fault Description	Continued Operation
1	Upper Switch	Disable Phase
2	Lower Switch	Disable Phase
3	Windings (series conection)	Disable Phase
4	Windings (parallel connection)	Possible
5	Diode	Possible
6	Power	Disable Drive
7	Power Capacitor	Possible

and their consequences are not discussed in detail.

Knowing the possible consequences of different faults is imperative for deciding their severity and developing remediation strategies. Charles M. Stephens of General Electric Corporate R&D initially performed experiments to define the performance effects of

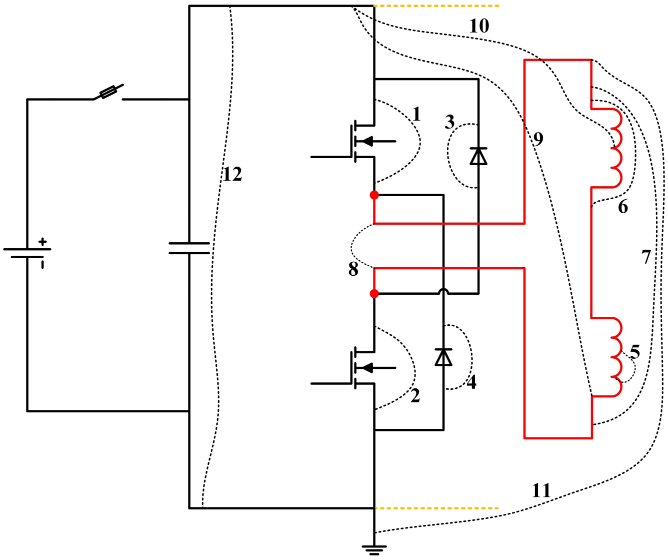

Figure 1.3: Possible short circuit faults.

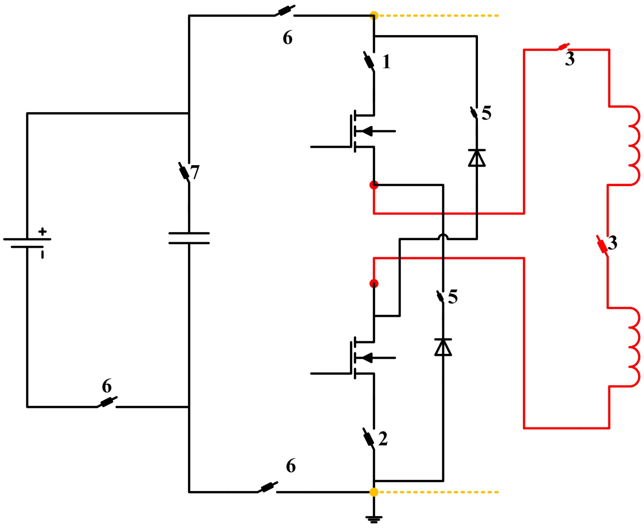

Figure 1.4: Possible open circuit faults.

electrical faults in SRM drives [22]. Experiments were conducted by creating different SCFs and OCFs on a four-phase SRM driven by an asymmetric half-bridge converter. In [23], an in-depth analysis of such fault conditions depicting variations in performance indices, such as noise, speed and torque ripple, is discussed. The findings of the analysis mentioned above arrived at a common conclusion. Disconnecting a faulted phase in some cases is not at all harmful. However, it reduces the torque output proportional to the number of inactive phases. In the case of phase absence, average electromagnetic torque, T_{fav}, is given by

$$T_{fav} = \frac{m-1}{m} T_{av}, \tag{1.4}$$

where T_{av} is the average electromagnetic torque under operation, and m is the number of phases. It was observed that torque and speed ripple increase in both the OCFs and SCFs. Because multi-phase SRM can be operated with one or more phases disabled, this motor has inherently a fault-tolerant structure. Required torque may be obtained by increasing the excitation of the remaining active phases. The most damaging effects, i.e., excessive phase current (limited by winding resistance and rotational voltage only) and vibrations are observed in a shorted phase with continuous excitation. The complete shorted pole and the case of a few shorted turns are evaluated with a continuous operation, which shows that the efficiency loss is lower when fewer turns are shorted than when the complete pole is shorted [5]. Higher torque can be expected under angle control as a part of the winding is still in action with an increase in the torque ripple. For the motor operating under current control with a fixed reference current, the average torque reduces with the increase in the torque ripple. However, under closed-loop current control, the healthy phases maintain the required average torque but with a higher torque ripple. Also, a high localized current is circulated in the shorted turns, which may lead to unbalanced force inside the machine. The local hotspot created results in the propagation of the fault with continued operation, leading to a complete phase short, which is more dangerous, as discussed. The majority of the phase short circuit results from ITSCs only. Moreover, in the case of ITSCs with fewer turns, the fault features are least evident on the motor parameters and, therefore, difficult to diagnose. The effect of ITSCs on the performance of SRM operating under different control strategies are elaborated thoroughly in subsequent chapters. Considering the behavior and repercussions of ITSCs, the thesis investigates the diagnosis techniques for ITSCs with higher sensitivity and reliability.

1.2.2 Existing Fault Diagnosis Techniques

The area of fault diagnosis for SRMs is still evolving and is immature compared to conventional motors. Table 1.4 summarizes the diagnosis techniques for electrical and mechanical faults in SRMs based on different methodologies [24–44]. It can be apprehended that most of the existing techniques regarding electrical faults target OCFs and SCFs at the converter end. Also, the SCFs within the motor with complete phase winding/entire pole short-circuited have been studied and analyzed in detail. It also includes some techniques related to ITSCs; however, most of the analysis is for a larger number of shorted turns. The major techniques related to the diagnosis of ITSCs in SRMs are discussed in detail, with their shortcomings that need to be encompassed in any sophisticated fault diagnosis systems. The objectives of the thesis have been decided by analyzing the research gap in the existing methodologies to make the SRM technology more adaptable for different applications.

SRMs, being somewhat new compared to conventional motors, have been given very little priority in fault diagnosis. Much of the research on SRMs has primarily focused on the design aspects and development of control strategies and techniques aimed at reducing torque ripples, as evidenced by various studies. In contrast, the diagnosis of different fault types for conventional motors like IMs and PMSMs has matured over several decades of research and is properly categorized. Multiple approaches exist to detect even ITSCs at the early stage, offering superior sensitivity and reliability. The first group is based on signal analysis, which employs methodologies based on current signature analysis, negative sequence analysis, wavelet decomposition and electromagnetic field monitoring. This group comprises mostly the analysis of electrical signals for which the classification is tabulated in Table 1.5. In [45], an online diagnosis method is developed using motor current signature analysis. The technique uses the spectra of the phase currents to identify and distinguish faults, including winding short circuits. Abnormal harmonics generated in the phase currents due to faults have been used as a fault indicator. An online diagnosis technique has been presented addressing the turn-to-turn insulation deterioration based on negative sequence impedance [46]. The turn-to-turn defects resulting from the dielectric stresses of over voltages and other adverse conditions have been identified as potential sources of other catastrophic winding failures. In [47], the harmonic analysis of the stray flux is carried out for the IM once operated with a sinusoidal supply and again using a voltage source inverter to analyze motor winding conditions. The technique is

Table 1.4: Summary of the fault diagnosis techniques

Method	**Adopted Technique**	**Target Fault Types**
Spectrum Analysis	Application of FFT to the DC bus current [24]	Open circuit fault
	Symmetrical components of phase currents [25]	Short circuit fault (Interturn short circuits)
	Application of FFT to the DC bus current [26]	Open and short circuit fault (Power Switches & Complete Pole & Phase Short)
	FFT of the torque signal [27]	Open circuit fault
	Symmetrical components of phase currents and ratio of the components [28]	Short circuit fault (Interturn short circuits)
Wavelet Decomposition	Decomposition of DC bus current [29]	Open and short circuit faults (Power Switches)
Extended Kalman Filter	Estimation of resistance based on DC bus current [30]	Short circuit faults (Interturn Short Circuits)
Coordinates Transformation	Park transformation on phase currents [31]	Open and short circuit faults (Power Switches)
	Transformation applied to gate signals [32]	Short circuit fault (Interturn short circuits)
Current Profiling	Current gradient and freewheeling time [33]	Open and short circuit faults (Power Switches)
	Compare currents with preset threshold or estimate value to detect the fault [34]	Open and short circuit faults (Power Switches)
	Variation in the pattern of induced currents through signal injection [35]	Eccentricity fault
	Overshoots in the phase currents over reference band [36]	Short circuit faults (Interturn short circuits)
	Transient pulse injection [37]	Open and short circuit faults (Power Switches)
Voltage Profiling	Comparison of induced phase voltage [38]	Eccentricity fault and short circuit faults (Complete Pole Short)
Gate Signal	Logic calculation on currents and gate signals [39]	Open and short circuit faults (Power Switches)
	Differential gate signals of upper and lower switches combining position signal [40]	Open and short circuit faults (Power Switches)
Differential Current Protection	Comparison of the differential current value [41]	Phase-to-phase fault
Trial & Error Method	Open or close specific switches and observe the amplitude of the phase currents [42]	Open and short circuit faults (Power Switches)
	Injection of HF pulses into two coils [43]	Eccentricity faults
Thermal Analysis	Thermal profile of the faulty winding [44]	Short circuit faults (Interturn short circuits)

Table 1.5: Classification based on analysis of electrical signals

Classifications	**Technique**
Direct use of electrical signals	Phase difference Residual voltage after turn-off Instantaneous power
Processing of electrical signals	Negative sequence currents Coordinate transformation Motor current signature analysis Positive and negative sequence of third harmonic line currents Park's vector
Redefining the features of electrical signal	Air-gap torque Sequence impedance Pendulum swing phenomenon Extended Park's vector approach

non-invasive and more reliable than the techniques based on current signature analysis. Also, the technique is easy to implement and utilizes low-cost instruments. A method based on current analysis overcoming the averaging issues of classical FFTs has been implemented for detecting shorted turns in IMs [48]. Two distinct approaches have been used: short-time FFTs and wavelet decomposition. The problems associated with the current signature analysis at varying loads/speeds are eliminated in this proposed method. Also, numerous methods have been established to diagnose the ITSCs based on temperature, magnetic flux, vibration or other physical quantities.

Model-based and parameter estimation is the second group of fault diagnosis. In [49], a model based technique for ITSCs for IMs is presented. The technique relies on the generation of a vector of a specific residuals using a state observer. It allows rapid diagnosis of an incipient fault. The method is reliable owing to parameter or load variations. The proposed technique is capable of detecting even 2% of shorted turns proving its higher sensitivity towards minor faults. A short-time least square Pronyds-based method has been introduced to diagnose ITSCs [50]. The ratio of the zero and positive voltage symmetrical components has been utilized as the fault indicator. The method possesses fast diagnosis, high precision and reliability even under load variations or unbalanced supply voltage. Online detection of stator faults in direct torque controlled driven IM has been proposed and implemented based on estimating the off-diagonal term in the IM sequence components impedance matrix [51]. The technique does not require any prior data on the motor parameters. Also, the method is highly sensitive as it can detect incipient failure of even 1% short circuit within the winding. Symmetrical component decomposition and the Savitzky-Golay filter are used to estimate different parameters. The percentage of shorted turns and fault loop resistance in induction motors are estimated using a nonlinear Kalman filter employing equality constraint [52]. Sequence component model analysis is used to deduce the constraints. The same method can be used to estimate fault severity of ITSCs in other electrical machines exploiting state space models. A fault indicator estimated using the stator voltage and current for a model of an asymmetric machine subjected to voltage imbalance is used for diagnosing ITSC in IMs [53]. It helps quantify the fault severity and also identifies the faulty phase. The model developed also distinguishes the effect of voltage imbalance, asymmetry and voltage imbalance.

The third group includes data-driven approaches where a large amount of data is collected for different motor conditions, and diagnosis methods are formulated with the help of machine learning and neural networks. A neural approach has been used to diagnose and locate ITSCs in stator windings of an IM. A multi-layer perceptron neural network trained by back-propagation is used to achieve the diagnosis [54]. The location of the fault is done by monitoring phase shifts between the phase voltage and line currents. The data for training the network are generated experimentally from a three-phase IM. A vibration analysis-based ITSC diagnosis approach is proposed using a neural network involving optimization of the network size of a probabilistic neural network [55]. A Growing Curvilinear Component Analysis neural network has been introduced to diagnose ITSCs in induction motors [56]. It can isolate the healthy cluster from the faulty ones and track the severity of the fault in a very short time. A deep learning-based framework has been introduced to diagnose minor stator winding interturn faults without having load information [57]. The three-phase current of an induction motor is converted to the Park's vector, which is then encoded into an RGB image using a recurrence plot and fed to a convolutional neural network (RPCNNet) to identify the fault. The recognition performance of this network is compared with other benchmark convolutional neural network models, namely "VGG16", "AlexNet", "ResNet50", and "DenseNet201".

Similarly, there has been intensive research devising diagnosing techniques for ITSCs in PMSMs. An online diagnosis technique with a simple fault indicator defined as the sum of absolute differences between stator currents has been introduced for PMSMs [58]. The amplitudes of the fundamental components are evaluated by using a frequency-tracking system. The technique also helps detect open switch faults and bearing failures. ITSC diagnosis for model predictive controlled (MPC) PMSM has been proposed that utilizes the energy-related feature vector evaluated using wavelet transform coefficients and cost function [59]. The method considers the MPC characteristics and presents improved reliability. Voltage and current residuals induced by ITSC are used to diagnose the fault [60]. The fault index based on the least square method has been deduced to indicate the severity of the fault. The second harmonic component in the q-axis current is evaluated using harmonic analysis. The method is restricted to steady-state operation [61]. A fault indicator based on the relationship between the rotor speed and fault current to diagnose incipient ITSC in PMSMs [62]. The indicator is immune to the rotational speed of the motor. An expression of the indicator has also been introduced by exploiting negative sequence components. The zero-sequence component of the voltage helps detect ITSC, and the escalated torque ripple in the PMSM is reduced by the current injection-based tolerant approach [63]. Considering any load/speed variation during the motor operation, the technique is reliable and highly sensitive to minor fault conditions. A model-based strategy has been introduced based on the residual current vector for diagnosing ITSCs in PMSMs [64]. The difference between the stator currents estimated by the state observer and the measured current has been exploited to devise the fault indicator. The technique is robust and reliable in transient conditions with different disturbances. An efficient method based on the stacked sparse auto-encoders and Siamese network has been introduced to diagnose ITSCs in PMSMs [65]. The proposed method exploits federated learning to solve the problem of sparse samples, thereby eliminating the requirement for many data. A Bayesian optimization-based residual convolutional neural network process is proposed for PMSMs [66]. The technique is effective and able to identify the faults at an early stage. Moreover, experimental results confirm the robustness of the scheme under different operating conditions.

A sophisticated fault diagnosis system must incorporate several factors, such as sensitivity to minor faults, reliability of the method/immunity of the fault indicator under different operating and transient conditions, least computation involved, fast diagnosis, and applicability to different control schemes and motor configurations. These characteristics have been considered with utmost importance in the methods for IMs and PMSMs discussed above. Moreover, sensitivity is of great importance for the diagnosis systems of ITSCs because the fault must be identified at the incipient stage to avoid further failures, as discussed previously. Table 1.6 lists the least severity (percentage of shorted turns) detected experimentally using some detection techniques for IMs and PMSMs [67–85]. It shows the maturity of the detection schemes, which are still lacking in the case of SRMs, elaborated later.

The operational principles and control strategies of SRMs significantly deviate from those of traditional motors. Consequently, the approaches previously discussed for IMs and PMSMs are not applicable for directly identifying ITSCs in SRMs. Furthermore, there has been limited research on diagnosing winding faults in SRMs of which the major contributions are discussed here. Even the existing methods available for detecting ITSC in SRMs exhibit deficiencies. In a prior study [86], a neural-based model has been extensively employed to investigate the impact of ITSCs in SRMs. This methodology proves highly proficient in accurately portraying the magnetic characteristics of the SRM when experiencing winding faults (one coil being shorted). Nevertheless, its suitability for rapid online diagnosis is limited because it necessitates real-time motor parameter inputs, which fluctuate during operation and entail a longer processing duration. An extended Kalman filter is used to estimate the phase winding resistance exploiting the DC link current [30]. With the motor subjected to ITSC, the winding resistance deviates, which is estimated in this technique. However, the estimation of resistance, which is temperature-dependent, might be easily affected by any load variation restricting its reliability. The lowest severity detected in this technique is 5% ITSC, corresponding

Table 1.6: Least severity detected

Motor type	**Diagnosis Technique**	**Severity**
IM [67]	MCSA-Sequence components of stator currents	0.43%
IM [68]	MCSA-FFT	20%
IM [69]	MCSA- Current envelope	0.42%
IM [70]	MCSA- Multiple reference frame theory	2.04%
IM [71]	Coupled negative and positive sequence impedance	0.23%
IM [72]	Rotor field voltage	0.32%
IM [73]	External flux	6%
IM [74]	Inverter switching states	0.76%
IM [75]	High-frequency signal injection	0.30%
IM [76]	Pendulous oscillation phenomenon	1.39%
IM [77]	State observer model	2.08%
IM [78]	Neural network	0.51%
IM [79]	Adaptive neural fuzzy system	1.16%
IM [80]	Fuzzy neural network	0.42%
PMSM [81]	MCSA- Fourier Series	4.17%
PMSM [82]	MCSA- Wavelet	2.78%
PMSM [83]	Air gap flux using search coils	7.7%
PMSM [84]	State space vector of voltage	2.89%
PMSM [85]	Electromagnetic torque and summation of phase voltages	9.09%

to 20 turns out of 400 in a phase winding. The fundamental component of the four-phase currents is extracted using a Fast Fourier transform to reconstruct symmetrical phase currents to detect ITSCs in SRM [25]. The positive and negative sequence components ratio is utilized as the fault indicator. The proposed method has been validated for 25% ITSC with 72 turns in a phase. However, it is reliable only for short circuits over 50% of phase winding. A complete cycle of all the phase currents of SRM is required for frequency domain analysis that necessitates a longer sampling window. Such a longer sampling window increases the diagnosis time, and therefore, the diagnosis methodologies based on spectral analysis are discouraged for SRMs. An analysis of surface thermal patterns has been conducted on an 8/6 SRM under various ITSC scenarios including turn-to-turn short circuit [44]. This analysis aimed to capture thermal signatures associated with these conditions. The simulation outcomes were cross-checked by comparing them to images obtained with a thermal imaging camera and readings obtained from a K-type thermocouple, affirming their accuracy. Thermal imaging is a viable approach for identifying abnormal conditions linked to short circuits, but it comes at a considerable cost. The diagnostic approach employed for identifying ITSCs in dual stator SRMs relies on the maximum current point tracking method, as detailed in reference [87]. It is important to note that this method is applicable only when the SRM operates under control strategies other than current control. Consequently, it cannot be utilized independently of control strategies. The proposed technique has been validated for 10% ITSC with 100 turns in a phase. The formulated fault index is not immune to load/speed variations indicating low reliability. In [36], a new method has been proposed for SRM achieving higher sensitivity and fast response. The phase current naturally exceeds the predefined reference value due to delays in both software and hardware components. This overshoot becomes more pronounced when the motor experiences interturn short circuits caused by fluctuations in inductance. However, for ITSCs of fewer turns, the faults features are not quite obvious in the measured parameters. The increased overshoot is leveraged to create fault indicators for each motor phase. It is important to note that this diagnostic approach is only effective when the machine operates with CCC. The technique is robust to transient conditions where the fault indicator remains immune to load/speed fluctuation. The method has been validated for 12.5% ITSC over a pole of 8/6 SRM. A diagnostic approach has been introduced to detect ITSCs in SRMs [28]. Initially, a model is developed to represent a phase winding featuring an ITSC, and this model is used to analyze the characteristics of the fault. In normal operating conditions, the phase currents primarily consist of sinusoidal components that exhibit a positive sequence with minimal distortion. A Fourier analysis extracts the frequency signature to assess the operational state of the motor under normal circumstances. Conversely, when a fault occurs, it disrupts the symmetry of the phase currents, leading to the emergence of both negative and zero sequence components. A fault index, the ratio between negative and positive sequence components of the phase currents, is formulated to assess this asymmetry. This index serves as a means to diagnose the fault and is not influenced by any parameters such as load torque, rotor speed and turn-on and turn-off angle. A summary of the major contributions related to diagnosis of ITSCs in SRMs discussed above is tabulated in Table 1.7.

The limitations associated with the methods discussed above are of utmost importance and should be taken into consideration when developing an advanced fault diagnosis system. These limitations are enumerated here:

1) Heavy computation burden for analysis and formulation of the diagnosis methodology.

2) A longer sampling window required for frequency analysis leads to slower diagnosis.

3) Most of the existing methods used to diagnose ITSCs have been validated by simulating a short circuit of substantial number of turns. Consequently, the reliability of these methods in identifying less severe ITSCs remains uncertain.

4) Fault features being least evident on the measured parameters under CCC mode of operation.

5) Some methods exhibit a dependency of the fault index on load variations, leading to a decrement in detection reliability.

6) As the behavior of SRM subjected to ITSC is not similar for every control method, it is not guaranteed that the diagnosis method devised for a control strategy would work appropriately for the machine operating with other control strategies.

Table 1.7: Comparison of the existing techniques

Diagnosis Principle	**Independent of control techniques**	**Sensitivity (Towards minor faults)**	**Reliability (Immunity of fault index to load variation)**	**Diagnosis during load & speed transition**
Overshoots in the phase currents	No	Medium (Validated for as low as one pole ITSC of 12.5%)	High	Not Addressed
Magnetic Flux Characteristic	Accurate estimation of flux characteristics under ITSCs. However, no specific monitoring methods is proposed. It requires highly accurate motor parameters, and the calculation process is complicated with high processing time. Not suitable for fast online diagnosis.			
Estimation of Winding Resistance	Yes	Low (Validated for as low 20 shorted turns over a phase having 400 turns)	Low	Not Addressed
Symmetrical Components	Yes	Low (Validated for as low as 18 shorted turns over a phase having 72 turns)	Low	Not Addressed
Thermal Signature Analysis	It is a non-invasive method based on thermal characteristics under ITSCs. Thermal imaging is a feasible method for condition monitoring; however, it is a costly and complicated procedure for motors that are not easily accessible.			
Maximum Current Point Tracking	No	Low (Validated for as low as 10 shorted turns over a phase having 100 turns)	Low	Not Addressed
Ratio of current components	Yes	Medium (Validated for as low as one pole ITSC of 12.5%)	High	Effective

1.3 Motivation & Objectives

Due to the unavailability and disrupted supply chain of rare-earth materials, SRM technology that is rare-earth free has attracted the scientific and industrial community after the advancement in power electronics. Many companies have started using SRM technology for commercial applications, claiming it to be a good alternative to traditional motors. As the technology of SRM is still evolving, intensive research is required considering different aspects to make the technology more adaptable, including the area of fault, which has been given very little priority. Stator faults, including 21% ITSCs, account for 40% of electrical machine faults. Also, most stator winding faults are due to rapid spreading ITSCs, often resulting in complete winding failures. Therefore, considering the reliable operation of SRMs in critical safety applications, the thesis has been dedicated to the diagnosis techniques for ITSCs in SRMs. The main motivation of the thesis is to address the shortcomings of the existing diagnosis techniques for ITSCs in SRMs.

As discussed in the literature review section, the fault features in the case of ITSC of fewer turns are least apparent in the measured variables of the motor under the CCC mode of operation that is widely preferred for low-medium speed applications. Thus, the motivation for objective 1 of the thesis is to propose a fault diagnosis method for low and medium-speed applications. Moreover, a novel and simple technique with minimal computation burden and low complexity has been formulated and validated for an 8/6 SRM.

The effect of ITSCs on the performance of SRMs differs for different control strategies. Therefore, it is not certain that a fault diagnosis system devised under a control method would work appropriately under another control scheme. Considering this issue in some of the existing techniques and objective 1, the motivation for objective 2 of the thesis is to propose a diagnosis technique applicable to SRMs independent of any control strategies and relevant for the entire speed range. Moreover, a novel diagnosis technique has been formulated and validated, eliminating the shortcomings of objective 1.

The outcomes of objective 2 of the thesis are remarkably outstanding compared to other existing techniques in terms of the least severity detected apart from its decoupled operation with the control strategies. However, these outcomes are obviously at the price of increased complexity and cost of the system due to the application of additional circuitries. Consequently, the motivation for the objective 3 of the thesis is to eliminate the complexity of the diagnosis system. Furthermore, a novel diagnosis technique has been formulated and validated by eliminating the complexity issue in objective 2.

Also, the key setbacks in the existing methodologies, such as sensitivity to ITSCs of fewer turns and reliability under different operating and transient conditions have been considered in all three objectives. All the techniques corresponding to the three objectives have been tested by operating the SRM under abrupt load/speed variations and when the motor is subjected to the fault during the transition period when the load/speed is varied.

To summarize, the objectives of the thesis are as follows:

Objective 1- To develop a fault diagnosis technique for ITSCs in SRMs for low and medium-speed applications.

Objective 2- To develop a fault diagnosis technique for ITSCs in SRMs for entire speed range independent of control strategies.

Objective 3- To develop a fault diagnosis technique for ITSCs in SRMs for entire speed range independent of control strategies with low complexity.

To address these objectives, the chapters of the thesis are as follows:

Chapter 2 proposes a new method to detect ITSCs in SRMs by monitoring post turn-off phase currents at around aligned rotor positions. It accurately identifies ITSCs as low as 4% turns without errors and is highly sensitive to minor short-circuits. It simplifies identifying faulty phases during operation, enabling timely maintenance to prevent motor damage. The method remains reliable under various loads and avoids saturation effects at higher loads, ensuring accurate fault detection regardless of load torque.

Chapter 3 introduces a new method for diagnosing ITSCs in SRMs, triggering an alarm if any unusual behavior is detected. To detect ITSC-related changes, it injects a high-frequency signal into the non-torque-producing phase, translating inductance variations. This approach is independent of the control strategies since it uses inactive phases for injection. It also identifies the problematic phase and roughly estimates the number of shorted turns by monitoring high-frequency signal peaks. The chapter also addresses the reliability of this detection method, accounting for both load variations and speed fluctuations.

Chapter 3 introduces a method that detects ITSCs by introducing high-frequency pulses to decipher the inductance variation. It focuses on the low-torque region near each phase unaligned rotor position for this purpose, minimizing unwanted torque generation. The injection frequency is carefully chosen to avoid significant loss. Importantly, these diagnostic pulses are introduced when the phases do not produce torque, making the method independent of control strategies and suitable for SRMs using any control approach. This method exhibits increased sensitivity to minor ITSCs and maintains reliability even when dealing with variations in load and speed.

Chapter 2

Diagnosis Technique for ITSCs in SRMs for Low & Medium Speed Applications

---

2.1 Introduction

The present chapter introduces a novel diagnosis method for ITSCs in SRMs suitable for low and medium speed applications. To operate the motor in constant torque region at low and medium speeds, CCC is widely preferred. The limitations in the existing techniques discussed previously are observed keenly and are accompanied in the proposed method. The basis of the diagnosis technique highlighting some of its main features are:

1) The fault diagnosis method involves monitoring the freewheeling phase currents right after the phase is turned off, particularly in the low torque area around the unaligned rotor positions. The change in inductance in the specific area of interest is minimal and can be assumed constant. Phase currents demagnetizes following a fixed rate determined by the ratio of inductance and resistance within the specified area. The monitoring process commences when the phase current reaches a value way below the saturation limit. This precaution is taken to prevent sudden shifts in inductance from affecting the process. Consequently, the method remains reliable even when the load fluctuates. Furthermore, any alterations in speed do not impact the effectiveness of the proposed method.

2) Inductance is proportional to the square of the number of turns which is pre-dominantly more affected than the phase resistance subjected to ITSCs. ITSCs causing a reduction in inductance results in a decrease in the associated time constant. Consequently, the current in the faulty phase diminishes at a faster rate compared to the normal phases. The method proposed in this study utilizes the changing time constant due to ITSCs to devise the fault indicator. This technique is characterized by its remarkable sensitivity, capable of detecting even minor short-circuits involving a mere four turns (approximately 4% ITSC) in a phase with a total of 108 turns. Importantly, the proposed method does not require complex computations and does not rely on any additional hardware components.

2.2 SRM: Operation & Effect of ITSCs

2.2.1 Description of SRM operating under CCC

Figure 2.1(a) illustrates a 4-phase 8/6 SRM that is powered using a widely preferred AHB converter. The inductance profile for one of the motor phases, as obtained through finite element analysis, is shown in Figure 2.1(b). During motoring operation, the phase switches (S and S') are activated in the region where the inductance has a rising slope to generate positive torque. Notably, for currents ranging from 1 A to 5 A, the unsaturated inductance plots closely follow a similar curve, reaching a maximum value of about 29 mH when the rotor is aligned. While smaller current values lead to minimal changes in inductance, the impact of saturation becomes apparent when the currents reach or exceed 8 A. Additionally, it can be ascertained that the alteration in inductance around the rotor position θ_a is negligible and can be considered consistent.

Controlling the phase currents is simpler when the motor is running at low speeds, allowing adjustments around a reference. As the speed increases to a medium range, keeping up with the reference becomes a bit more challenging but still achievable. However, as the speed continues to rise, the back electromotive force becomes stronger, limiting the capacity of the controller to manage the current effectively. This situation leads the SRMs to transition into single-pulse operation mode at higher speeds, as it becomes impractical

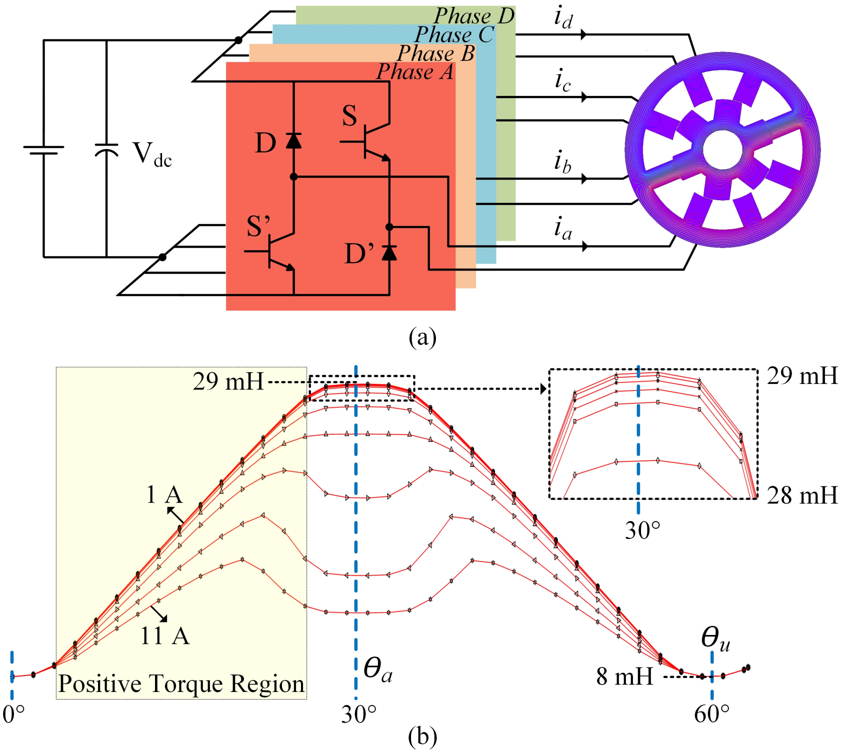

(a)

(b)

Figure 2.1: (a) Basic configuration of 8/6 SRM driven by an AHB (b) Incremental inductance for one of the phases obtained in FEA for currents 1 A to 11 A at the step of 1 A.

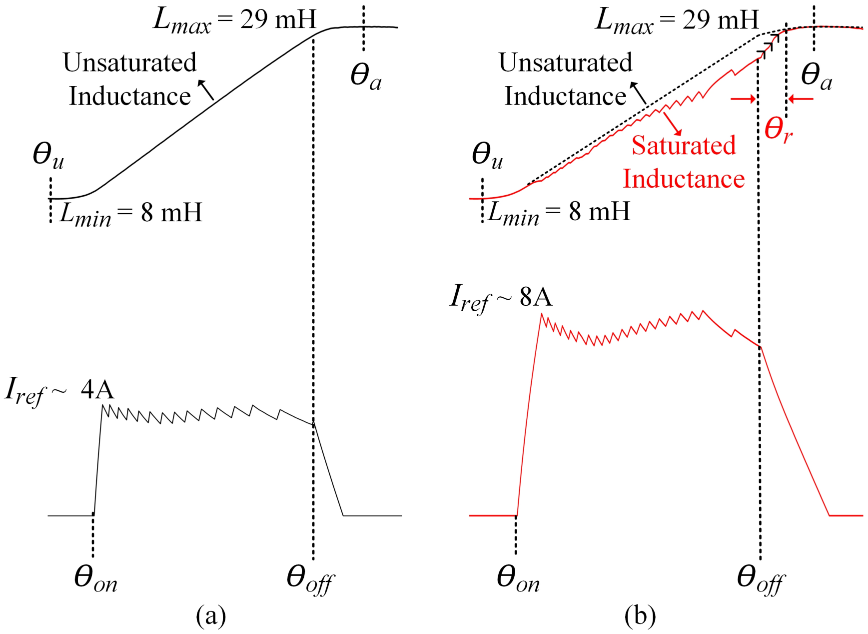

Figure 2.2: Effect of load variation on the inductance profile obtained in FEA (a) No saturation at light load (b) Saturation at a higher load.

to track the reference. As a result, accurate current regulation is feasible only at low and medium speeds, making it well-suited for applications requiring substantial torque. Figure 2.2(a) depicts the current of one of the phases for the motor operating at a light load condition. As discussed, the current with such amplitude cannot saturate the motor. The inductance, as shown in the same figure, remains unsaturated. However, under higher load conditions, the motor does reach a point of saturation, which leads to a sudden change in the inductance profile, as demonstrated in Figure 2.2(b). An interesting observation here is that once the phase is turned off at the position θ_{off}, the inductance starts recovering as soon as the current drops below the saturation limit. It gradually transitions back to following the unsaturated curve after passing through a certain angle θ_r. This recovery of the inductance profile from saturated to unsaturated conditions is primarily influenced by the characteristics of the core material.

2.2.2 Consequences of Interturn Short-Circuits under CCC

When the motor experiences ITSCs, the uniformity and balance of the magnetic flux distribution undergo changes. Additionally, the resistance and self-inductance of the faulty phase, which are linked to the number of turns in the motor, are influenced and diminished. In the context of CCC, where a consistent reference current is maintained, the strength of the magnetic flux diminishes due to the reduction in the number of active turns and the impact of the current in the shorted turns (i_s). These restrict the strengthening of the flux, thereby degrading the magnetic co-energy W given as

$$W = \sum_{h=1}^{N_h} \int_0^{i_z} \phi_h(i, \theta)\, di, \tag{2.1}$$

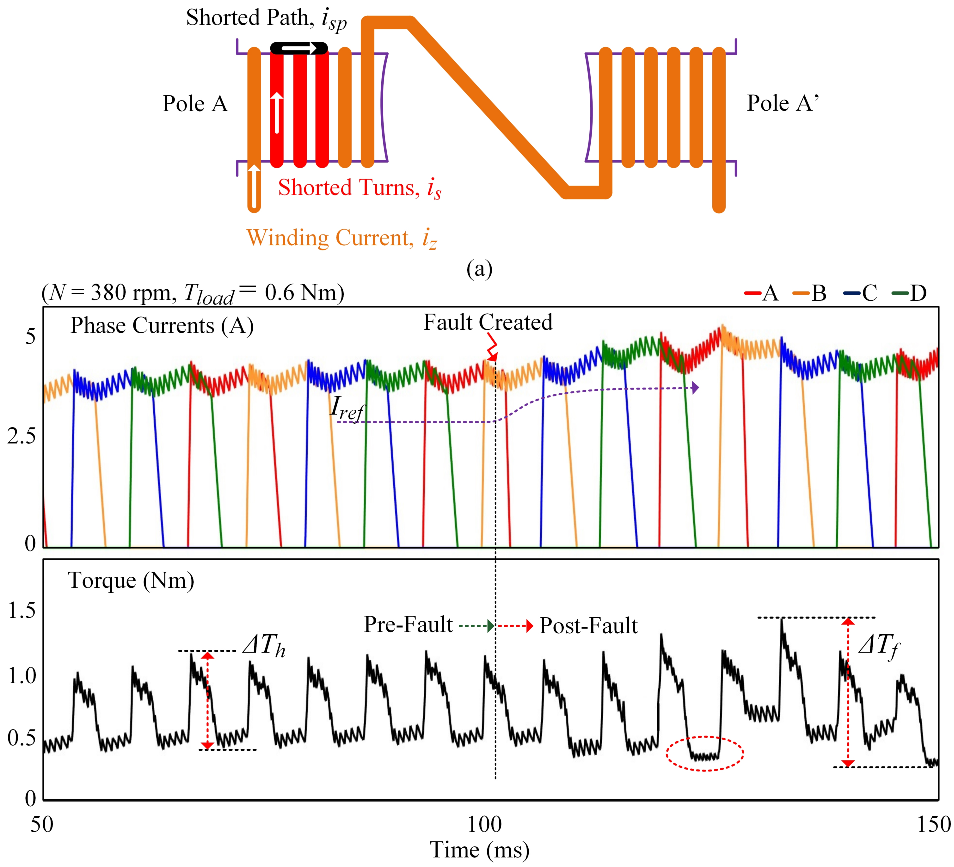

(a)

(b)

Figure 2.3: (a) One pole ITSC in a phase (b) Performance of 8/6 SRM in CCC under the influence of ITSC of 16% turn in phase A.

diminishes. T_{elec}, a function of magnetic co-energy produced by the faulty phase represented as

$$T_{elec} = \frac{\partial W}{\partial \theta}, \tag{2.2}$$

also reduces. In the case of the motor being under closed-loop speed control, the current reference is raised to ensure that the unaffected normal phases generate sufficient electromagnetic torque to fulfill the load requirements. This scenario is depicted in Figure 2.3(b), which showcases the impact of a 16% turn ITSC in phase A. The torque generated by the faulty phase A diminishes, as indicated within the circled area. As a result, the motor necessitates an augmentation in the reference current to compensate for the decreased torque. The healthy phases, upon increasing reference current, produce higher torque according to the demand inferred from the post-fault torque waveform. The difference between $\triangle T_h$ and $\triangle T_f$ is fairly evident, showing an escalated torque ripple in the motor due to ITSC.

The behavior of the phase A current remains consistent both before and after the fault occurrence due to the regulation provided by a hysteresis controller. Any shifts in the magnitude of the phase currents are primarily influenced by change in reference current to meet the load demand rather than the fault itself. Nevertheless, the effects of the fault become noticeable during the chopping period due to the varying inductance caused by ITSC, leading to overshoots in the current profile. Also, the rise and fall times of the faulty phase current are altered. The variation in fall time post turn-off is utilized for formulating the diagnosis technique elaborated in the subsequent sections.

2.3 Background of the Diagnosis Technique

The phase current is initiated in a way that the rotor has moved past the unaligned rotor position. This ensures that the current reaches the desired magnitude just as the inductance slope starts to rise. Additionally, the current is turned off strategically, allowing it to decrease and eventually reach zero around the aligned rotor positions where the rate of change of inductance ($dL/d\theta$) is approximately close to zero. The same has been illustrated in Figure 2.4. Due to ITSC, the reduction in inductance of the phase winding is more pronounced compared to the reduction in resistance. It is because the inductance is directly proportional to the square of the number of turns. Also, the mutual inductance between the remaining healthy turns and shorted turns tends to reduce the effective inductance of the phase winding. Consequently, rise and fall times (t_r and t_f) decreases. Figures 2.4(a) and 2.4(b) show the characteristics of phase currents under light and heavy loads for both normal and faulty conditions. At higher current demands exceeding the saturation limit (I_{sat}) under heavy loads, the current right after being

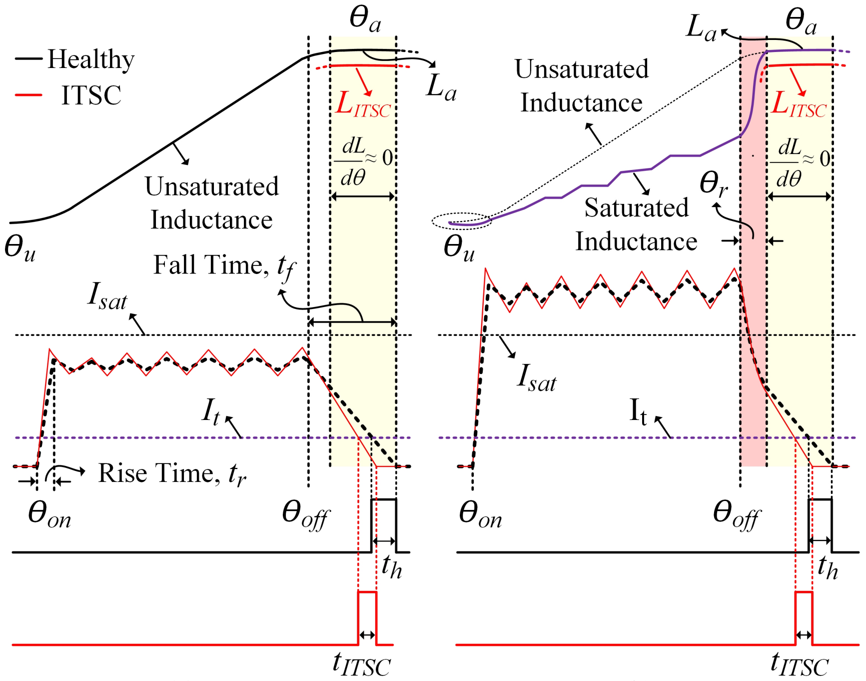

(a) (b)

Figure 2.4: Principle of diagnosis (a) Post turn-off current slope at light load (b) Post turn-off current slope at high load.

turned on can saturate the motor. It is in contrast to the situation under light loads. The immediate saturation of the inductance profile after θ_{on} is evident in the circled area in Figure 2.4(b). While t_r does experience variations due to ITSC, the sudden change in inductance makes t_r a function of the load for higher loads. As a result, it has not been utilized in the development of the fault indicator.

As previously mentioned, the current is deliberately turned off in a manner that allows it to decrease to zero within the flat inductance region before entering the negative torque area. However, the entire extent of t_f cannot be employed for creating the fault indicator because its initial portion does have a loading effect due to saturation. Once the phase of the motor driving a higher load is turned off, there is a delay before the inductance starts following the unsaturated curve, as described earlier. During this recovery period, represented as θ_r, the current decays proportionally to the variation in the inductance which is very abrupt and becomes rather unpredictable. Once the current falls below the saturation limit I_{sat} and enters the flat inductance zone, it begins to decrease with a constant slope. Furthermore, under light load conditions or when the phase current is below the saturation limit, the current follows the same slope while decaying within the flat zone. This consistent behavior is visible in both Figure 2.4(a) and Figure 2.4(b), where a section of the post-turn-off current decline shows the same slope within the flat inductance zone.

Moreover, the post turn-off current is tracked once it reaches a value I_t way below I_{sat} till it becomes zero for diagnosing the fault. It also ensures that the current is in the desired flat zone. During the turn-off, a negative voltage is applied to the phase. The voltage equals the negative of the dc source voltage V_{dc}. As the change in the inductance in the target area is insignificant, the induced emf term goes zero. Therefore, the phase equation can be represented as

$$-V_{dc} = R_{ph} i + L_a \frac{di}{dt}. \tag{2.3}$$

The initial and final conditions are

$$i(0) = I_t, \tag{2.4}$$

$$i(t_h) = 0 = I_{min}, \tag{2.5}$$

from which the fall time starting from I_t is evaluated as

$$t_h = \tau_h \ln \left[1 + \frac{R_{ph} I_t}{V_{dc}} \right], \tag{2.6}$$

A pulse is generated corresponding to the fall time of the current starting from I_t till it decays to zero ideally having the width t_h irrespective of the load governed by (2.6).

For the motor winding affected by ITSCs, the inductance diminishes to L_{ITSC} when the rotor is aligned, as seen in Figure 2.4. The phase current under faulty conditions is highlighted in red. Similarly, the value of t_{ITSC}, determined for the faulty state, experiences a decrement due to the reduction in τ_{ITSC} (calculated as L_{ITSC}/R_{ITSC}). This reduction happens because L_{ITSC} is significantly smaller than L_a, irrespective of the load conditions. Also, R_{ITSC} becomes less than R_{ph}, which tends to increase τ_{ITSC}. However, the decrement in inductance is dominant over the decrease in resistance, ultimately lowering the decay time ($t_{ITSC}<t_h$) depicted in Fig. 2.4. Since the current consistently decays within the flat inductance zone, the intended decay time remains unaffected by any variations in operational speed, as shown in Figure 2.5.

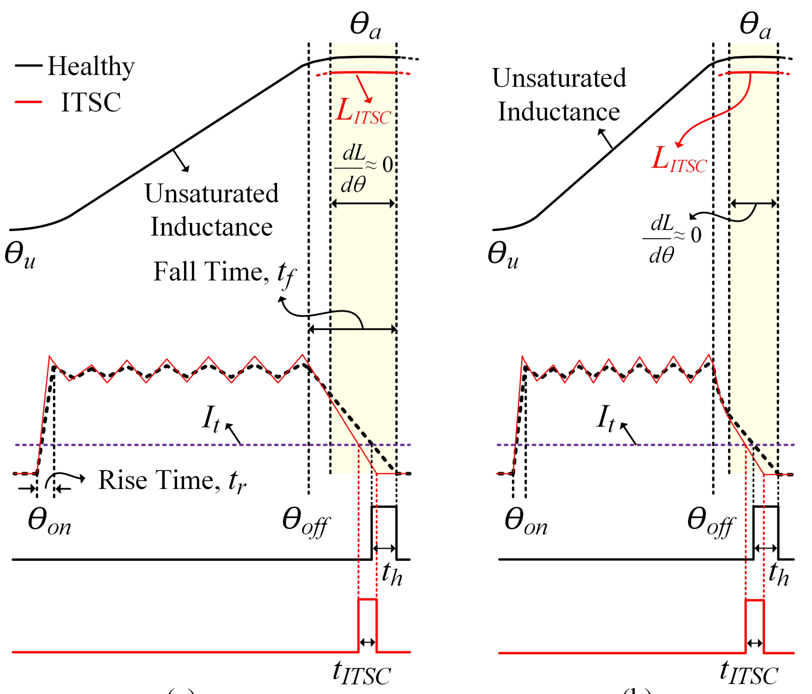

(a) (b)

Figure 2.5: Effect of speed variation on the target decay time (a) At speed ω_1 (b) At speed $\omega_2>\omega_1$.

The pulse duration, also known as the target decay time, is translated by triggering a counter for that specific duration. The peak of the counter is then compared with a predefined threshold value (x) to identify the onset of ITSC. The logical steps and procedures underlying the proposed diagnostic approach are clearly illustrated in Figure 2.6(a). The already acquired parameters like rotor position (θ) and the phase currents i_A to i_D are utilized to evaluate the desired decay time for diagnosis. I_t, θ_{offset} and x are specified in the controller. The tracking process is executed right from the moment of turning off each phase, extending to a position θ_{offset} ahead. This ensures that the phase currents fully decay within the provided offset interval. For example, $\theta_{off\_A}+\theta_{offset}$ for phase A, depicted in Figure 2.6(b). The target decay time corresponding to each phase is activated by initiating four separate counters set to operate within the time range of

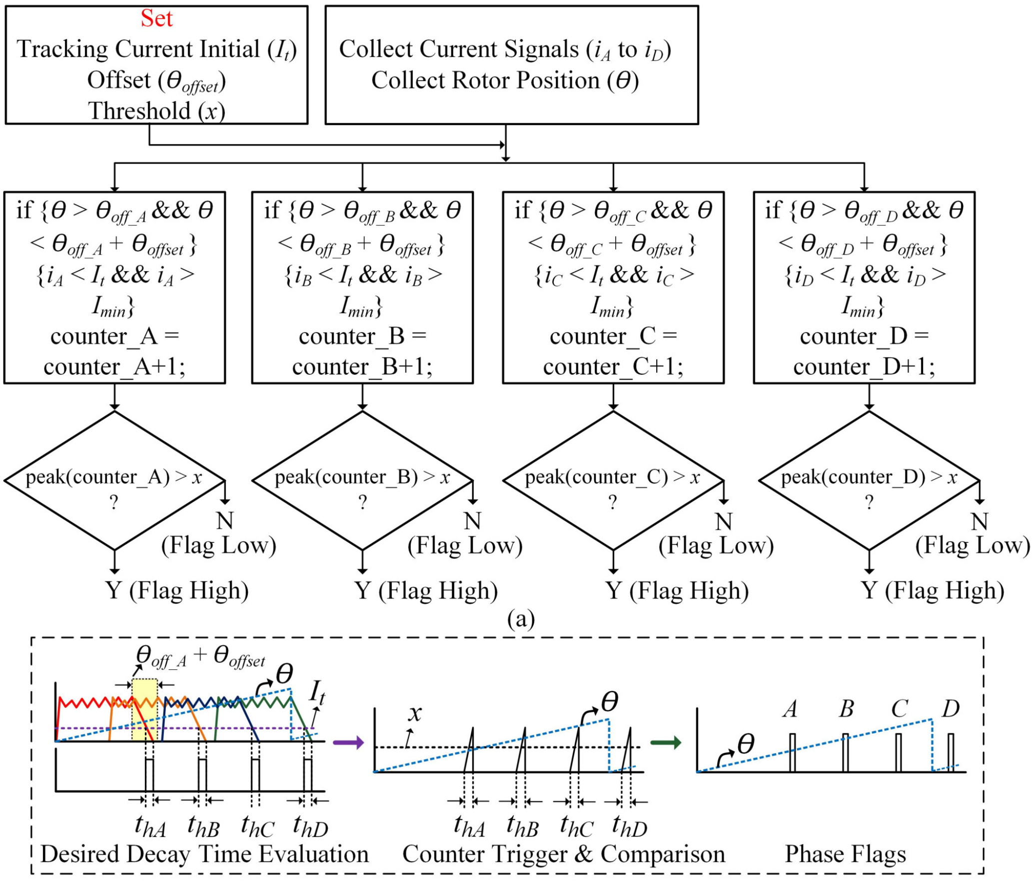

(a)

(b)

Figure 2.6: Flowchart and process of the proposed diagnosis scheme.

t_{hA} to t_{hD}. Whenever a counter surpasses a predetermined threshold, it indicates that the winding condition is normal. The value of x is determined through a series of experiments, depending on the minimum number of short-circuited turns that can be accurately detected using this proposed method. In normal conditions, the peaks of the counters corresponding to the four phases attain identical values. If the peak of counters surpasses x, it signifies an absence of the fault and confirms smooth operation. However, when any of the phases experiences ITSC, the decay time becomes shorter, leading to a decrease in the peak value of the counter. If the peak of a counter falls below x, the corresponding phase flag disappears, indicating the initiation of an ITSC event.

Also, the peak of the counter corresponding to the faulty phase varies with the increasing number of shorted turns. The decreasing nature of the peak value is used to derive the severity function that helps determine the number of shorted turns. The deduced SI is given by

$$SI = \frac{peak_h - peak_{ITSC}}{peak_n}. \tag{2.7}$$

2.4 Experimental Validation & Results

2.4.1 Experimental Setup

Table 2.1: Specifications of 8/6 SRM

Parameter	**Value**	**Parameter**	**Value**
Rated output power	1 hp	Stack length	102 mm
Rated input voltage	72 V	No. of poles (Stator/Rotor)	8/6
Rated speed	1200 rpm	Phase resistance	0.6 Ω
Stator outer diameter	165 mm	Stator pole arc	22.5°
Stator inner diameter	85 mm	Rotor pole arc	30°
Rotor outer diameter	84.5 mm	Number of turns/pole	54
Rotor inner diameter	33.5 mm	Air gap	0.5 mm

Experiments were performed on a four-phase 8/6 SRM prototype to prove the efficacy and feasibility of the proposed method. The parameters of the motor are outlined in Table 2.1. The control process is highlighted in the block diagram shown in Figure 2.7. The information about the rotor position is obtained by integrating the speed from the encoder fed back to the controller as an outer loop. The motor phases are operated successively according to the onset of the positive slope of their respective inductance profile, defining the fixed turn-on and turn-off angles. Each phase is excited for 21° in phase overlap mode to extract the optimal torque from the motor. The proportional-integral block generates the current reference in accordance with the intended load and operational speed of the motor. The disparity between the reference and the actual phase currents is controlled within a hysteresis band, which is further processed to produce switching signals. These signals are then applied to the gate terminals of the respective switches operating the SRM under CCC.

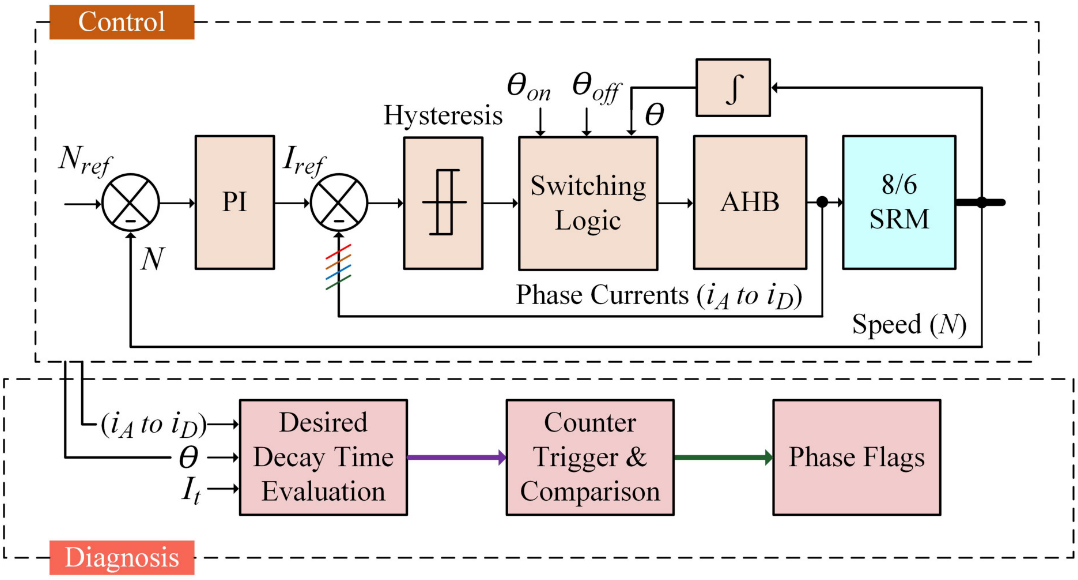

Figure 2.7: Block representation of control and diagnosis.

An experimental setup for validating the proposed approach involves a customized test rig featuring an 8/6 SRM. This test rig is capable of emulating ITSCs in two phases, as shown in Figure 2.8. To power the motor, an AHB converter is utilized, employing the Semikron IGBT modules SKM100GB12T4. The phase currents used as feedback for control are acquired using LEM hall effect based sensors LA 55 with a bandwidth of 100 kHz. For determining rotor position and speed, an incremental encoder with 1000 pulses per revolution is synchronized with an absolute encoder. The control and diagnostic logic, as depicted in Figure 2.6(a), is implemented within a digital signal processor (DSP) model TMS320F28379D. The validation of the proposed diagnostic method is carried out using the fundamental drive assembly of the SRM, eliminating the need for any additional hardware components.

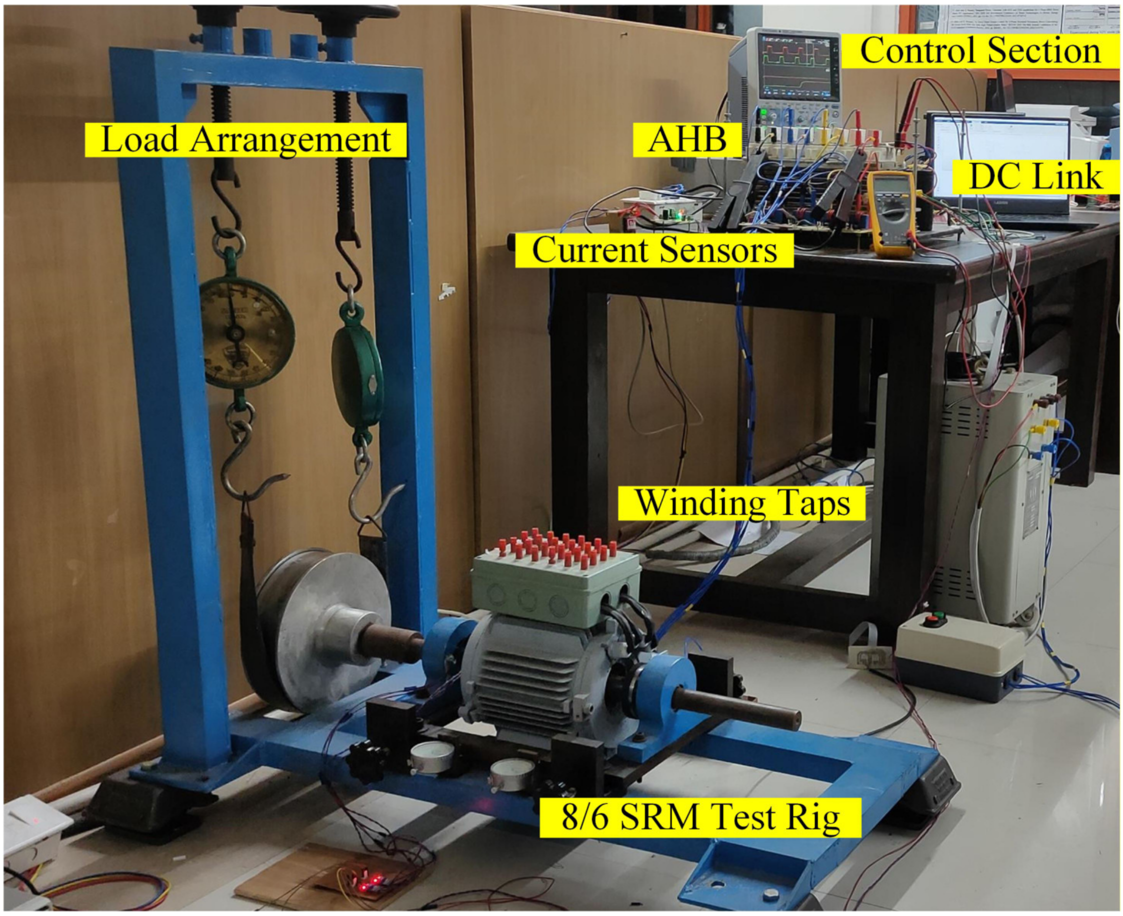

Figure 2.8: Experimental rig of customized 8/6 SRM.

2.4.2 Performance of SRM under ITSCs in CCC Mode

The parameters employed for carrying out the experimental validation are detailed in Table 2.2. Within this section, comprehensive results are presented, encompassing various aspects of the proposed method. These results include discussions on detection reliability, sensitivity, and other relevant considerations.

Table 2.2: Experimental parameters

Parameter	**Value**	**Parameter**	**Value**
DC link voltage (V_{dc})	72 V	Sampling rate	10 μs
Conduction angle (θ_{on}-θ_{off})	21°	Offset (θ_{offset})	10°
Tracking current initial (I_t)	1.5 A	Threshold (x)	0.95 V
Current hysteresis band	±0.4 A	Speed reference (N_{ref})	380 rpm

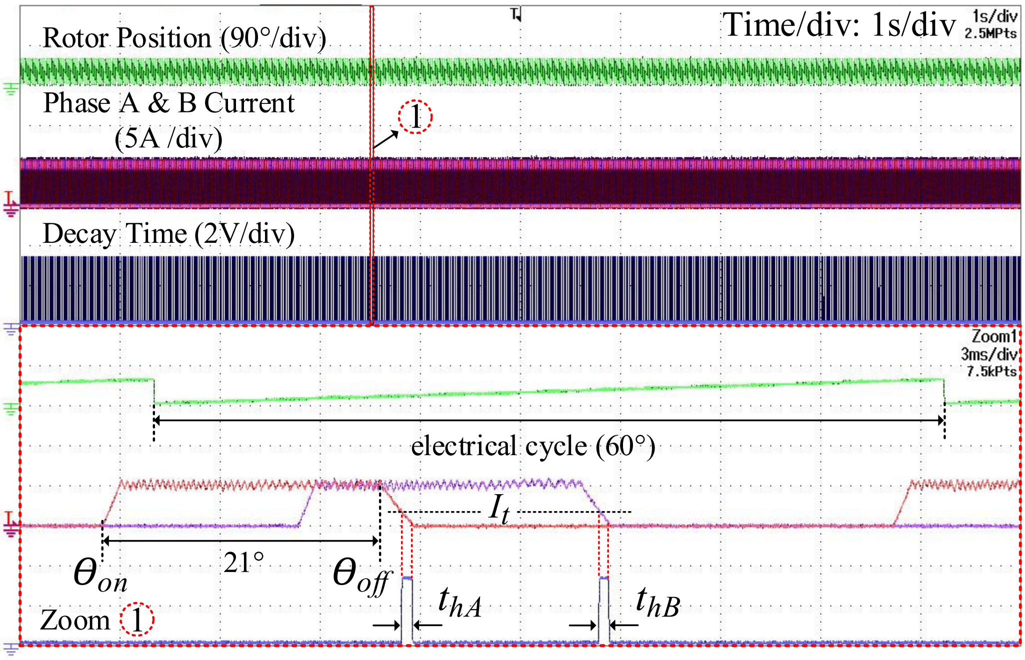

Figure 2.9: Rotor position, phase currents (A & B), and desired decay time (t_{hA} & t_{hB}) for normal operation at 380 rpm and 0.6 Nm of load torque.

Figure 2.9 illustrates the healthy operation of the motor that is operating at a speed reference of 380 rpm under a load torque of 0.6 Nm. The graph shows the two-phase currents (labeled as A and B) and their corresponding decay times, represented as pulse durations (t_{hA} and t_{hB}). It also includes information about the position of the rotor. Because the measurement scope has limited channels, only the currents of two consecutive phases are being monitored. Notably, both phase currents decays with an identical slope after they are turned off. In this specific operational state, the target decay time is 0.36 ms, originating from I_t for both phases.

ITSCs in the motor tends to increase the magnitude of the phase currents due to the increase in reference value, discussed previously. The same has been illustrated in the dashed yellow region representing the fault duration created by short-circuiting 18 turns ($\approx$ 16% ITSC over a phase) in phase A. t_{ITSC-A} for the faulty phase A reduces to a value of 0.16 ms compared to the decay time for other healthy phases. For clarity, the current of the adjacent phase B with t_{hB} of 0.36 ms is shown in the zoom window-1 of Figure 2.10. Also, there are overshoots in the faulty phase current over the specified hysteresis band during the chopping interval. The same can be inferred from the encircled areas in the zoom window-1 & 2 of Figure 2.12, representing phase A current post and during fault.

2.4.3 Characteristics of Diagnosis Signals in Healthy & Faulty Conditions

Based on the explanation of diagnosis logic in Figure 2.6, a digital counter is set up in the DSP for each phase to translate their corresponding target decay time. The value of the counters is retrieved by sending it to the digital-to-analog converter channels of the DSP.

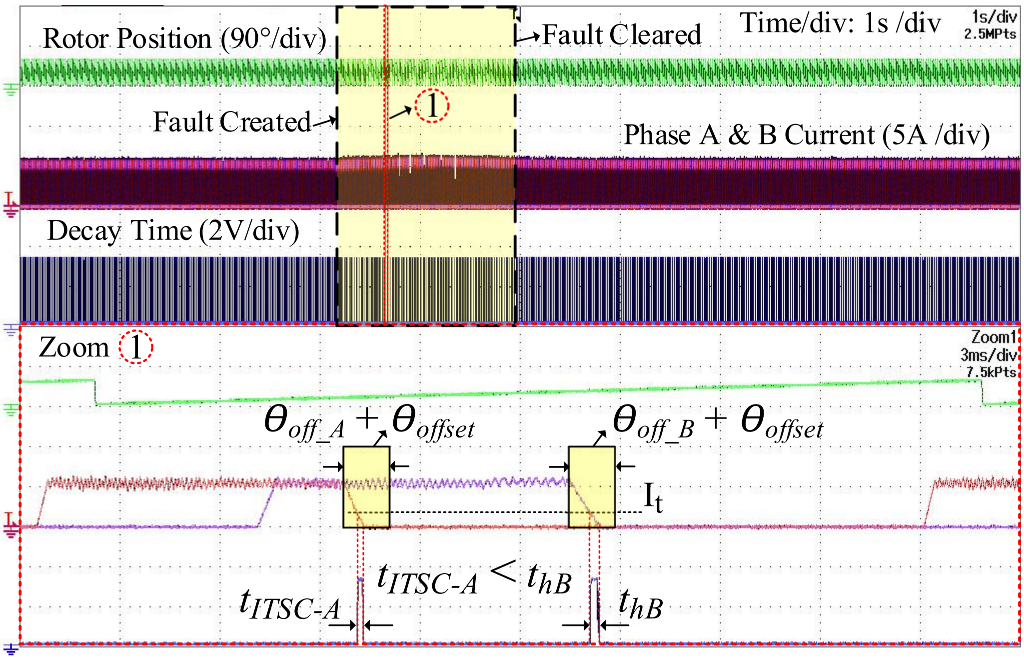

Figure 2.10: Rotor position, phase currents (A & B), and decay time (t_{hA} & t_{hD}) for 16% ITSC in phase A at 380 rpm and 0.6 Nm of load torque.

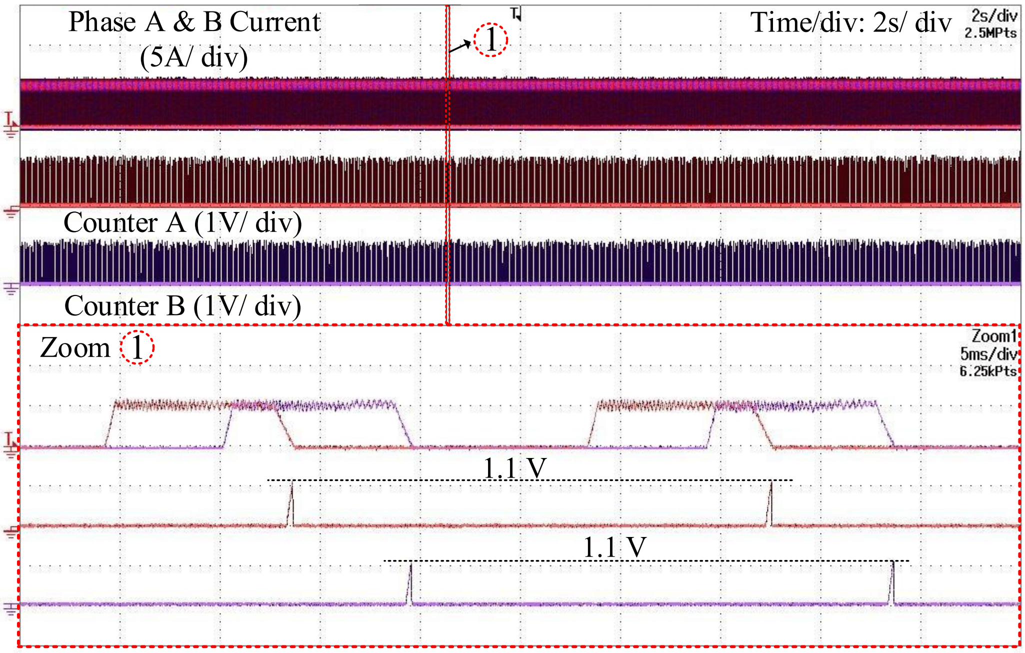

Figure 2.11: Phase currents (A & B) and their counter output for normal operation at 380 rpm and 0.6 Nm of load torque.

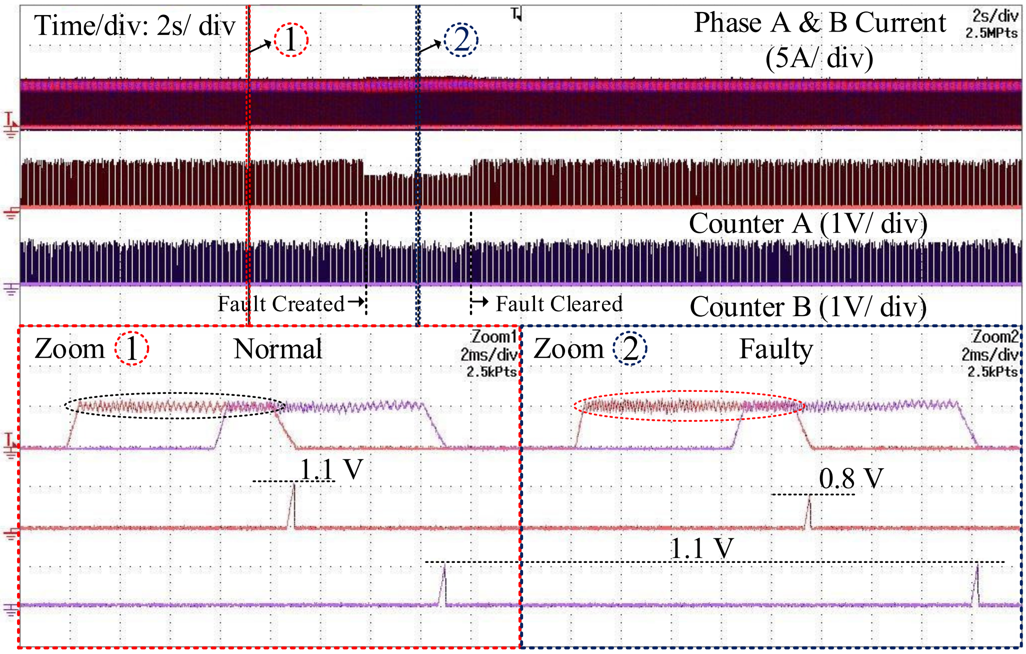

Figure 2.12: Phase currents (A & B) and their counter output for 4% ITSC in phase A at 380 rpm and 0.6 Nm of load torque.

Figure 2.11 presents phase A and B currents, along with the counter outputs linked to them. The counter outputs reach a peak value of around 1.1 volts, indicating a normal winding condition. However, when there is a 4% turn short circuit in phase A (as depicted in Figure 2.12), the peak of the counter for that phase drops to approximately 0.8 volts. It is worth noting that for other normal phases, the counter peak remains consistent at 1.1 volts, regardless of the condition. This observation can be made by analyzing the waveforms for phase B, which are shown in the magnified section of Figure 2.12.

Flags associated with each phase have been devised to mark the onset of ITSCs and to pinpoint the problematic phase. In healthy conditions, the counter reaches a value of 1.1 V. However, for a situation where there is a 4% ITSC, as shown in Figure 2.13, this value drops to 0.8 V. There is a considerable difference of around 30% in the counter values between healthy and faulty conditions. This difference offers a significant margin to establish a threshold value, which has been set at 0.95 V (approximately 15% lower than the healthy condition). The logic behind each flag is such that they stay high when the counter value exceeds the predetermined threshold, indicating trouble-free operation. Figure 2.13 demonstrates that the flag for phase A returns a value of 1 (equivalent to 3.3 volts) both before and after the fault within the tracking zone ($\theta_{off} + \theta_{offset}$), which is already presented in Figures 2.6 and 2.10. However, this flag disappears completely (goes to 0 volts) within the concerned tracking zone when a 4% turn short circuit occurs as the counter value drops below the threshold due to ITSC. This situation is highlighted in zoom window-1 & 2 of Figure 2.13 for better clarity. The onset of ITSC is only recognized after the faulty phase has turned off. For example, if a short circuit happens in phase A while phase C is active, the fault would be identified after phase A has been powered up again following the occurrence of the fault. To make it easier to understand, the flags for each phase are shown as separate signals. However, they can be combined using straightforward logic to create a single signal, which simplifies the diagnosis method.

To demonstrate the effectiveness of the proposed method under varying load torques, the motor is operated at an elevated load torque of 2.8 Nm while maintaining the same reference speed of 380 rpm. In order to achieve the specified load torque, the motor draws a current of 10 A per phase, as illustrated in Figure 2.14. It can be inferred that the counter value remains same at different loading conditions for the fault-free and faulty operation for the 4% ITSC. In addition, to showcase the robustness of the proposed technique across different motor speeds, an experiment is conducted at 600 rpm with a load torque of 0.6 Nm. The results demonstrate that the proposed method effectively detects a 4% ITSC over a phase at 600 rpm, as shown in Figure 2.15.

2.4.4 Reliability of the Diagnosis Technique

An advanced diagnostic technique should be capable of handling changes in the load and speed of the motor. The signals used for diagnosis or the fault indicators should remain unaffected by any fluctuations in load or speed. This feature is essential to prevent the diagnosis system from being falsely triggered and to ensure that the indicators show minimal to no alterations when any of the operating conditions change. Therefore, to prove the robustness of the diagnosis technique, the experiments were carried out by subjecting the motor to severe load change and load mutation.

The motor is subjected to a load alteration going from 0.6 Nm to 2.8 Nm, and then the

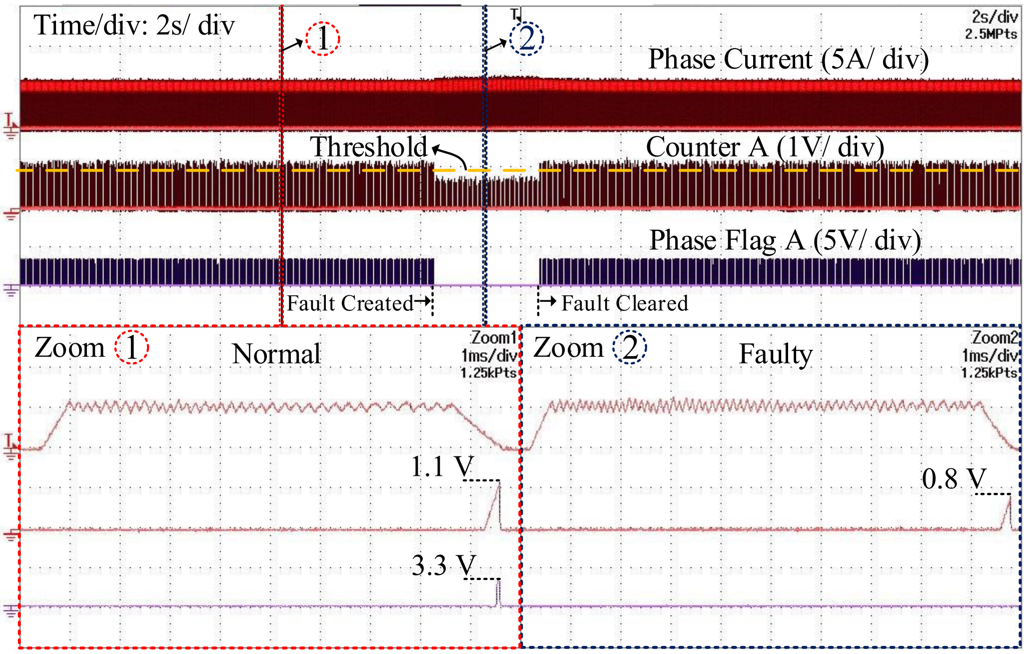

Figure 2.13: Phase *A* current, counter *A* output, and phase *A* flag for 4% ITSC in phase *A* at 380 rpm and 0.6 Nm of load torque.

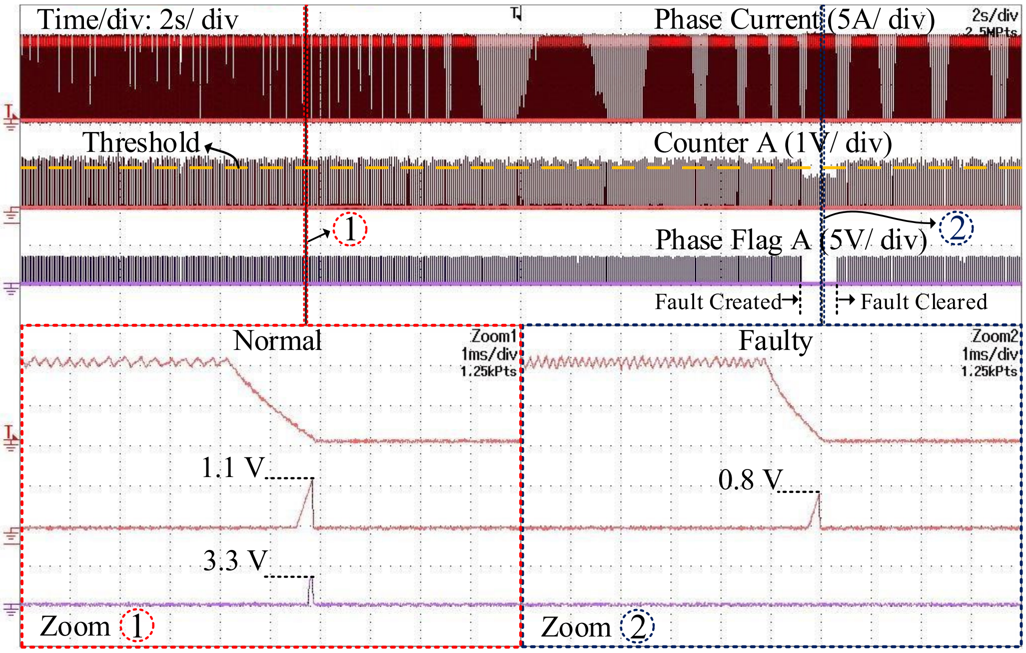

Figure 2.14: Phase A current, counter A output, and phase A flag for 4% ITSC in phase A at 380 rpm and 2.8 Nm of load torque.

load was returned to its initial operational state, as shown in Figure 2.16. The current has increased from the original 5 A to approximately 10 A during this load change and then reverted back as the load is released. The counter value exhibited minimal fluctuations, which in turn does not force any variation in the phase flag. It appears in the tracking zone, presenting a healthy winding condition depicted in the zoom window-1 of Figure 2.16. These findings demonstrate that the diagnostic signal remains unaffected by variations in

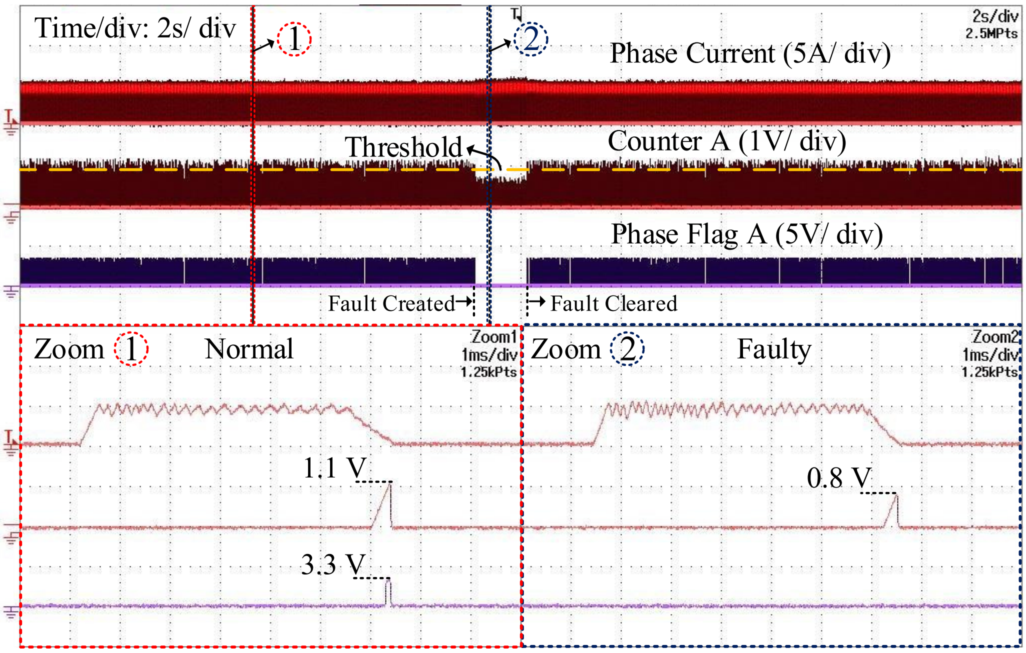

Figure 2.15: Phase A current, counter A output, and phase A flag for 4% ITSC in phase A at 600 rpm and 0.6 Nm of load torque.

load, highlighting the immunity of the proposed method to load changes. Additionally, it verifies that the saturation effect occurring at higher loads does not impact the effectiveness of the diagnosis scheme.

Figure 2.17 depicts a scenario where ITSC occurs amidst a load change. Specifically, a 4% ITSC is created in phase A while the motor is experiencing a load alteration. The characteristic of the diagnosis signal or the output of the counter, remains unchanged. Its value remains the same during both normal and faulty conditions, similar to what was observed in previous cases. This consistency is emphasized in zoom window-1 & 2 of Figure 2.17. Furthermore, the speed varies as a result of the load changes occurring under closed-loop control. However, these fluctuations in speed do not significantly impact the fault indicator.

An experiment was carried out where a 4% ITSC was created in phase A under different operating speeds (varied from 240 rpm to 420 rpm), as illustrated in Figure 2.18. The results shows that there is a negligible difference in the counter output under the initial and final speeds. The output of the counter matches the values observed in previous cases (1.1 V for normal conditions and 0.8 V for 4% ITSC). Additionally, there are minimal fluctuations during the period of transition within which the speed changes. This confirms the reliability of the fault indicator during speed transitions, effectively preventing any unnecessary false alarms.

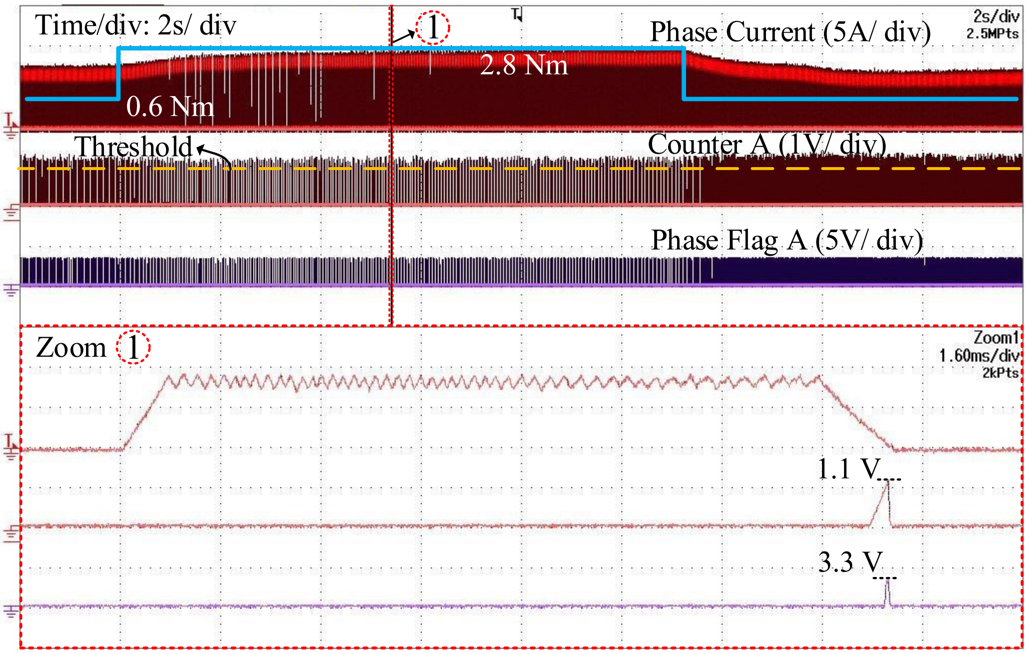

Figure 2.16: Phase A current, counter A output, and phase A flag for normal operation at 380 rpm and load variation from 0.6 Nm to 2.8 Nm.

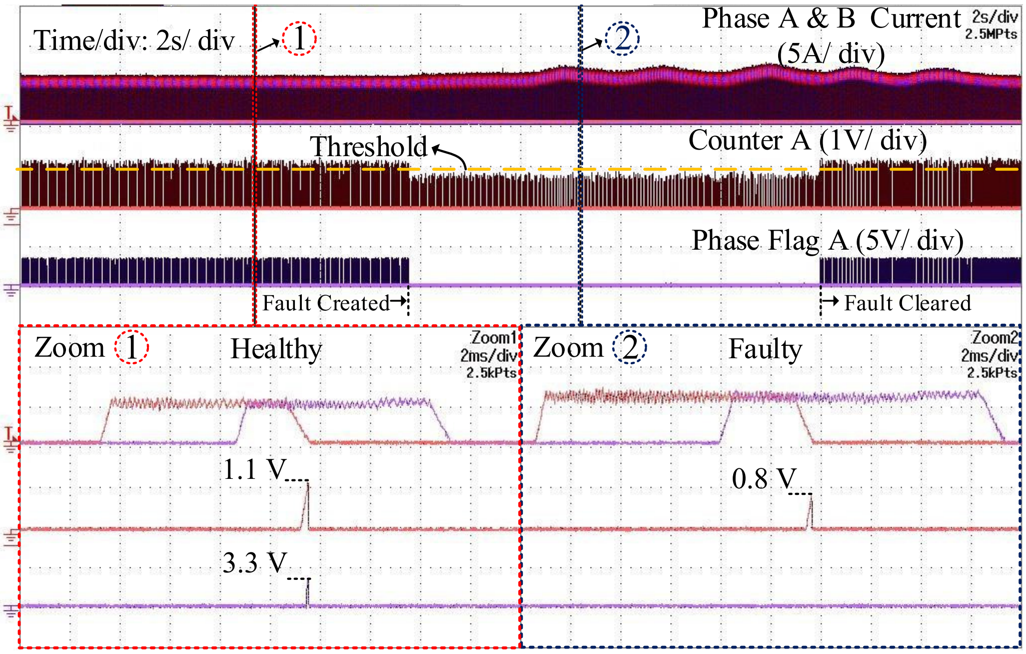

Figure 2.17: Phase A current, counter A output, and phase A flag for normal operation at 380 rpm and load variation from 0.6 Nm to 2.8 Nm.

2.4.5 Severity of the ITSCs

Figure 2.19 displays how the peak value of the counter output changes when the motor experiences ITSC of 4%, 16%, and 24% in phase A. The fault is created by shorting the mentioned turns in a single motor run highlighted in the figure. It can be inferred that the peak value decreases as the severity of ITSC increases. Specifically, it reaches values of 0.8

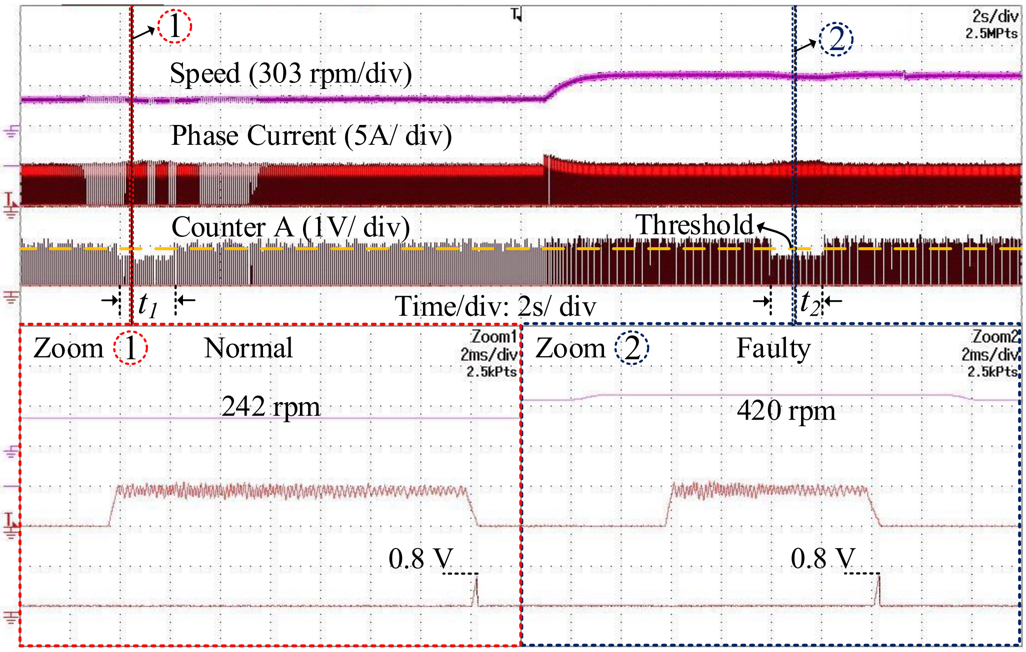

Figure 2.18: Speed, Phase A current, counter A output for 4% ITSC in phase A created under different operating speeds within t_1 & t_2.

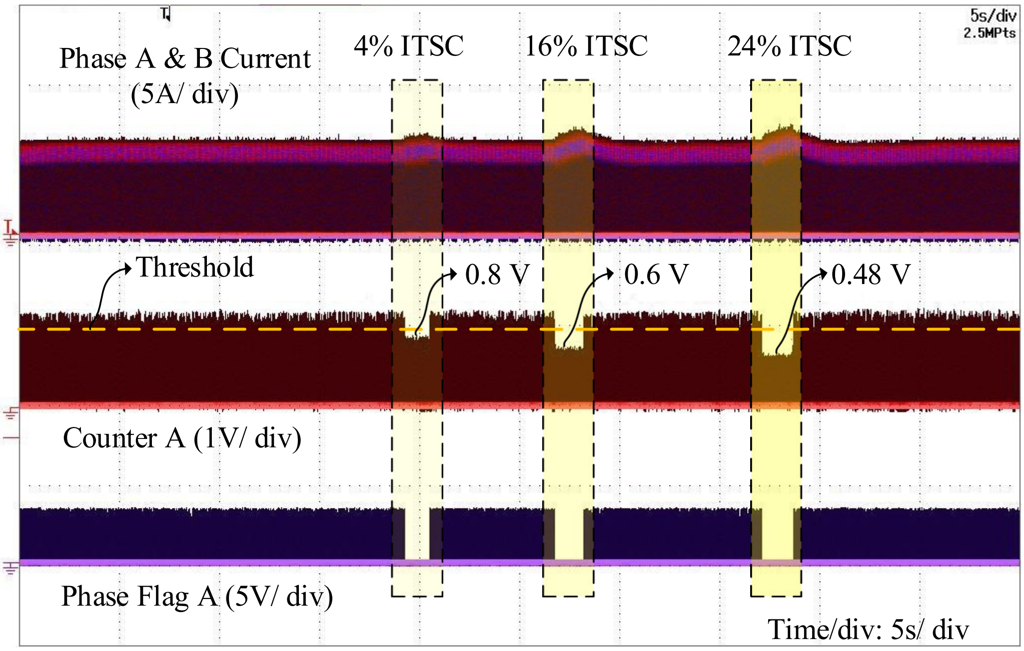

Figure 2.19: Phase A current, counter A output, and phase A flag for 4%, 16% & 24% ITSC in phase A at 380 rpm and 0.6 Nm load torque.

V, 0.6 V, and 0.48 V for ITSC of 4%, 16%, and 24% turns, respectively. It is worth pointing out that there is a significant difference of 0.3 V in peak values between the healthy case and ITSC of 4% turns. This difference is crucial in establishing a threshold voltage to avoid triggering any false alarms. Moreover, it underscores how sensitive the proposed approach is to even minor short-circuits. Table 2.3 provides the calculated severity index values using equation 2.7 for various shorted turns. To roughly estimate the number of shorted turns, it be can referred to Figure 2.20, which illustrates the relationship between the percentage of shorted turns and the severity index (SI). For instance, if SI value falls between 0.3 and 0.4, the plot suggests an ITSC of around 8-15% turns.

2.4.6 Comparison with Existing Methods regarding Sensitivity

Many of the existing approaches have primarily focused on identifying ITSCs involving a substantial number of turns, where the signs of the fault are quite evident. However, these methods tend to overlook or disregard minor fault scenarios. For instance, in a previous study [36], the effectiveness of the method was confirmed only when at least 12.5% of the turns were short-circuited. Another technique, discussed in reference [30], utilizes a

Table 2.3: Severity index for ITSC

Conditions	**Peak value (Volts)**	**Severity index (SI)**
Normal	1.1 V	0
ITSC-4%	0.8 V	0.27
ITSC-16%	0.6 V	0.45
ITSC-24%	0.48 V	0.56

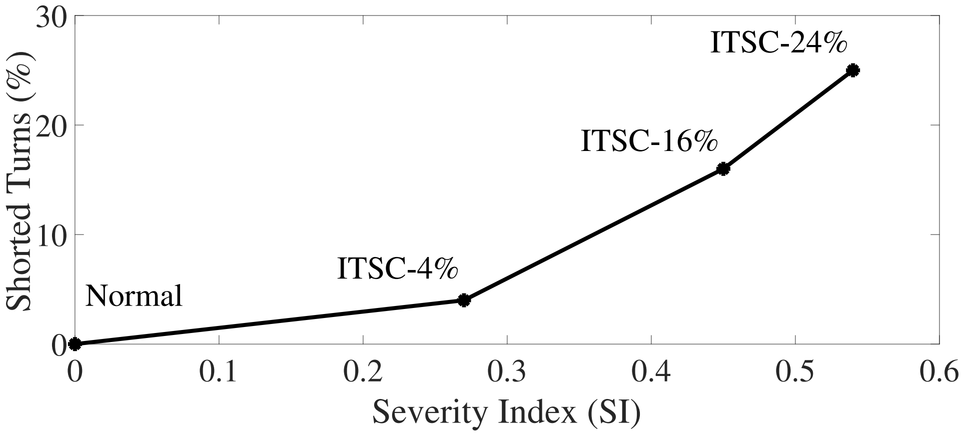

Figure 2.20: Severity plot to estimate the number of shorted turns.

Kalman filter to estimate phase resistance and can successfully identify faults when as few as 5% (equivalent to 20 turns out of 400) are shorted within a phase. In another study described in [25] expanded its application to recognize faults as low as 25% across a phase containing 72 turns. Also, the method is reliable only with a short-circuit of over 50%. The proposed technique in this chapter can detect ITSC of as low as 4 turns (≈4% of 108 turns over a phase), demonstrating a higher sensitivity than most conventional methods.

2.5 Conclusions

This chapter introduces an innovative and straightforward approach for diagnosing interturn short circuits (ITSCs) in switched reluctance motors (SRMs) by monitoring the post turn-off phase currents around their aligned rotor positions. This method can effectively detect even minor ITSCs, as low as 4% of turns within a phase, without any errors. This demonstrates its higher sensitivity to minor faults. Additionally, the method enables easy identification of the faulty phase during operation. Detecting such a small number of faulty turns is valuable as it allows maintenance to be performed before the fault worsens and causes more severe motor damage. The proposed approach remains reliable under various load conditions, indicating its robustness. Moreover, the diagnostic logic is designed to prevent saturation effects at higher loads, ensuring that diagnostic signals and fault indicators remain unaffected by any variation in the load torque. One of the advantages of this scheme is its simplicity of implementation, without imposing a complex computational load on the processor. The method operates in the time domain, resulting in fast diagnosis. Importantly, no extra hardware is required for diagnosis, maintaining the cost and complexity of the drive system. It is worth noting that the proposed method is specifically suited for chopped current control and is more applicable to SRMs operating in the constant torque region. The diagnosis hinges on monitoring the decaying post turn-off current within the low torque region around aligned rotor positions. Therefore, careful selection of the conduction angle for the phases is essential to ensure the current decays in the targeted region. The foundation of the proposed diagnosis approach rests on changes in inductance caused by ITSCs. This alteration reduces the desired decay time of the faulty phase current. However, this change in inductance acts oppositely when eccentricity faults are present in the motor. It extends the decay time of the faulty phase currents. This insight opens the possibility of using the proposed method for comprehensive eccentricity fault diagnosis, which could be explored in future research efforts.

Chapter 3

Control-Independent Diagnosis Technique for ITSCs in SRMs for Entire Speed Range

---

3.1 Introduction

The present chapter introduces a diagnosis technique for ITSCs in SRMs independent of control strategies overcoming the limitations of the technique discussed in the previous chapter. The essence of the proposed method, along with some of its major features, are enumerated here:

1) High-frequency voltage signals are introduced into the phases that do not contribute to torque production or are inactive in each electrical cycle during the motor operation. This signal injection occurs for a specific duration that is predefined. The phase terminals of the phase windings in the SRM are accessed, and the signals are introduced through an auxiliary circuit setup. This injection process stands entirely separate from the power circuit utilized for motor control. Because these signals are directed into inactive phases and the auxiliary circuit is not linked to the power circuit, this technique can be employed for SRMs independent of control strategies.

2) This method examines changes in winding characteristics, such as resistance and inductance, caused by ITSC. It can identify even a short circuit involving just 2 turns (equivalent to 4% of the total turns over one pole). It showcases a heightened ability to detect minor ITSC instances. Additionally, the method can provide a rough estimation of the number of shorted turns, giving insight into the severity of the fault.

3) In SRMs, the inductance of any phase is dependent on both the rotor position and the phase current. When the phase being injected is not drawing current from the power circuit, the inductance becomes solely dependent on the rotor position during the injection interval. As a result, any variation in inductance experienced by the injected voltage signal remains separate from load currents. So, the diagnosis technique remains unaffected by any load variation exhibiting good detection reliability. Furthermore, the effectiveness of the technique remains unaffected by changes in the motor speed, maintaining its reliability across various speed variations.

3.2 Effect of ITSCs in SRMs for different Control Strategies

Figure 3.1 illustrates the model of an 8/6 SRM along with the winding arrangement, specifically highlighting coil A_1 of phase A. Under normal operation, the flux distribution remains balanced and uniform within each excited stator pole. However, this symmetry is disrupted if any fault arises in the winding. The self-inductance and resistance of the faulty winding decrease proportionally to the extent of shorted turns. Additionally, there is a noticeable increase in mutual inductance between the neighboring healthy and faulty phases. In cases of ITSCs, with a fixed phase current i_1, two primary factors contribute to the reduction in flux. First, the diminished number of active turns leads to decreased flux generation. Second, the presence of a short-circuit current i_3 in the shorted turns counteracts the flux buildup. These two factors lead to a decrease in the magnetic co-energy denoted as W, which is expressed as

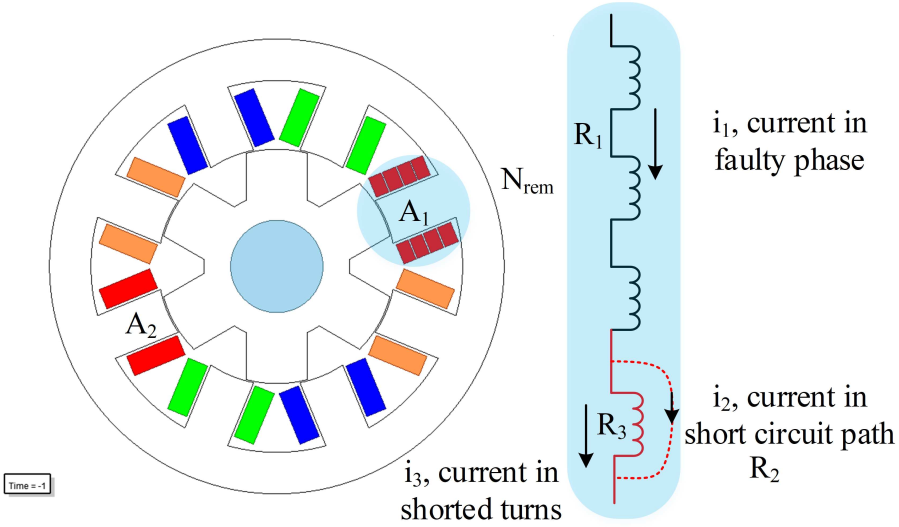

Figure 3.1: One pole ITSC in phase A.

$$W = \sum_{h=1}^{N_h} \int_0^{i_1} \phi_h(i,\theta), di, \tag{3.1}$$

where θ represents the rotor position, N_h accounts for the remaining healthy turns, and ϕ_h signifies the flux linked by these healthy turns. As a result of this co-energy reduction due to the fault, there is a subsequent decrease in the electromagnetic torque T_{elec}, which originates from the faulty phase. This torque is mathematically described as

$$T_{elec} = \frac{\partial W}{\partial \theta}. \tag{3.2}$$

also reduces. In CCC, when maintaining a fixed reference current, the phase current remains at a standard level i_1 regardless of any short-circuit occurrence. Consequently, the torque of the faulty phase is reduced proportionally. As a consequence, the overall machine torque decreases while torque ripple increases. In a closed-loop control scenario, the current reference must be increased to uphold the torque demand when ITSC occurs. In angle position control (APC), the applied phase voltage V_{dc}, phase current i_1, and flux linkages in each phase are interconnected as follows:

$$V_{dc} = i_1 R_{ph} + \sum_{h=1}^{N_h} \frac{d\phi_h(i,\theta)}{dt}, \tag{3.3}$$

where R signifies the phase resistance. Given that the flux linkage of the faulty phase diminishes in the presence of an ITSC, and since U remains constant, the current i_1 increases to counterbalance the decrease in flux linkage. Consequently, the torque generated by the faulty phase, which relies on the square of the phase current, experiences an increase. Simultaneously, there is a notable increase in torque ripple, leading to a substantial force imbalance within the machine. The effect of ITSCs under CCC has already been discussed in Chapter 2. However, to highlight the effect of ITSC in SRMs under different control strategies, these are again discussed here for clarity.

It can be concluded that the response of an SRM to winding faults is inconsistent across all control techniques. As explained, various machine parameters, such as phase currents and torque, exhibit distinct behaviors. It is plausible that these variables might display diverse fault patterns under different control strategies. It highlights that a diagnostic approach tailored for an SRM operating under a specific control scheme might not translate effectively to other schemes. The method proposed in this paper effectively addresses

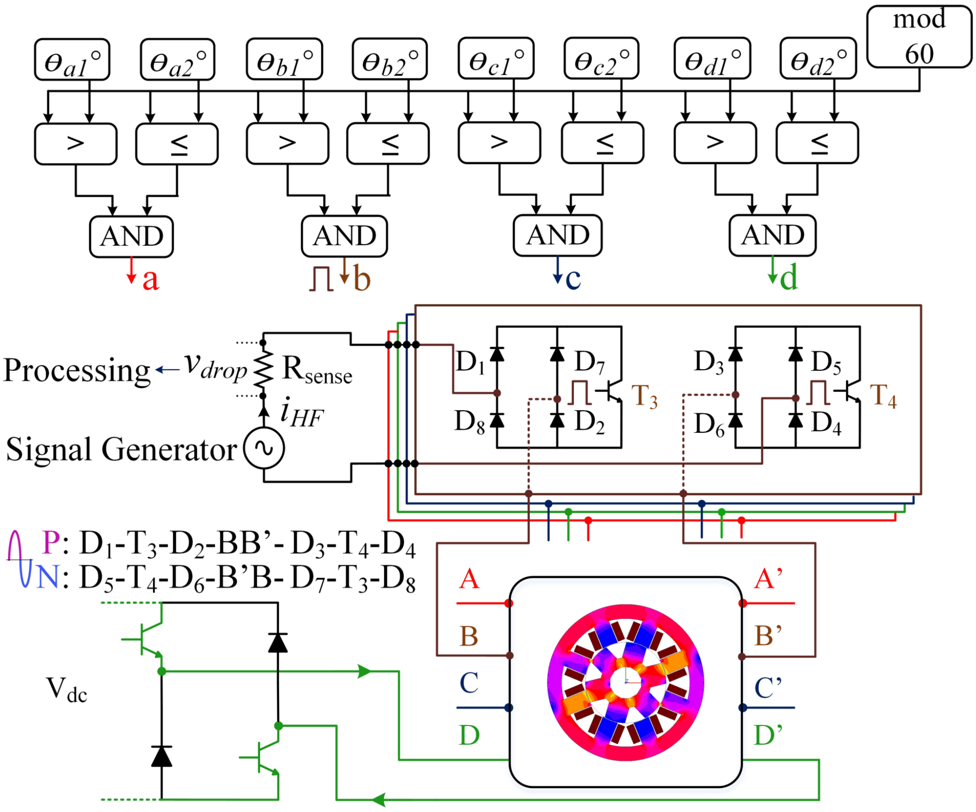

Figure 3.2: Injection logic for 8/6 SRM.

this variability, ensuring its applicability regardless of the control strategy in use. This method tackles the uncertainty associated with different control approaches, diagnosing ITSC independently of control schemes.

3.3 Principle of the Diagnosis Technique

3.3.1 Theoretical Analysis of the Diagnosis Technique

An 8/6 SRM is operated using an asymmetric half-bridge converter with single-phase excitation, depicted in Figure 3.2. The feedback of the motor speed is acquired to determine the rotor position. The speed signal is integrated, and then modulo-60 is taken to capture information about the electrical cycle, as shown in Figure 3.3. As discussed previously, not all phases of an SRM are actively involved in torque production at any given moment. The idle or inactive phase is chosen for signal injection, with a predetermined ratio within each electrical cycle. This approach can also be extended to SRMs with different pole configurations, such as 6/4 or others with higher pole counts. This adaptability makes the technique suitable for SRMs with 3 or more phases. In the 8/6 configuration, the phase quadrant to the active phase is the most suitable choice for signal injection, mainly due to its minimal mutual effect. The process involves introducing a

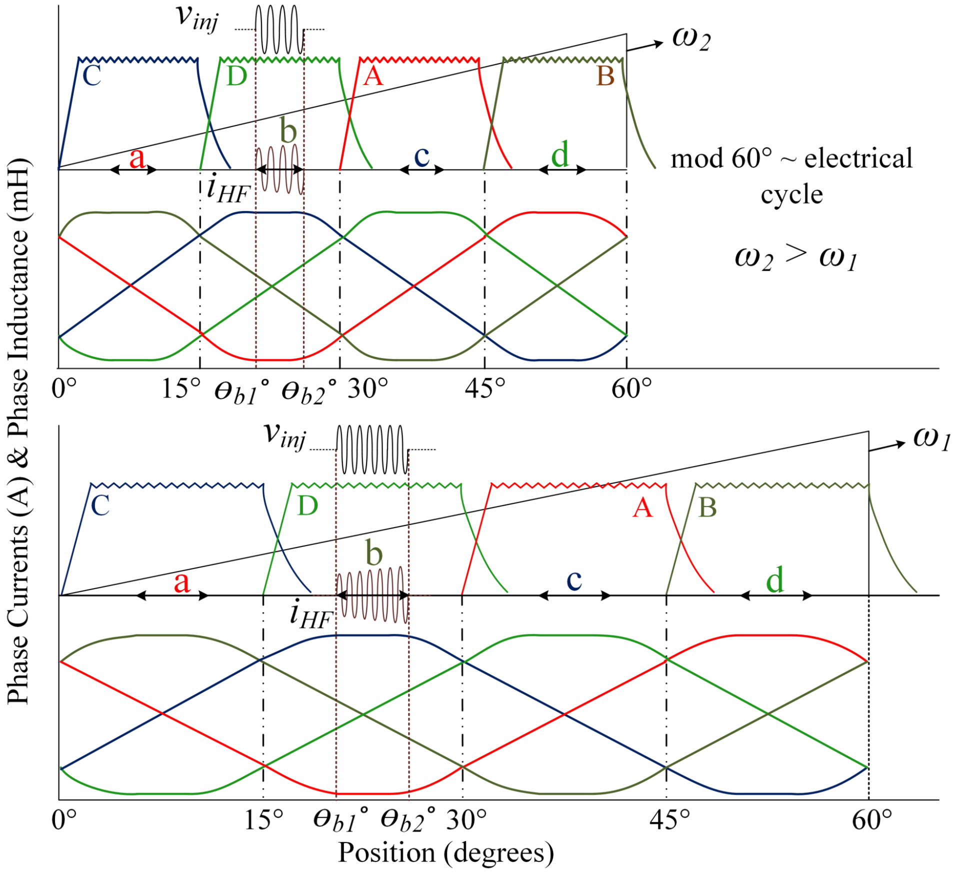

Figure 3.3: Auto-adjustment of injection duration with variation in speed.

high-frequency sinusoidal signal at low voltage into the phase windings at various instants. For illustration, the injection is showcased specifically in phase B, achieved by accessing its winding terminals through an injection circuitry arrangement, as depicted in Figure 3.2. A bidirectional switching setup handles both the positive and negative portions of the sinusoidal signal. The switches T_3 and T_4 are simultaneously activated to establish a connection between the signal generator and the winding terminals of phase B, as shown. The pathways for conducting both the positive and negative portions of the injected signal are also outlined. The voltage drop across the sense resistor R_{sense} is further processed to facilitate the diagnosis of faulty conditions.

In SRMs, any phase is activated when its inductance profile exhibits a positive slope, indicating positive torque generation. For comprehension, consider phase D participating in torque generation between 15° and 30°, as demonstrated in Figure 3.3. During this interval, the rotor poles shift from being aligned to an unaligned position for quadrant phase B. A high-frequency signal is introduced into the winding of phase B for an injection width θ°_{b1} - θ°_{b2}. Similarly, for other phases, injection occurs with the same injection width whenever the corresponding quadrant phases are involved in torque production. In each electrical cycle, high-frequency currents emerge at four distinct moments, as indicated by the double-headed arrows in 3.3. The magnitude of the current exhibits an upward trend, indicating a negative slope in the inductance variation. For a fixed injection width (θ°_{b1} - θ°_{b2}), a higher motor speed ($\omega_2 > \omega_1$) would result in fewer injected cycles, as depicted.

The peak of the high-frequency current ($i_{peak(h)}$) occurs roughly around the position θ°_{b2}, which aligns with the inductance value $L_b(\theta_{b2})$ illustrated in Figure 3.4(a). In SRMs, the inductance is influenced by the rotor position due to changing reluctance. Even with changes in speed that lead to variations in the number of injected cycles, the peak of the high-frequency current tends to maintain the same value. This consistency arises because the inductance $L_b(\theta_{b2})$ remains unchanged at the position θ°_{b2}, as depicted in Figure 3.4(b).

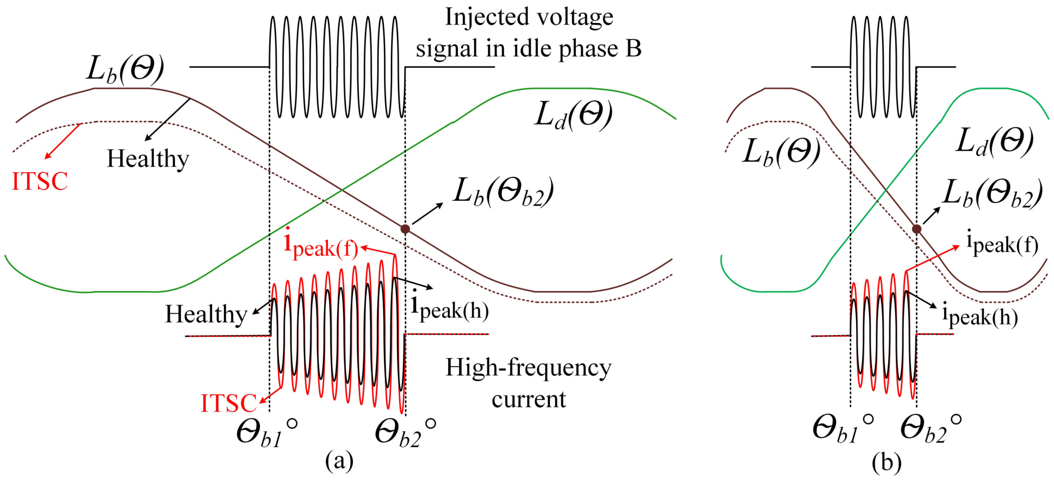

Figure 3.4: Variation in the high-frequency current due to ITSC fault for different speed (ω_2>ω_1) (a) At speed ω_1 *(rad/sec)* (b) At speed ω_2 *(rad/sec)*.

Therefore, the peak of the high-frequency current serves as the key indicator of ITSC in the proposed technique.

Assuming that the pulse period is short enough, the peak current is small, and the voltage in the idle phase winding which is being injected can be approximated as

$$v_{inj} \approx L_b(\theta)\frac{i_{peak}}{\Delta t}, \tag{3.4}$$

where v_{inj} represents the voltage introduced into the idle phase and $L_b(\theta)$ stands for the inductance of phase B. Rearranging (4), it is found that the peak current is inversely proportional to the instantaneous values of phase inductance. Moreover, it also has a reciprocal relationship with the frequency of the injected signal, which remains constant throughout.

$$i_{peak} \approx \frac{v_{inj}\Delta t}{L_b(\theta)} \tag{3.5}$$

Hence, because of the reduced inductance caused by ITSC, the peak of the high-frequency current increases. When an ITSC fault occurs in phase B, the alterations in the inductance characteristics are shown in Figure 3.4, compared to a normal state. The graph also displays the high-frequency current produced in the coil, both for a healthy condition (solid black line) and a faulty condition (red dotted line). The resistance of the affected coil also diminishes; however, its effect is insignificant. With an injection frequency of 30 kHz and an inductance value of, for example, 15 mH at any point within the injection duration, the observed impedance would be around 2826 Ω. This is considering the phase winding resistance as 0.6 Ω, which is very small compared to the impedance offered. Therefore, the instantaneous value of the high-frequency current is mainly influenced by the phase inductance, which increases due to ITSCs. Additionally, it can be concluded that any alterations in resistance due to temperature fluctuations would barely affect the impedance. Consequently, the diagnostic technique remains unaffected by temperature-induced changes in coil resistance.

A threshold is established based on the peak value of the current in the healthy state, denoted as $i_{peak(h)}$. The fault indicator for the affected phase becomes active when the condition $i_{peak(f)} > y \times i_{peak(h)}$ is met. Here, $i_{peak(f)}$ stands for the peak current during a faulty condition, and y represents the threshold factor. The threshold factor is determined through empirical means, involving the observation of the percentage change in peak current values for both healthy and instances with ITSC of 2 turns. These simulations are conducted using finite element method analysis.

3.3.2 Selection of the Frequency of the Injected Signal

The signal injected into the phase windings should have a high frequency due to the following reasons:

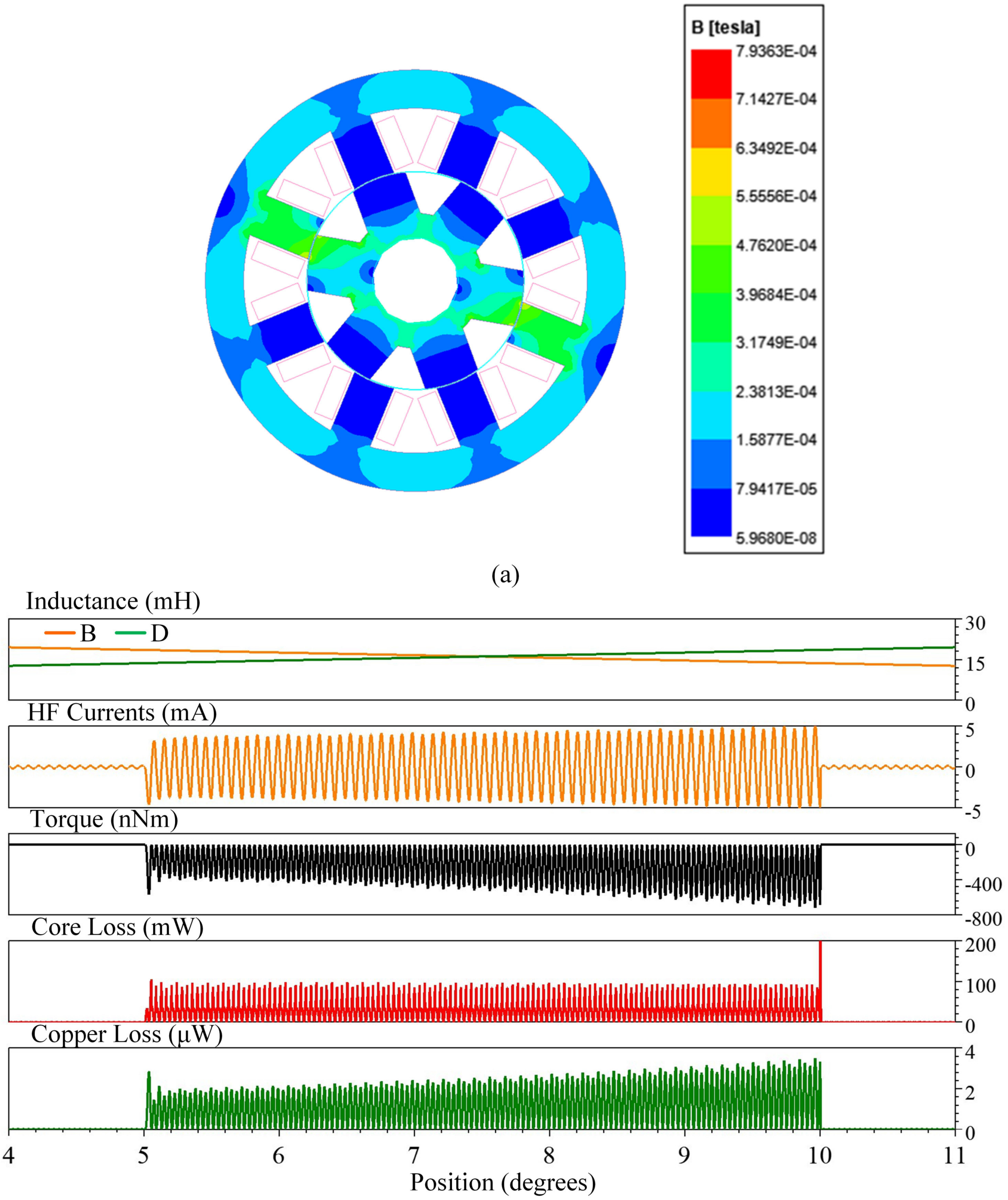

(a)

(b)

Figure 3.5: Effect of signal injection (a) Magnetic field density (b) Phase B and D inductance, HF current in phase B, Torque, Core Loss and Copper Loss.

1) In the idle or inactive phases, switching noises result from the mutual interaction between the active and inactive phases. These noises mix with the injected signal, causing distortions. An accurate pass band filter is needed to prevent unwanted components from affecting the injected signal. The size of the filter components depends on the frequency, which reduces as the frequency of interest increases.

2) From 3.5, it becomes evident that the magnitude of the current caused by the injection of high-frequency voltage is inverse to the frequency. As the frequency rises, the

magnitude of the current diminishes. FEM simulations are performed to analyze the effect of injection on the performance of the motor. In this analysis, a sinusoidal signal with an amplitude of 15V at 30 kHz is injected into Phase B for 5 degrees. Additionally, the rotor is intentionally rotated during this process. The choice of a 15V signal amplitude is practical for generating and handling a high-frequency signal at that voltage level. This amplitude ensures that the injected current would not lead to significant torque generation or losses. The outcomes in terms of torque and losses for each phase resulting from the injection are depicted in Figure 3.5. It is clear from the results that the produced torque is negligible. Moreover, the losses remain insignificant due to the relatively small current magnitude and low flux density.

3) As the speed increases, the injection duration naturally decreases, as already discussed. Additionally, the method utilizes a band-pass filter, and its output takes some time to stabilize after the injection. Consequently, this filtering process makes a portion of the cycles ineffective. Choosing a frequency that allows a sufficient number of useful cycles to be injected is important to ensure accurate collection of the fault index. Considering factors like the rated speed of the motor, injection duration, and the settling time of the filter, a frequency of 30 kHz is adopted for the injection. Figure 3.6 illustrates the filtered high-frequency currents injected at 30 kHz over an injection period of 5 degrees, at speeds of 380 rpm and the rated speed of 1200 rpm. The encircled indicates the settling time of the filter, and the dashed arrows demonstrate the inductance variation imitated by the high-frequency current. It is apparent that by choosing 30 kHz, enough useful cycles are secured for injection across the entire speed range up to the rated speed, ensuring accurate fault detection. The peak value remains consistent for both scenarios, as previously discussed. Moreover, there is flexibility in adjusting the injection duration, allowing for more cycles at the same frequency. Similarly, the frequency can be increased with certain limitations while keeping the injection duration fixed. However, detecting low-amplitude signals at very high frequencies is challenging, and achieving a narrower bandwidth at higher center frequencies makes the filter design more intricate.

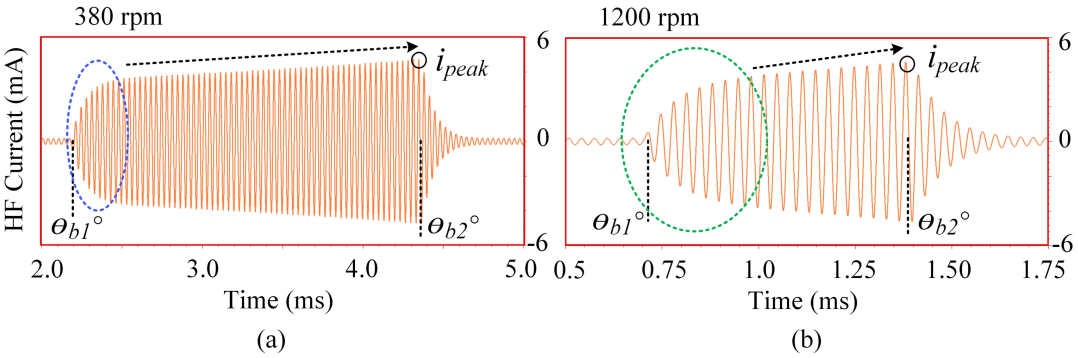

Figure 3.6: Filtered high-frequency currents at 30 kHz for injection width ($\theta_{b1}°$ - $\theta_{b2}°$) of 5° at (a) 380 rpm (b) 1200 rpm.

3.3.3 Effect of Load and Speed Variation on the Fault Indicator

When devising any fault detection method, ensuring reliability is a critical priority. The impact of speed and load variations on the diagnostic arrangement defines the reliability of the algorithm. Injection is performed in the inactive quadrant phase, which is not involved in torque generation. It essentially means that the inductance of this unenergized phase is solely dependent on the rotor position. Consequently, any load torque alterations do not influence the peak value of the high-frequency current. Furthermore, this value remains nearly constant across different speeds, leading to the conclusion that the fault indicator is not affected by changes in speed.

3.4 Experimental Validation & Results

3.4.1 Experimental Setup

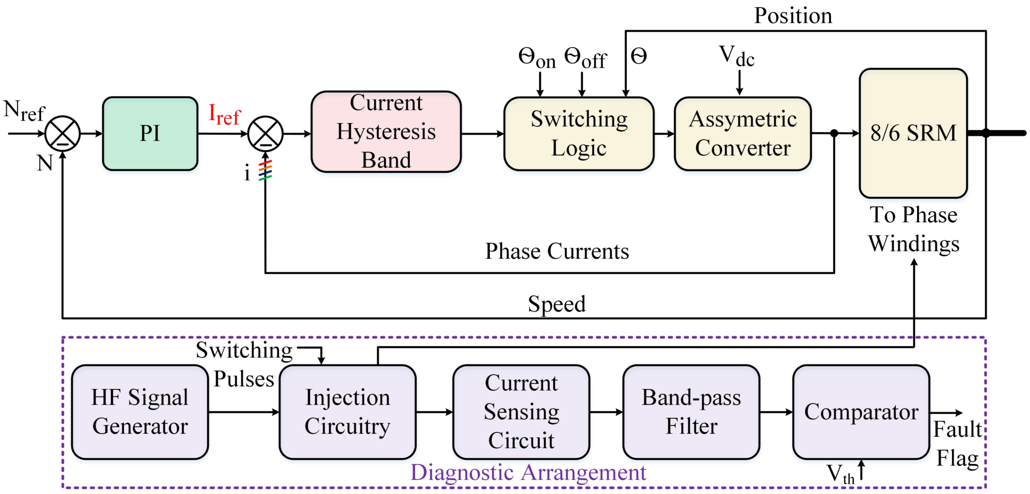

Figure 3.7: Overall block representation of the drive with diagnostic arrangement.

The complete block diagram illustrating the 8/6 SRM drive with the integrated diagnostic setup is depicted in Figure 3.7. As mentioned, the presented approach is tested and confirmed under two control strategies. Under the CCC strategy, the phase currents of the SRM are controlled to align with a reference value computed based on the desired speed and a specific load torque demand. The motor is additionally operated at its rated

Table 3.1: Specifications of 8/6 SRM

Parameter	**Value**	**Parameter**	**Value**
Rated output power	1 hp	Stack length	102 mm
Rated input voltage	72 V	No. of poles (Stator/Rotor)	8/6
Rated speed	1200 rpm	Phase resistance	0.6 Ω
Stator outer diameter	165 mm	Stator pole arc	22.5°
Stator inner diameter	85 mm	Rotor pole arc	30°
Rotor outer diameter	84.5 mm	Number of turns/pole	54
Rotor inner diameter	33.5 mm	Air gap	0.5 mm

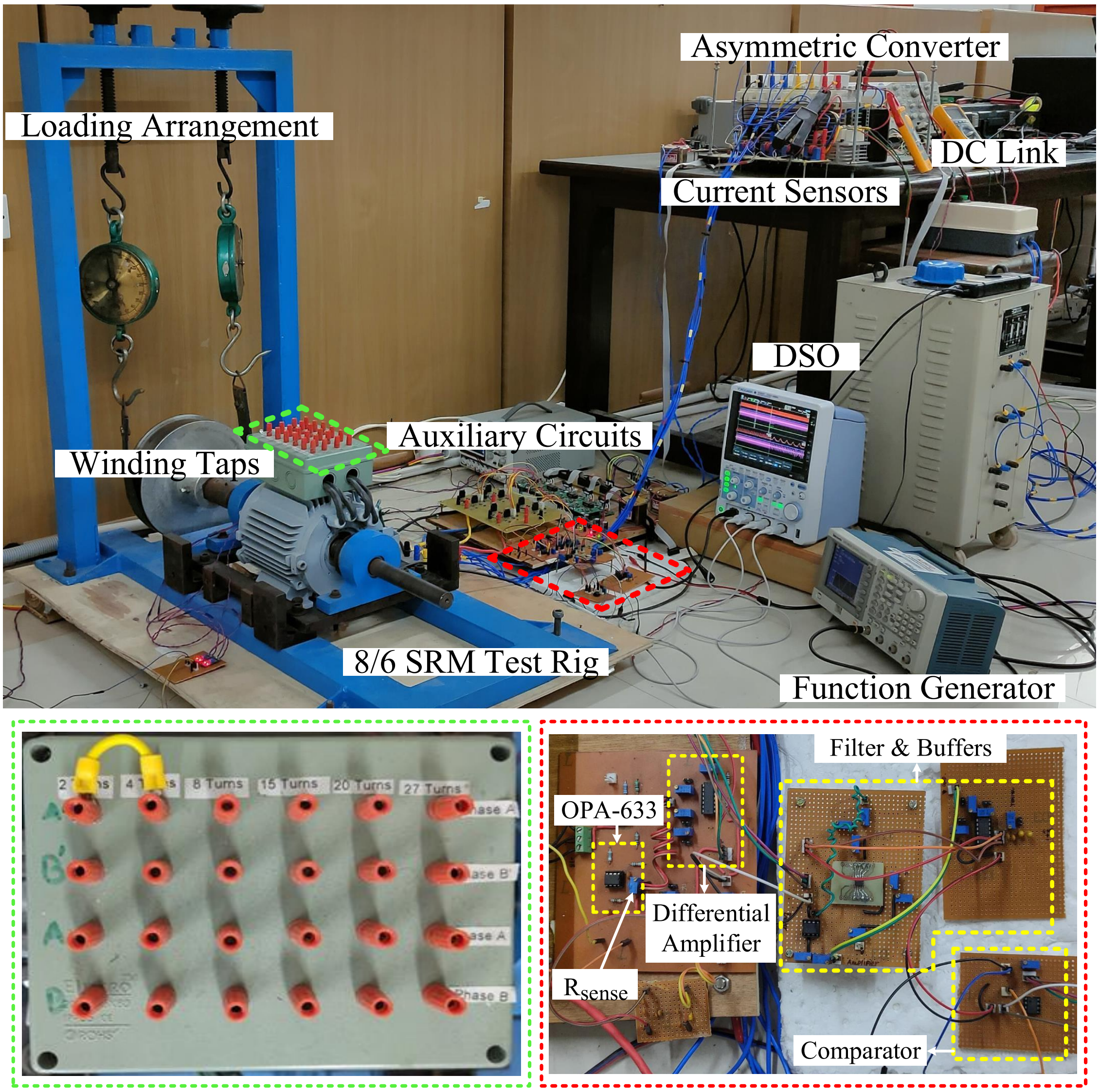

Figure 3.8: Experimental setup.

speed using the APC strategy to assess the effectiveness of the proposed technique at higher speeds. A comprehensive explanation of the diagnostic arrangement is provided in the subsequent sections of this chapter.

A testing setup has been developed for an 8/6 SRM with specifications outlined in Table 3.1. This setup is designed to analyze various fault conditions, as illustrated in Figure 3.8. In phases *A* and *B* windings, multiple taps are incorporated to emulate the ITSC faults of varying magnitudes. A conventional AHB converter is built to drive the motor using the Semikron IGBT module SKM100GB12T4. The four-phase currents of the motor are sensed using a Hall-effect-based LA-55 sensor with a bandwidth of DC-200 kHz. These sensed currents are fed back to the controller via analog-to-digital converter channels, forming a crucial part of the control scheme. Additionally, speed feedback is obtained through a Baumer-manufactured incremental encoder, which generates 1000 pulses per revolution. This encoder is synchronized with an absolute encoder to ensure precise rotor position tracking. Control and signal injection logic are implemented in the

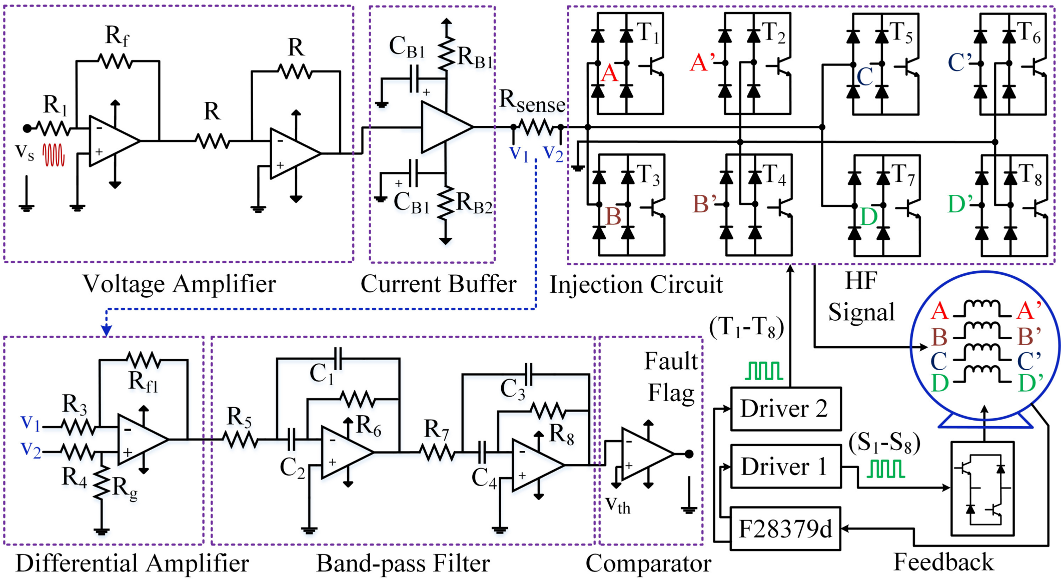

Figure 3.9: Auxiliary circuitry for fault diagnosis.

DSP micro controller TMS320F28379d. The switching signals generated by the controller are then routed to the gate-emitter terminals of the IGBTs employed in both the AHB and the injection circuitry. These signals are facilitated through Skyper 32 PRO drivers. The additional circuitries employed for diagnosing ITSCs are illustrated in Figure 3.9. A function generator is utilized to generate a high-frequency sinusoidal signal, and its current sink capacity has been enhanced to meet the current demand. OPA-633, a current buffer amplifier, as shown in Figures 3.8 and 3.9, is employed for this purpose. The output of this amplifier is directed to the windings following the injection logic detailed previously. The injection circuity is also presented in Figure 3.9. A configuration comprising eight Schottky diodes capable of managing high frequencies, along with two IGBTs, is employed for each phase. In a scenario where phase C is engaged for torque generation between position 15° - 30°, both T_1 and T_2 are triggered concurrently. This action injects a signal into phase A, commencing from the position (θ°_{a1} - θ°_{a2}) as indicated. In a similar fashion, the remaining IGBTs (T_3 - T_8) are controlled for the other phases. The LA-55 current sensors encounter challenges in accurately detecting low-amplitude currents, particularly at higher frequencies. A solution involves incorporating a sense resistor to address this issue. The current readings in the windings are translated in terms of voltage by measuring the voltage drop across this resistor ($v_1 - v_2$). As depicted, a differential amplifier is implemented to sense the voltage drop across the resistor. The amplifier output is then directed to a filtering stage. A two-stage narrow-band pass filter utilizing high-speed Op-Amps THS-4032 to capture the signal at the frequency of the interest. This filter is designed with a center frequency of 30 kHz. The resultant filtered signal is compared against a predefined threshold voltage via an Op-Amp-based comparator. This step serves to identify instances of ITSC and pinpoint the specific faulty phase within the motor.

The experimental results for both CCC and APC are analyzed in detail the subsequent

Table 3.2: Experimental Parameters

Parameter	**CCC**	**APC**
DC Input Voltage, V_{dc}	72 V	72 V
Speed reference, N_{ref}	380 rpm	-
Current Hysteresis Band	±0.4 A	-
Switching frequency	8-12 kHz	-
Nature of HF signal	Sinusoidal	Sinusoidal
Amplitude of HF signal, V_m	15 V	15 V
Frequency, f_{inj}	30 kHz	30 kHz
Injection width for each phase, (θ_1-θ_2)	5°	7°
Cut-off frequency of band-pass filter, (f_H-f_L)	28-32 kHz	28-32 kHz

sections. The parameters used for implementation of the proposed diagnosis technique is tabulated in Table 3.2.

3.4.2 Diagnosis with Chopped Current Control

At a speed of 380 rpm and with a load torque (T_{load}) of 0.5 Nm, the machine draws a reference current of 5 A as depicted in Figure 3.10. Due to the limitations of the channels in the oscilloscope, only the currents for phases A and the quadrant phase C are observed. Zoom window 1 provides a clear visual representation of the filtered high-frequency signal for each phase throughout the machine cycle. As the injection width remains consistent for all phases, the voltage signal encounters similar variations in inductance for each phase in a healthy state. Notably, the peak value of the high-frequency signals for all phases exhibits nearly identical magnitudes, signifying a healthy winding condition. Zoom window 2 highlights the distinctive inductance pattern detected by the injected signal specific to

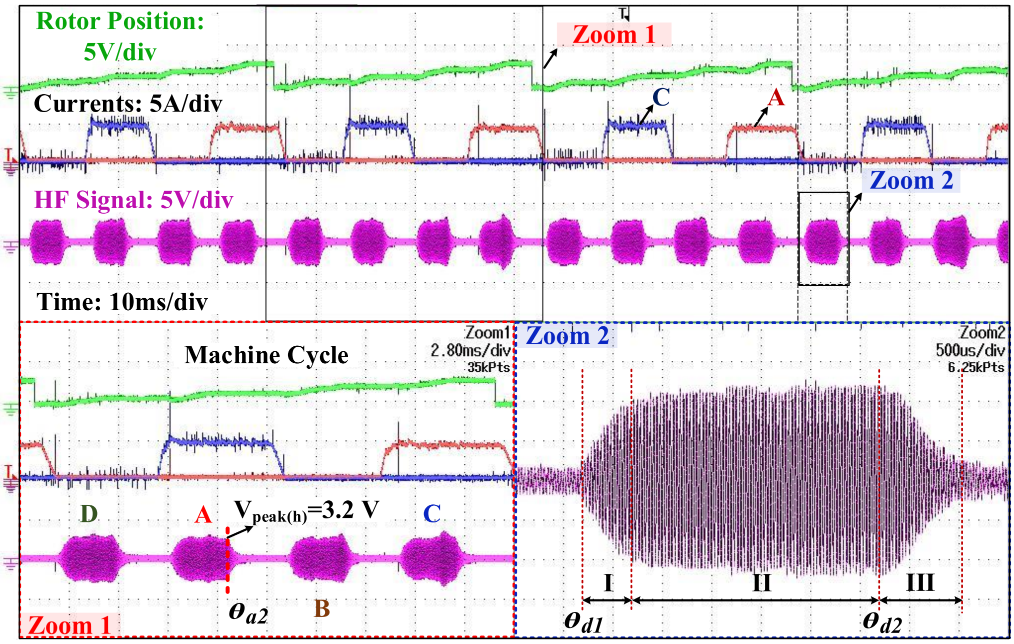

Figure 3.10: Rotor position, phase A & C currents and HF signals for healthy windings condition under CCC.

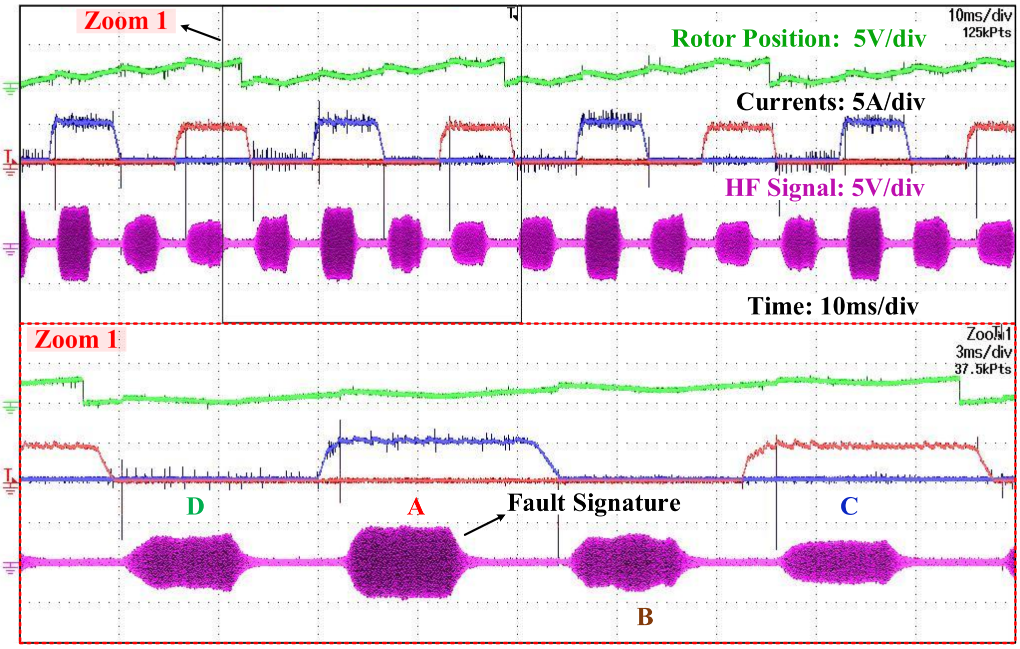

Figure 3.11: Rotor position, phase A & C currents and HF signals for one pole ITSC of 2 turns in phase A under CCC.

phase D. Within this window, Region I spanning ($\theta_{d1}°$-$\theta_{d2}°$) showcases an abrupt variation in magnitude in contrast to Region II. Region I corresponds to the settling time of the filter, where the output stabilizes after a few cycles. In Region II, the period of interest, the magnitude of the high-frequency current increases, as previously discussed. The peak of the signal is observed at around $\theta_{d2}°$, used for identifying the winding conditions. A residual current is present because of the filter after the injection width concludes, but this current diminishes to zero after a few cycles, as illustrated in Region III. Notably, the diagnostic approach remains unaffected by the characteristics of these two regions, namely I and III. Figure 3.11 illustrates a faulty condition where two turns within one of the poles of phase A are short-circuited during the running condition. Despite this fault, there is no significant observable change in the current of phase A. Notably, the high-frequency signal associated with phase A displays an increased magnitude in comparison to the other phases. Minor fluctuations are noticed in the signals of the adjacent phases D and B concerning the faulty phase A. This phenomenon arises due to the substantial rise in mutual interaction between the faulty phase and its adjacent phases, attributed to the ITSCs. Conversely, the signal linked to phase C, situated at a quadrant opposite to the faulty phase A, remains unaffected, as depicted in Figure 3.11. In this proposed method, the fault is detected only when the phase quadrant to the faulty phase is energized for torque production, elaborated and explained in Fig. 3.12.

For the purpose of identifying the onset of ITSCs, a threshold voltage of 3.8 V is employed, which is 1.2 times greater than the peak value observed in the healthy condition. This voltage is compared against the amplitude of the high-frequency signals through a comparator mechanism. The outcome of this comparison functions as a fault indicator, as depicted in Figure 3.12. Notably, during the healthy operation of the motor, the threshold voltage surpasses the peak value of the high-frequency signals. In this situation, the comparator output becomes saturated at -15 V, signifying an absence of faults. This scenario is evident in the zoomed-in section labeled as zoom window 1 in Figure 3.12.

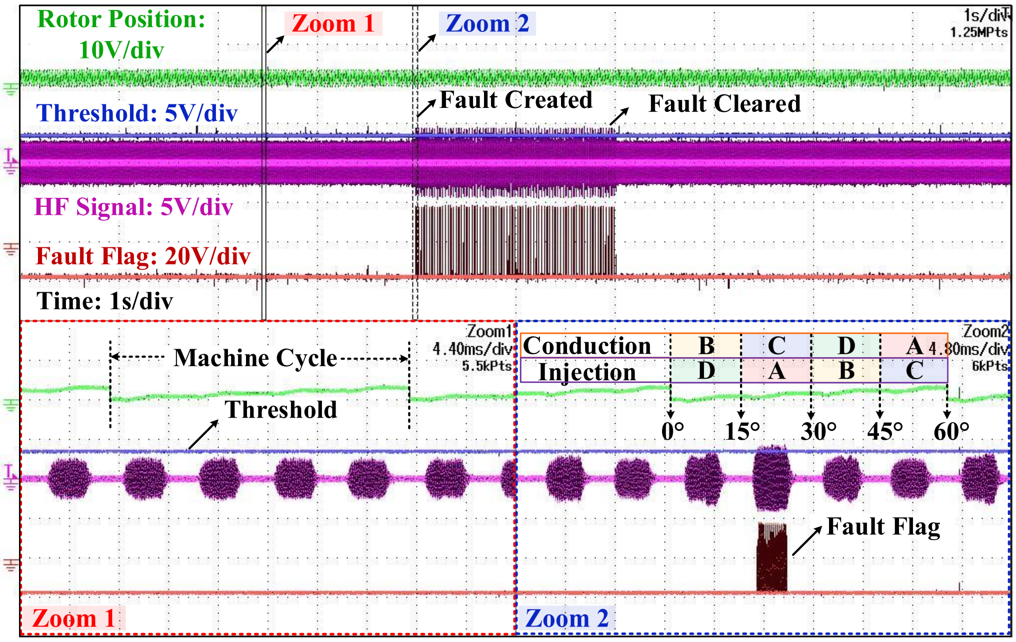

Figure 3.12: Rotor position, threshold voltage, HF signals and fault flag depicting the dynamics for healthy and faulty conditions under CCC.

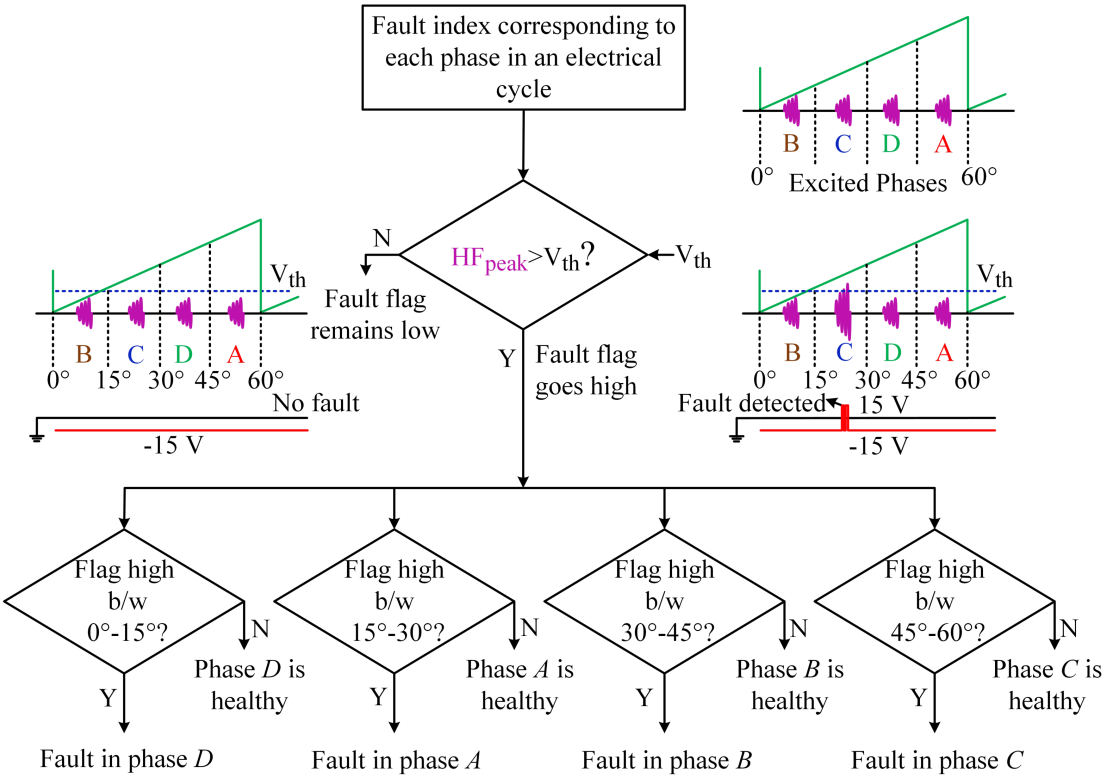

Figure 3.13: Flow chart depicting fault detection and faulty phase identification.

For the identification of the faulty phase, it becomes necessary to have access to information regarding the position of the rotor. The activation of each phase relies on the rising slope of the inductance profile, which depends on the rotor position. In our control scheme, phase C is being activated between 15°-30° for positive torque production. The quadrant phase A is being injected for which the flag goes high in between 15°-30°, shown in zoom window 2 of Fig. 3.12. When the flag rises while phase C is conducting, it signifies the occurrence of a fault in phase A. Likewise, if the fault flag becomes elevated within the 45°-60°, the faulty phase can be identified as C. Merely monitoring the flag status and the position at which it becomes high provides insight into the faulty phase. This process is elucidated in the flowchart illustrated in Figure 3.13.

3.4.3 Severity of the ITSCs

Figure 3.14(a) and (b) displays the peak of the high-frequency signal in the case of single pole ITSC, involving 2 turns (equivalent to 4%) and 27 turns (equivalent to 50%) within phase A, respectively. It is used to roughly approximate the number of shorted turns, i.e., the severity of the ITSC. The peak value increases with the increasing severity. For instances of 4% and 50% ITSC, the corresponding peak values are 4.6 V and 5.1 V, in comparison to the value of 3.2 V recorded for a healthy state ($v_{peak(h)}$). Figure 3.11 depicts the peak value corresponding to the healthy condition. A significant difference of 1.4 V is evident between the peak values of the healthy and 4% ITSC conditions. This distinction proves substantial enough to establish a threshold voltage, thereby preventing any inadvertent triggering of the fault indicator. Additionally, this difference confirms the increased sensitivity of the proposed technique in detecting even minor instances of ITSC

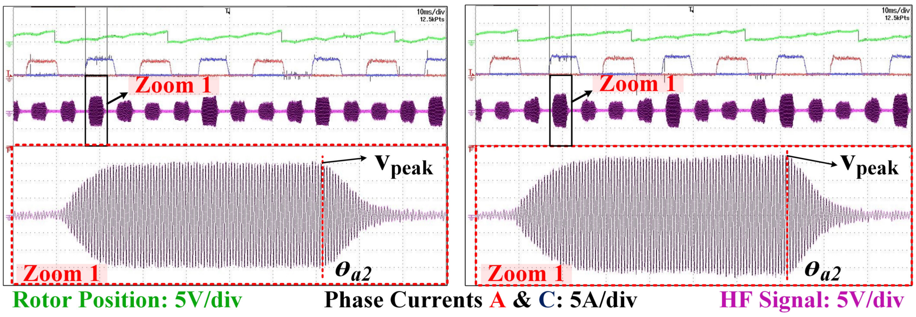

(a) (b)

Condition	v_{peak}(V)	SI_{ITSC}
Healthy	3.2	0
ITSC-4%	4.6	0.43
ITSC-27%	4.9	0.53
ITSC-50%	5.1	0.59

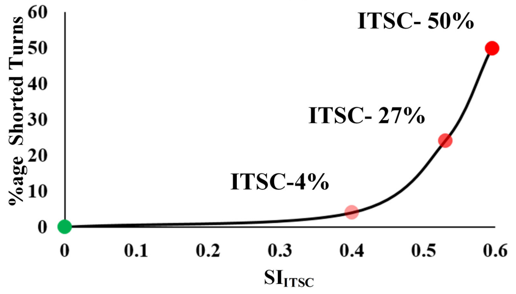

(c)

Figure 3.14: Severity of the ITSC (a) Peak value for 4% ITSC (b) Peak value for 50% ITSC (c) Percentage shorted turns versus SI_{ITSC} plot.

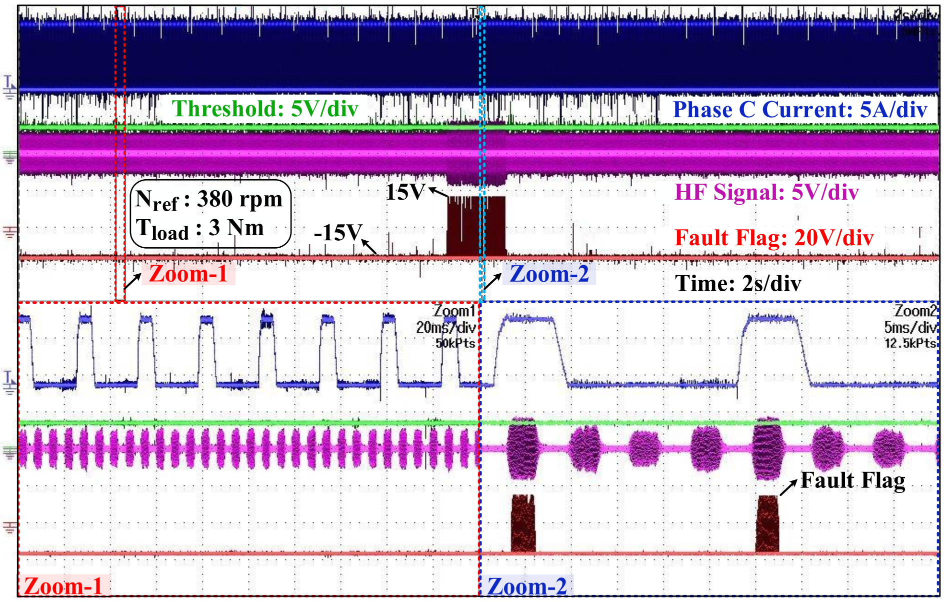

Figure 3.15: Phase C current, threshold voltage, HF signals and fault flag at load torque of 3 Nm operating with CCC.

within the winding.

A normalized severity index SI_{ITSC} is also introduced for enhanced clarity. This index is formulated as follows:

$$SI_{ITSC} = \frac{v_{peak(f)} - v_{peak(h)}}{v_{peak(h)}}, \tag{3.6}$$

where $v_{peak(f)}$ represents the peak value associated with the faulty conditions. The graphical relationship between the percentage of shorted turns and SI_{ITSC} is presented in Figure 3.14(c), facilitating an estimation of the number of shorted turns. When the SI_{ITSC} value falls within the range of 0.5 to 0.55, the percentage of shorted turns can be approximated to be around 20-30%.

3.4.4 Dynamic Behavior of the Diagnosis Technique

Figure 3.15 presents the outcomes obtained when the SRM operates at a constant speed of 380 rpm under an elevated load torque of 3 Nm while experiencing an ITSC involving 2 turns within one of the poles of phase A. In this particular situation, the motor draws a current of approximately 10 A, as demonstrated. In zoom window 1 of the figure, the state before the fault is apparent, wherein the indicators associated with each phase remain below the predetermined threshold limit, as previously discussed. Subsequently, the magnitude of the high-frequency signal linked to the faulty phase A surpasses the threshold value, leading to the saturation of the fault flag at +15 V. It clearly signifies the onset of an ITSC fault, as depicted in zoom window 2 of the figure.

Figure 3.16 illustrates the behavior of the diagnostic approach under varying load conditions. There is an obvious change in the phase current with closed-loop control due to the variation in load torque. However, it is worth highlighting that despite these load fluctuations, the peak amplitude of the high-frequency signals remains relatively consistent. The threshold greater than the peak of the high-frequency current forces the fault flag to be saturated at -15 V, indicating no-fault operation. Under the influence of closed-loop control, the motor encounters speed fluctuations attributed to load variations. These fluctuations are visually demonstrated in the magnified views in zoom windows 1 and 2 of Figure 3.17. When comparing two distinct speeds, 220 rpm and 400 rpm, it becomes evident that the number of cycles injected differs for both cases. This count diminishes for the higher speed of 400 rpm. However, despite these differences, no observable alterations exist in the peak values for both speeds. The fault flag consistently saturates at -15 V, showcasing the immunity of the fault indicator. As outlined previously, the validation of the theoretical basis is confirmed through the results depicted in Figures 3.16 and 3.17. These findings serve to substantiate that the proposed method possesses robust detection reliability.

Furthermore, an assessment of the resilience and efficacy of the proposed method under dynamic conditions is conducted by creating ITSCs during load and speed transients. A single pole ITSC involving 2 turns is introduced in phase *A* while the motor undergoes a load transition, as depicted in zoom window 1 of Figure 3.18. In response to the fault, the fault flag goes high, correlating with the increased peak of the high-frequency signal corresponding to the faulty phase. This response is visually illustrated in zoom window 2 of the figure. Figure 3.18 presents the diagnostic outcome when the motor is subjected to ITSC during a speed transition. In this case, the fault is created in phase *A* as the motor speed is transitioning from 132 rpm to 420 rpm under a load torque of 0.5 Nm. The peak of the fault indicator, corresponding to the injured phase, surpasses the predetermined

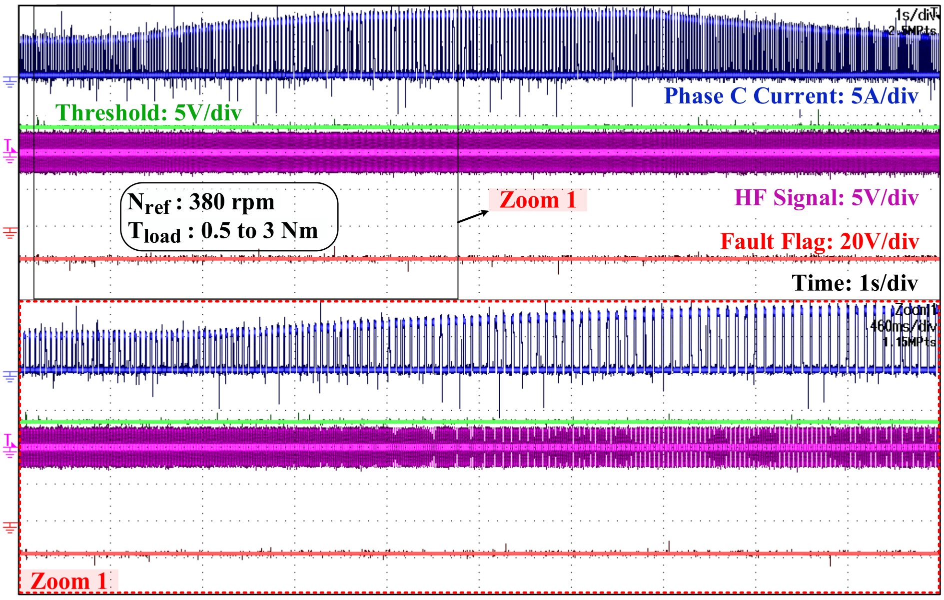

Figure 3.16: Phase *C* current, threshold voltage, HF signals and fault flag under load variation from 0.5 to 3 *Nm* operating with CCC.

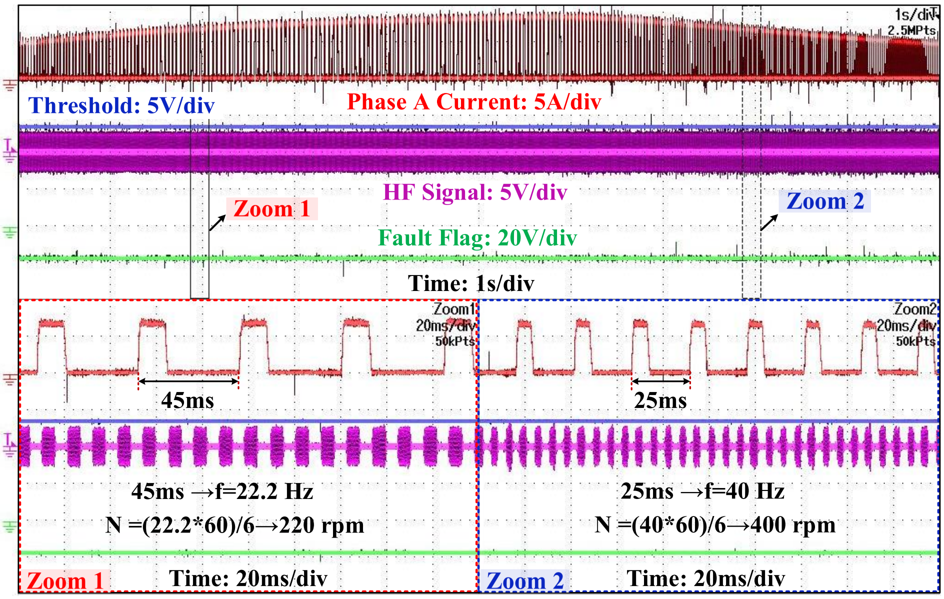

Figure 3.17: Phase A current, threshold voltage, HF signals and fault flag under speed variation operating with CCC.

threshold, leading to the fault flag saturating at +15 V. This phenomenon is distinctly presented in zoom window 1 of Figure 3.19, where the peak of high-frequency current for phase A increases within the period when phase C conducts to generate torque. The initial and final speeds, denoted as 132 rpm and 420 rpm respectively, can be inferred from the frequency of the phase currents as portrayed in zoom windows 2 and 3 of the same figure.

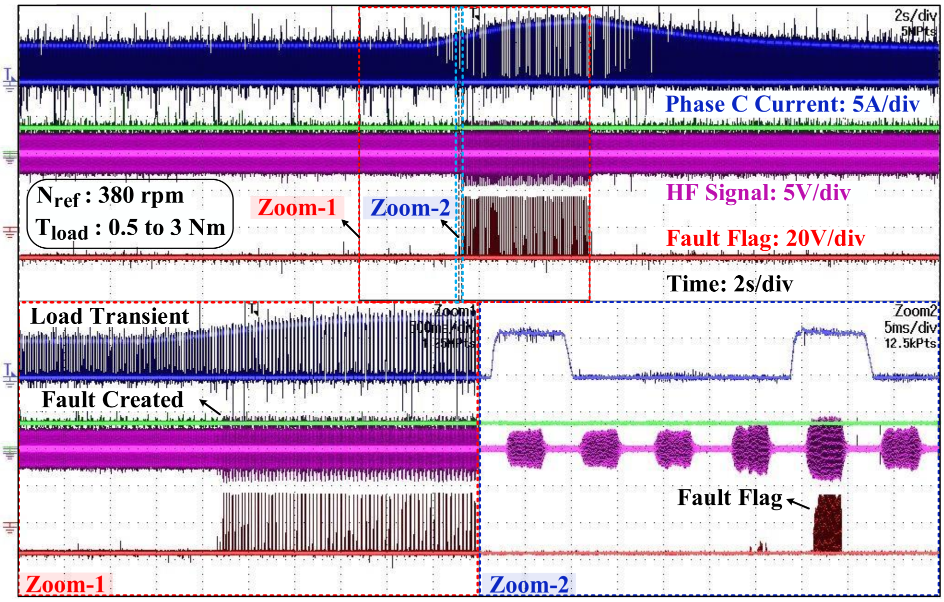

Figure 3.18: Phase A current, threshold voltage, HF signals and fault flag under speed variation operating with CCC.

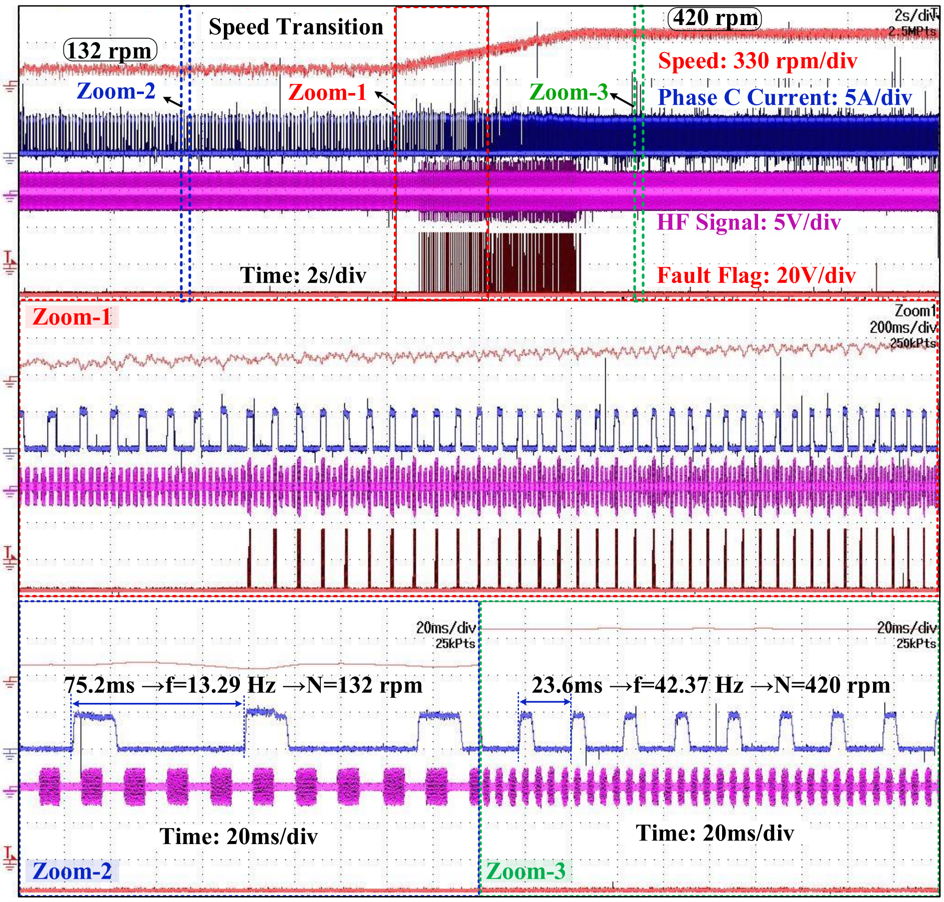

Figure 3.19: Speed, phase C current, HF signals and fault flag when motor is subjected to ITSC during speed transition from 132 *rpm* to 420 *rpm*.

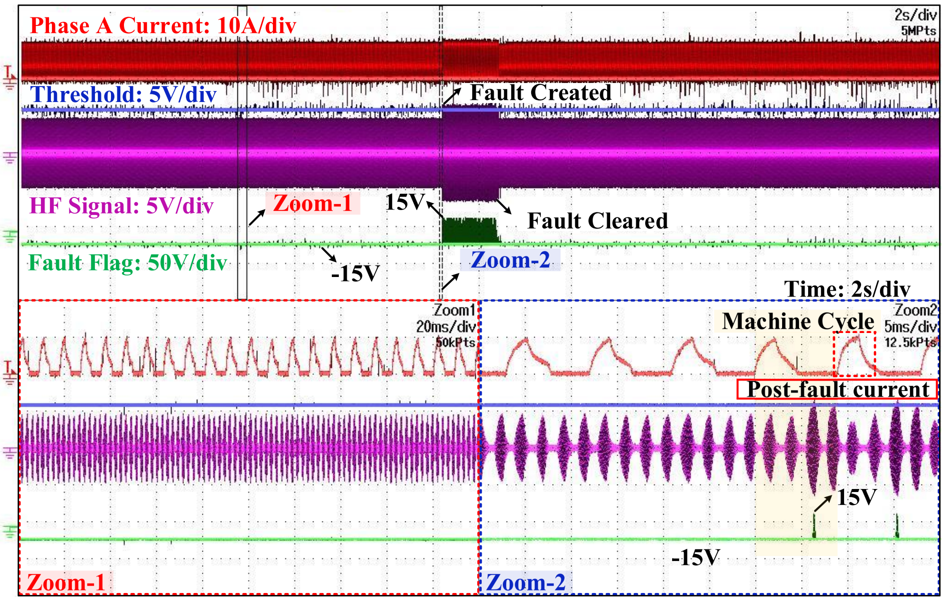

Figure 3.20: Phase A current, threshold voltage, HF signals and fault flag for healthy and faulty condition under APC.

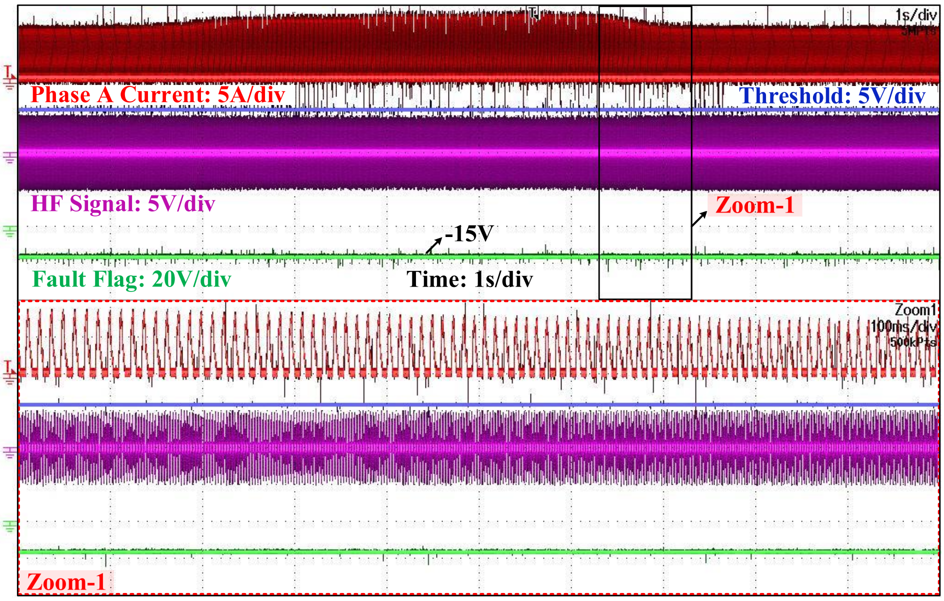

Figure 3.21: Phase *A* current, threshold voltage, HF signals and fault flag for healthy and faulty condition under APC.

3.4.5 Diagnosis under Angle Position Control

The motor is run without any load at a speed of 1150 rpm, achieved by applying the full DC-link voltage. Similar outcomes to those explained under the CCC strategy are obtained using the APC method. Figure 3.20 illustrates the operation of the SRM in both healthy and faulty conditions. The fault-free state is displayed in the first zoom window, where the four-phase high-frequency signals exhibit the same peak values. The threshold voltage consistently remains higher than the peak values, causing the fault flag to saturate at -15 V. One pole ITSC of 2 turns is created in phase A at the instant shown. The effect of ITSCs of larger turns on the magnitude of the faulty phase current of SRM is prominent for APC. However, for minor ITSCs, the effect is not that noticeable, as presented in zoom window 2. Following a fault, the post-fault phase current magnitude does not experience a substantial alteration. As the peak of the injected signal corresponding to the faulty phase increases, the fault flag is raised, indicating an ITSC occurrence. The fault flag returns to the -15 V saturation point once the fault is cleared. Identifying the faulty phase and the extent of the fault can be determined similarly, as discussed under the CCC strategy.

Figure 3.21 displays the behavior of the diagnostic method when the motor is subjected to varying load conditions. Notably, there is no significant impact on the fault indices, and as a result, the fault flag consistently stays at a saturation level of -15 V.

The response time of the diagnosis method depends on the instant the fault occurs and the phase active at that instant. However, the exact time of detection is not certain. At most, it could be slightly less than the time needed to complete a full machine cycle. Since SRMs are known for their robust fault tolerance, this delay in detection can generally be accommodated. The method introduced employs an extra diagnostic setup, which introduces an additional expense to the system. However, for safety-critical applications like EV and aerospace, the relative cost of the components concerning SRM and its converter is hardly significant as operational amplifiers and IGBTs of low current and voltage are required. It is important to note that the proposed technique not only aids in detecting ITSC faults involving a smaller number of turns but also contributes to minimizing breakdown losses.

3.5 Conclusions

ITSCs are responsible for creating localized hotspots within the windings of electric machines. If left unchecked, these ITSCs can lead to catastrophic failures, as they have the potential to propagate and eventually cause complete insulation breakdown. This chapter proposes an online diagnostic approach designed to trigger a fault alert whenever motor behaviour deviates due to ITSCs. In this method, a high-frequency signal is injected into the non-torque producing phase of the switched reluctance motor SRM to detect changes in inductance caused by ITSCs. The advantage is its independence from the specific control strategies employed to run the motor, as it utilizes inactive phases for injection. Experimental outcomes demonstrate that the proposed method is extremely sensitive, even to minor ITSCs. These minor faults are challenging to identify as their impact is not very apparent in the motor performance. Detecting them can significantly mitigate industrial downtime by preventing substantial winding failures in the machine. Moreover, this method identifies the faulty phase and roughly estimates the number of shorted turns by monitoring the peak values of high-frequency signals. The issue of detection reliability has also been tackled, accounting for both load fluctuations and variations in speed. This diagnostic method is applicable for identifying ITSCs in switched reluctance machines with 3 or more phases, whether used as motors or generators. Additionally, it can potentially diagnose other faults, such as eccentricity/hybrid fault conditions of ITSCs and eccentricity in switched reluctance machines, suggesting future avenues for research in this field.

Chapter 4

Diagnosis Technique for ITSCs in SRMs for Entire Speed Range with Lower Complexity

4.1 Introduction

The present chapter introduces a novel diagnosis method for ITSCs in SRMs for the entire speed range using signal injection, eliminating the complexity of the technique discussed in the previous chapter. The additional circuitries used for diagnosis purpose discussed in the previous chapter has been eliminated, and a new method has been devised. The crux of the technique with some of its key advantages are as follows:

1) In the context of this study, the switches controlling the motor phases are deliberately operated at high frequency. It occurs specifically within low torque operational regions around their respective unaligned rotor positions. This operation occurs over a consistent injection width within an electrical cycle. The outcome of this process is a series of current pulses, each attaining uniform magnitude over a specific fraction of the injection width. These pulsed currents are juxtaposed against a predefined threshold value to ascertain potential short circuits within the motor phase windings. This comparative analysis serves as the basis for short-circuit identification. A specific control scheme does not bind the proposed technique. It can be adapted for application SRMs under various control methodologies covering the entire speed range. As elaborated in subsequent sections of this chapter, minor adjustments to the injection period accommodate this versatility. One notable advantage of this method is its minimal computational load. The decision-making process relies solely on straightforward comparisons. Notably, the diagnostic procedure does not require supplementary hardware components, reducing the complexity.

2) The method proposed in this study exhibits higher sensitivity, enabling the identification of ITSCs involving as few as four turns (equivalent to approximately 4% of the total turns within a phase). This method also possesses the capability to determine the specific phase affected by the fault and to provide an estimate of the number of short-circuited turns. Under higher loads, the impact of saturation becomes

apparent in SRMs, leading to a sudden dip in the inductance of the torque-producing phase. Due to the sequencing of the injection process before the phases engage in torque generation, the influence of unsaturated inductance predominantly determined by rotor position only becomes significant during the injection width. Consequently, the technique remains unaffected by saturation effects at higher loads. This characteristic ensures that the fault indicator remains impervious to variations in load conditions. Furthermore, it is noteworthy that fluctuations in the motor speed do not affect the fault indicator.

Figure 4.1(a) illustrates an AHB converter driving an 8/6 SRM. The prevailing control strategies for SRMs encompass CCC and APC. CCC is the preferred approach in situations characterized by low to moderate speeds. Conversely, the control strategy automatically transitions to APC due to the technical challenges of effectively employing chopping techniques at higher speeds due to strong back emf. The current flow patterns during the excitation and freewheeling periods within the context of the asymmetric configuration are depicted in Figure 4.1(b). Figure 4.2(a) showcases the incremental inductance profile around the rotor position for a specific phase within an 8/6 SRM. This profile has been derived from FEM simulations conducted at varying current levels. Notably, the influence of saturation becomes evident at current levels exceeding 8A. Segment II of the profile is the positive torque region, while negative torque is obtained in segment IV. The portion of segments I and III is a low torque region as the rate of change in inductance is very small, as depicted. ITSC in pole *A'* of phase *A* with currents in different winding parts following the fault is also depicted in Fig. 4.2(a). It showcases how the uniformity and symmetry of the flux distribution are perturbed in the presence of a winding fault. Moreover, the presence of winding shorts decreases both the self-inductance and resistance within the

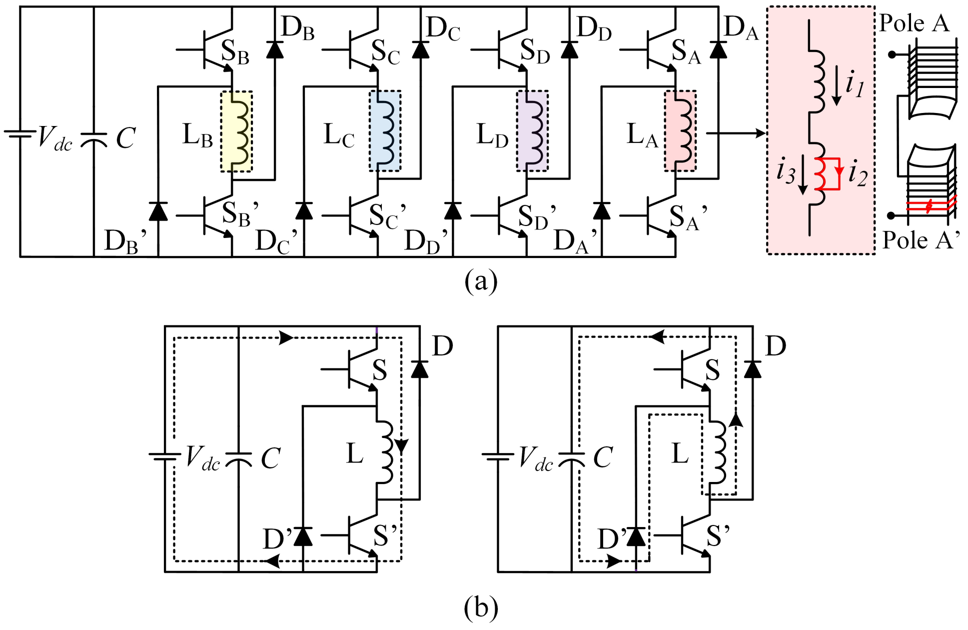

(a)

(b)

Figure 4.1: Basic configuration of 8/6 SRM driven by an asymmetric half-bridge converter.

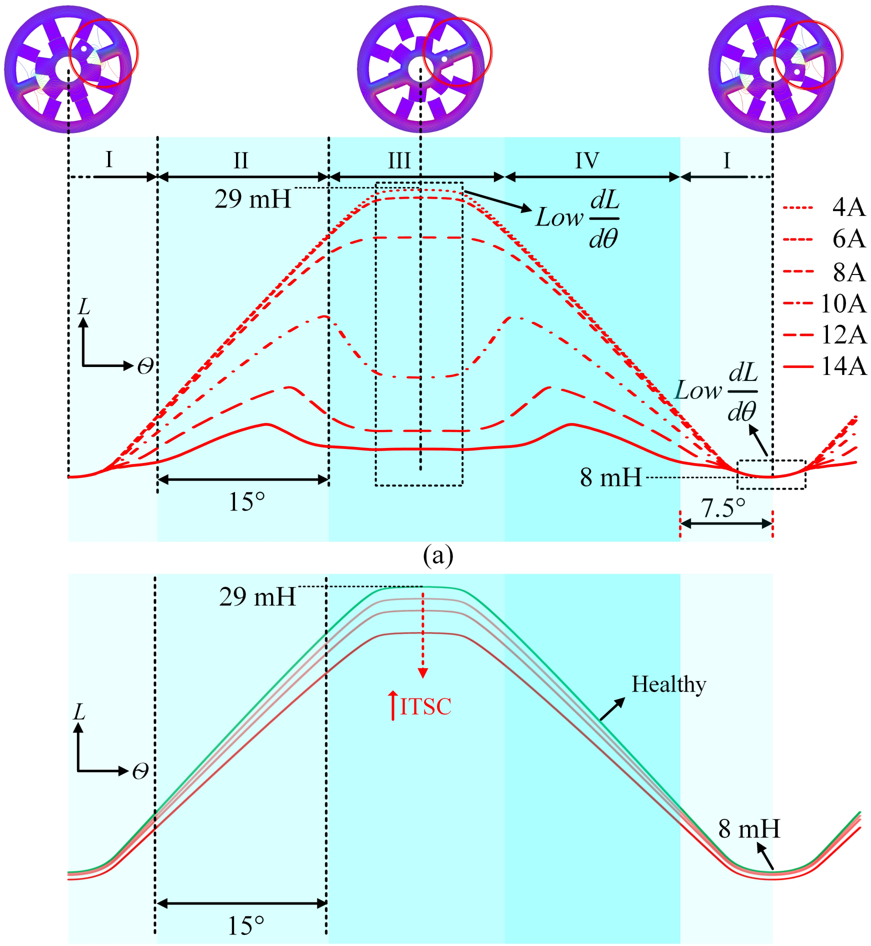

(a)

(b)

Figure 4.2: Inductance profile of the test motor (a) Incremental inductance illustrating saturation effect obtained in FEM (b) Effect of ITSC with increasing severity on the unsaturated inductance profile.

faulty phase. The impact of ITSC on the inductance profile, as the number of shorted turns increases, is portrayed in Figure 4.2(b). The unsaturated inductance profile is exclusively presented for the faulty scenario, as the diagnostic methodology is nowhere linked to saturation effects, as elaborated upon subsequently. The graph clearly illustrates that the inductance diminishes with the growing severity of ITSC, a relationship directly linked to the square of the number of turns. Additionally, the mutual inductance between the unaffected and shorted turns contributes to the reduction in effective inductance. The effect of ITSCs on the performance of SRM considering both the control schemes have already been discussed and can be referred from Chapters 2 & 3.

4.2 Propositions of the Diagnosis Technique

4.2.1 Theoretical Background of the Proposed Scheme

During the operational phase of motoring in an SRM, the phase exhibiting a positive slope in its inductance profile is energized to harness positive torque. This favorable

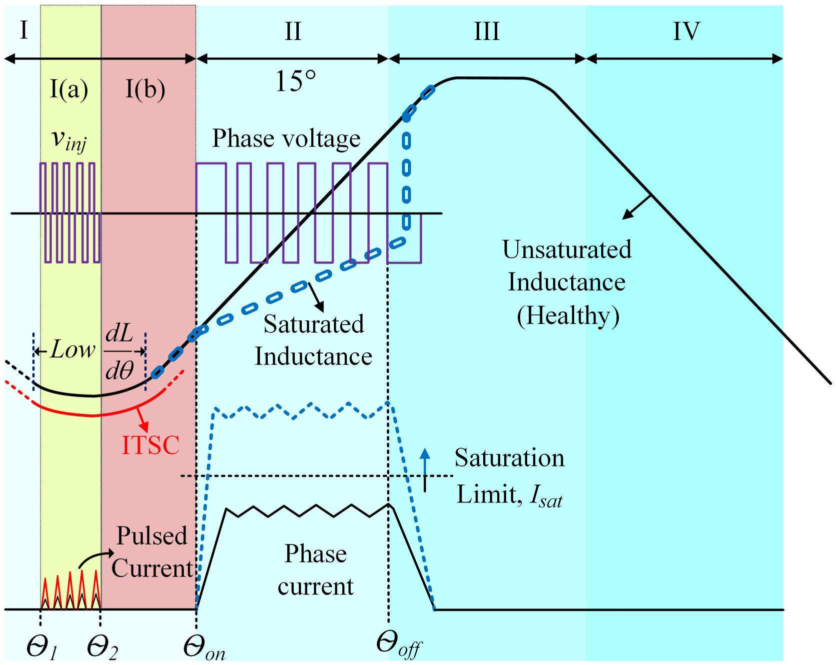

Figure 4.3: Principle of diagnosing ITSC.

region, labeled Segment II of the inductance profile and characterized by a positive slope, is effectively employed for this torque generation, as depicted in Figure 4.3. Furthermore, an alternative strategy involves activating the phase within region I(b) of Segment I. This approach enhances the motor torque by creating overlapping phase currents, as illustrated in Figure 4.4. It contributes to an increased torque output from the motor.

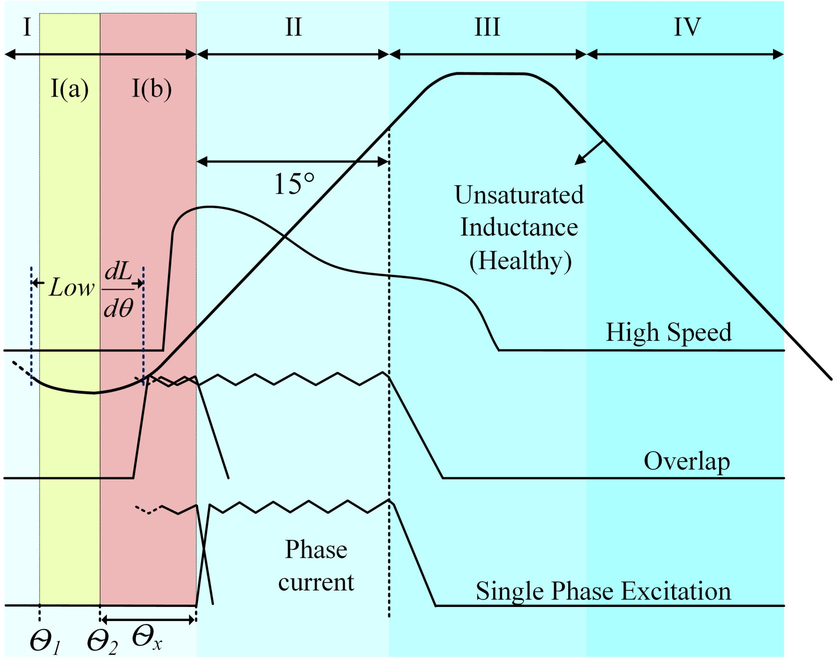

Figure 4.4: Phase current of SRM in single phase excitation, overlap condition and high speed operation.

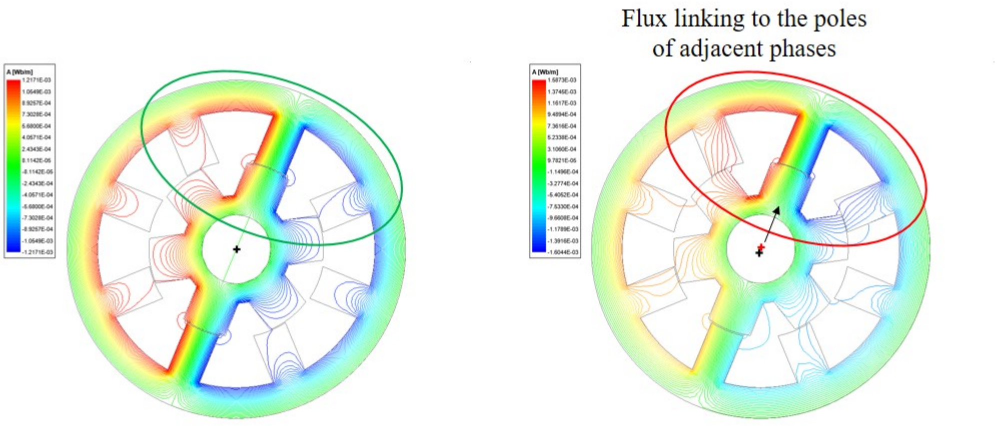

(a) Aligned Position (Healthy)

(b) Aligned Position (Eccentric)

✚ Original centre ✚ Shifted centre

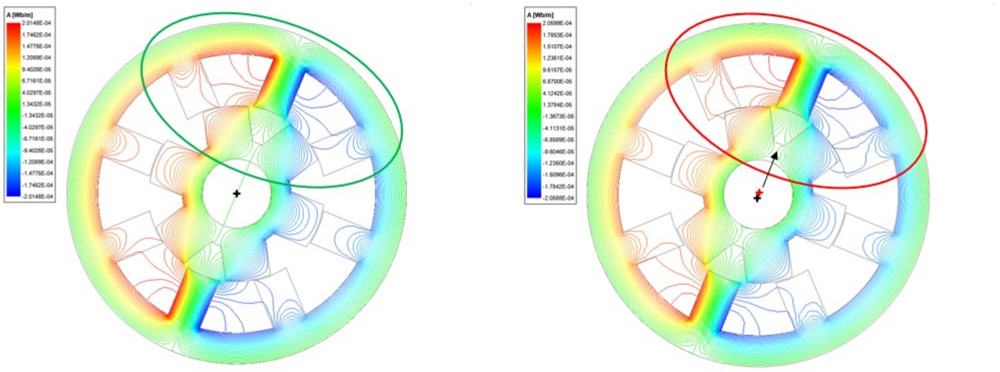

(c) Unaligned Position (Healthy)

(d) Unaligned Position (Eccentric)

Figure 4.5: Healthy and eccentric rotor (static eccentricity of 40%) at aligned and unaligned rotor positions.

The phase switches are operated at a fixed high frequency in the low torque region I(a) of segment I for a fixed injection width (θ_1 - θ_2) to inject pulse current before the particular phase is activated for torque production. This procedure is visually represented within the highlighted yellow zone in Figure 4.3. The described process is systematically repeated for each phase. During this repetition, pulse currents are injected into their respective phases within their corresponding low torque regions around unaligned rotor positions. These pulse currents are exclusively influenced by the inductance, which solely depends on the rotor position within the specified injection width. This particular injection of pulse currents helps diagnose ITSCs within the SRM. Notably, the magnitude of the pulse current escalates with the reduction in inductance attributed to short circuits occurring in the phase windings. This phenomenon is depicted in Figure 4.3. Between the two available low torque regions, preference is given to region I(a) within segment I for injection, as opposed to the low torque region in segment III. For single-phase excitation or phase overlap conditions, segment III can also be used for injection if the phase current decays to zero well before the low torque region. However, at higher speeds, phase currents persist

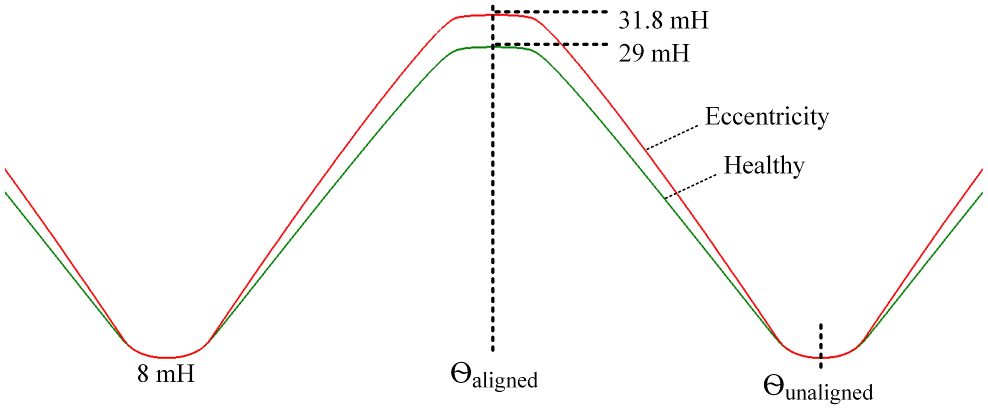

Figure 4.6: Inductance profiles for healthy and eccentric rotor (static eccentricity of 40%).

well into the major portion of segment III, as illustrated in Figure 4.4. This prolonged presence of phase currents in segment III constrains the feasibility of operating phases at a higher frequency within this segment. Moreover, selecting the preferred injection region does not compromise the inherent flexibility of phase overlapping. Any phase can be activated between the positions marked as θ_x to enhance torque output.

Opting for this specific injection region also confers immunity to potential complications such as manufacturing defects and eccentricity. These issues lead to the inductance variation in SRM. However, the effect on inductance is opposite to that caused by ITSC. It increases due to the change in the air gap in the motor, except for the unaligned rotor positions. In the case of rotor eccentricity, air gap reluctance is not equal for both poles of the energized suffering phase. In such inequality, other flux paths appear through the unenergized adjacent stator poles. Therefore, the pole of the energized phase adjoining the shortened air gap has greater flux linkage than the other pole of the same phase. Due to the additional flux paths, the overall reluctance reduces, leading to an increase in the inductance. However, this is not true for all the rotor positions. Figure 4.5 shows the flux lines for healthy and eccentric rotor conditions at aligned and unaligned rotor positions. A constant current of 1 A energizes the phase along which the rotor poles are aligned. It can be inferred that under eccentricity at an aligned rotor position, the flux linking the poles of adjacent phases increases compared to a healthy condition. It implies a reduction in reluctance, leading to an increase in inductance. The flux linking to the adjacent poles is almost similar at the unaligned rotor position shown in Fig. 4.5 (c) and (d). Therefore, with the same reluctance path, no changes would be observed in the inductance around the unaligned rotor positions. The inductance profile of the most suffered phase obtained in the FEM simulations for healthy and eccentric rotor conditions is shown in Fig. 4.6.

The proposed method has been implemented for control schemes featuring fixed turn-on and turn-off angles. A specific region has intentionally been set aside for injection to facilitate the diagnostic process. This separation ensures that the diagnostic pulse currents remain independent from the phase currents. However, certain control techniques involve the real-time evaluation and adjustment of turn-on and turn-off angles throughout the motor operation. In such cases, the turn-on angle can vary and may fall before or after the unaligned rotor position. Consequently, the diagnostic approach cannot be effectively separated from the current profiling, reducing diagnostic efficacy. Nevertheless, the viability of the proposed method can be preserved by designating a segment within the negative torque region for injection, depicted in Figure 4.7. This approach guarantees the feasibility of the diagnosis method even when dealing with control strategies that dynamically update the turn-on and turn-off angles during operation.

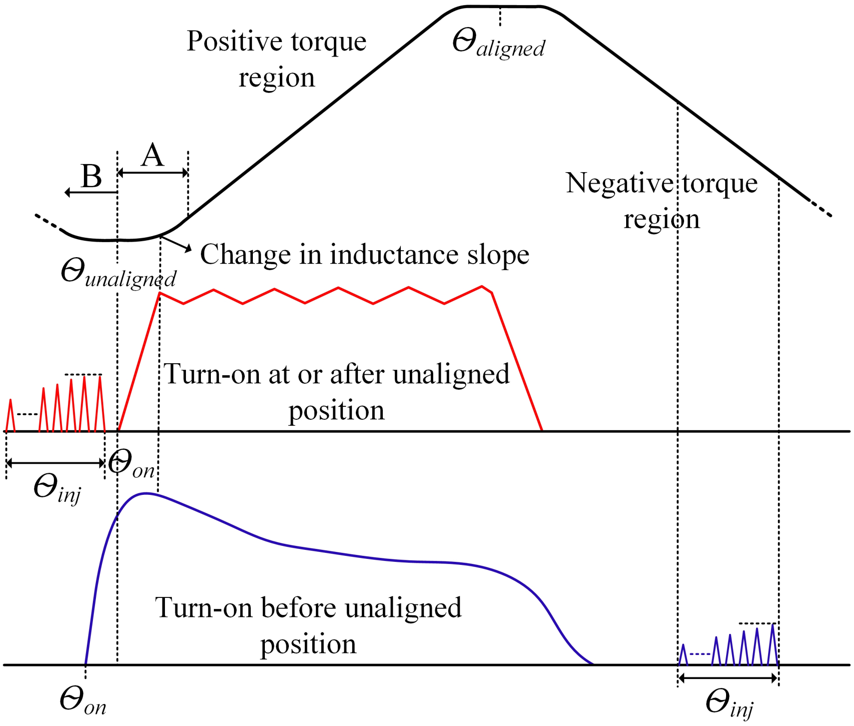

Figure 4.7: Turn on at and before the unaligned position with the feasibility of injection.

4.2.2 Injection Methodology and Frequency Selection

The upper and lower switches within the same phase leg are synchronized to be turned on and off simultaneously. This coordinated action introduces fixed high-frequency voltage pulses strategically around unaligned rotor positions, as depicted in Figure 4.8(a). The resulting pulse currents exhibit distinct peaks corresponding to the impedance profile within the designated injection width, predominantly reflecting the unsaturated inductance value. To prevent continuous current flow within the injection width and ensure that the current diminishes to zero before the commencement of the subsequent cycle, a duty ratio (D) lower than 0.5 is adopted for the high-frequency voltage pulse. This configuration, along with a higher frequency selection, contributes to diminishing the amplitude of the pulse currents. This adjustment not only prevents motor saturation but also mitigates incurred losses. Also, it can be observed that a specific portion (θ_{f1} - θ_2) within the overall width (θ_1-θ_2) presents a uniform inductance profile. Therefore, the peak value of the different pulses within this fraction would acquire the same magnitude

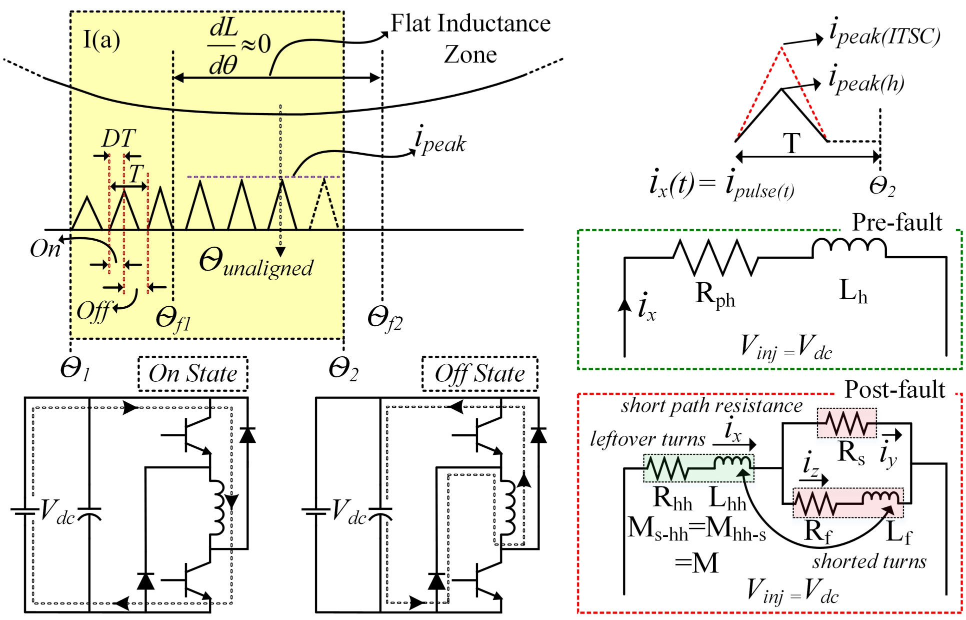

(a) (b)

Figure 4.8: (a) Flat inductance profile (θ_{f1}-θ_2) within the injection width (θ_1-θ_2) (b) Pre and post-fault winding equivalent circuit considering injection.

as shown in Fig. 4.8(a). As the phase inductance between θ_{f1} and θ_{f2} is assumed to be constant and neglecting the small phase resistance R_{ph}, the peak value $i_{peak(h)}$ of the pulse current in the healthy condition can be related to inductance $L_h(\theta_{f1}$-$\theta_2)$ as

$$i_{peak(h)} \approx \frac{V_{inj}}{L_h(\theta_{f1}-\theta_2)\times f_{inj}}D, \tag{4.1}$$

where V_{inj} and f_{inj} are the magnitude of the injected voltage and frequency respectively. At higher frequencies, the influence of inductive reactance would be dominant compared to the phase resistance. Therefore, the phase resistance is neglected in the formulation as it has a negligible effect on the impedance observed during the injection width.

Figure 4.8 illustrates the equivalent winding circuit before and after a fault occurrence, considering the injected current. Let N_{ph} denote the total number of turns in an intact winding, and δN_{ph} represent the total number of shorted turns. In normal operating conditions, the relationship $L_h(\theta_{f1}$-$\theta_2)$= $L_h(\theta_2)$= $N_{ph}^2/\mathcal{R}$ is valid, where $\mathcal{R}$ signifies the reluctance of the system. During ITSC incident, the inductance values of the remaining intact turns (L_{hh}), the shorted turns (L_f), and the mutual inductance (M) existing between the remaining intact turns and the shorted turns can be reasonably approximated as follows:

$$L_{hh}(\theta_2)=\frac{(N_{ph}-\delta N_{ph})^2}{\mathcal{R}}=(1-\delta^2)L_h(\theta_2), \tag{4.2}$$

$$L_f(\theta_2) = \frac{(\delta N_{ph})^2}{\mathcal{R}} = \delta^2 L_h(\theta_2), \tag{4.3}$$

$$M(\theta_2) = \delta(1-\delta)L_h(\theta_2). \tag{4.4}$$

The effective inductance of the faulty phase (L_{eff}) under ITSC can be approximated as:

$$\begin{aligned} L_{eff}(\theta_2) &= L_{hh}(\theta_2) - M(\theta_2) \\ &= (1-\delta^2)L_h(\theta_2) - \delta(1-\delta)L_h(\theta_2). \end{aligned} \tag{4.5}$$

As the inductance of the faulty phase decreases, there is an observable increase in the peak of the high-frequency pulsed current ($i_{peak(ITSC)}$), as illustrated in Figure 4.8. It is compared to a predetermined threshold value, which serves as a diagnostic criterion for identifying ITSCs. The threshold value is established through empirical analysis, considering the percentage change in the peak values of high-frequency current during both healthy operating conditions and scenarios involving a 4% ITSC, as observed in FEM simulations.

The variation in the inductance profile near the unaligned rotor position has been previously discussed. For each phase, the injection width (θ_1-θ_2) is kept constant at 5°, with nearly half of this span falling within the zone of flat inductance. It is crucial to ensure sufficient pulses within the range of θ_{f1} and θ_2 that exhibit comparable amplitude. This adequacy of pulses is vital for precise comparison with the predefined threshold value. For this purpose, the frequency is chosen so that an adequate number of pulses are present within the flat inductance zone, which applies to the entire speed range. Having a minimum of 7-8 pulses within the injection width guarantees the availability of 3-4 pulses within the flat inductance region, enabling the convenient identification of ITSC. The injection frequency required to achieve the minimum necessary pulse count (N_p) can be correlated with the rated speed (N_{rated}) in rpm, and this relationship is expressed as:

$$f_{inj} \approx \frac{N_p \times N_{rated} \times \theta_{ec}}{(\theta_1 - \theta_2) \times 10}, \tag{4.6}$$

where θ_{ec} is one electrical cycle in degrees.

Considering a rated speed of 1200 rpm and having 7 pulses within θ_1-θ_2 of 5°, the injection frequency is calculated as 10 kHz using equation (4.6). The number of pulses within this zone exhibits an inverse relationship with the speed, remaining higher at lower speeds, as depicted in Figure 4.9. It is worth noting that the frequency of injection can be increased up to the limit governed by the capabilities of the semiconductor switches in the motor-driving converter. Moreover, the pulse currents contribute to related losses, which can be managed by selecting an appropriate injection frequency. The torque and losses due to injection are discussed in the subsequent section.

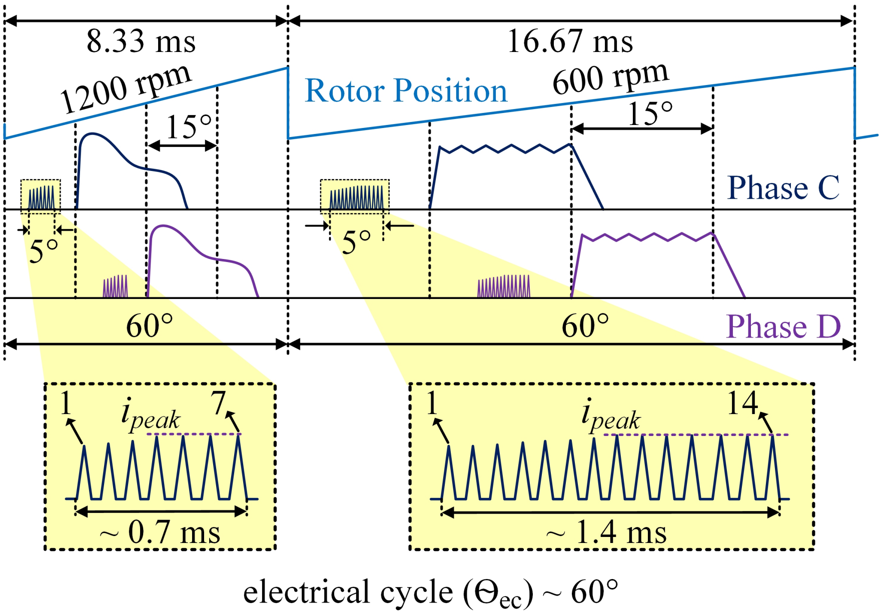

Figure 4.9: Variation in number of pulses due to change in speed.

4.3 Experimental Validation & Results

4.3.1 Experimental Setup

The functional block diagram, incorporating control and diagnosis, is illustrated in Figure 4.10. The proposed technique is validated for the entire speed range, employing CCC up to medium speed and APC for higher speed. The motor speed, which serves as feedback to the controller, is integrated to determine the rotor position, a crucial factor for both control and fault detection. The controller dictates the ON and OFF positions (θ_{on} and θ_{off}) to excite the phases sequentially to operate the motor. Each phase is activated for 15° in single-phase excitation mode. The respective phases are switched around their unaligned positions at a frequency of 10 kHz for a duration of 5° to introduce pulse currents, as previously detailed. For instance, in Figure 4.10, high-frequency pulses are injected into phase A between 34° and 39°. The injection strategy adheres to the flat inductance zone concept explained earlier, with the resulting pulse currents for diagnostic purposes represented for better comprehension. Fault flags corresponding to each phase are determined based on the rotor position and phase currents, with the underlying logic in the accompanying flowchart. The magnitude of pulse currents in phase A, surpassing a predefined threshold value i_t as set in the controller, triggers the fault flag, as demonstrated. Fault flags serve a dual purpose: detecting the occurrence of ITSCs and pinpointing the faulty phase within the motor. The efficacy of the proposed method is verified experimentally under diverse loading conditions and speed variations. Moreover, the robustness is substantiated through transient studies that account for the motor dynamic behavior under varying load and speed conditions.

A specialized test setup has been developed to emulate various levels of ITSCs,

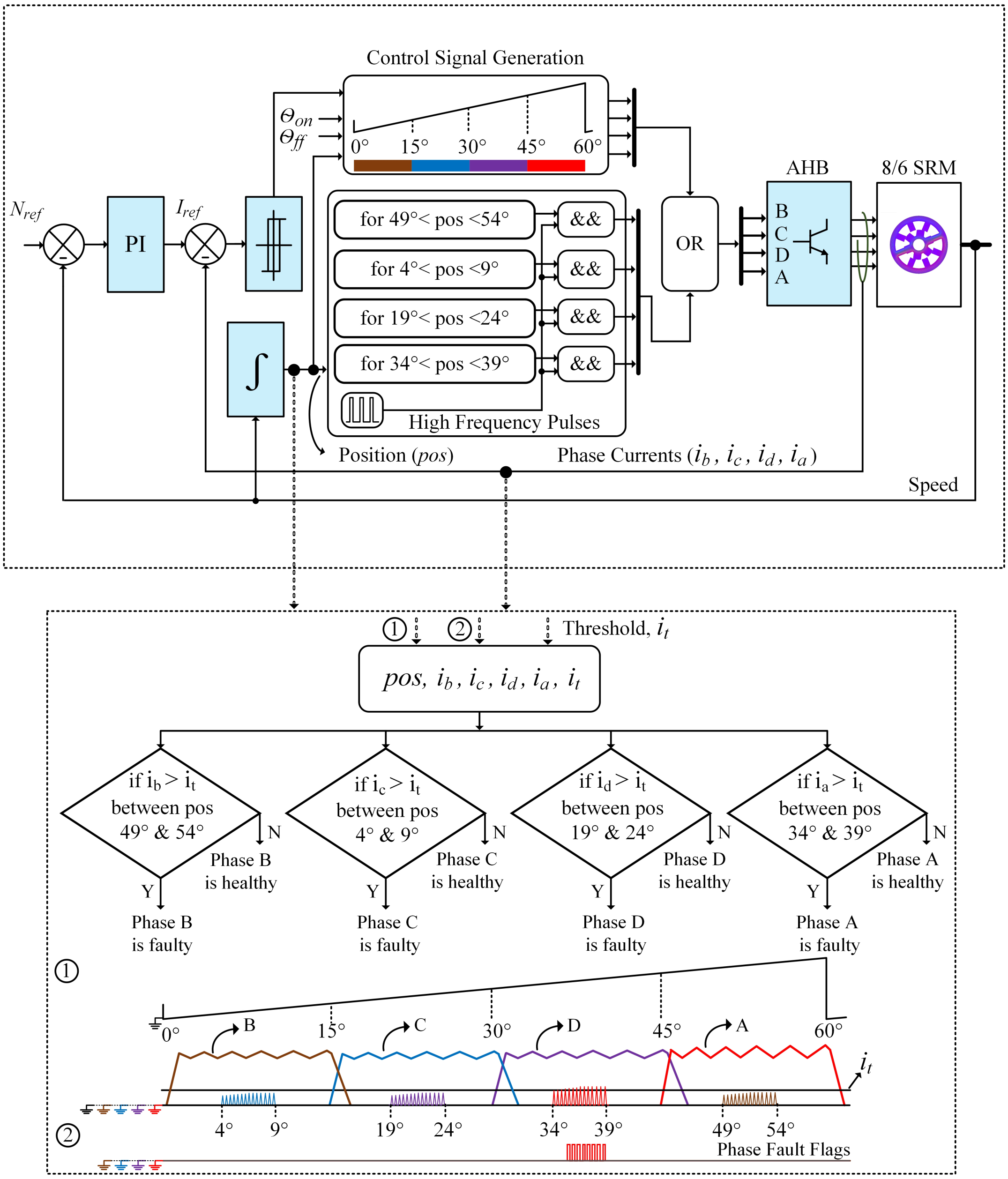

Figure 4.10: Block diagram depicting control and fault diagnosis logic.

consisting of a custom 1 hp, 72 V, 8/6 SRM equipped with assorted winding taps in two phases. The same is depicted in Figure 4.11. Each phase comprises 108 turns, with 54 turns wound around a single pole. The operation of the SRM is managed through a Semikron IGBT module SKM100GB12T4-based AHB converter. For the execution of control and diagnosis logic, the currents flowing through all four motor phases are detected using hall-effect sensors, specifically LA-55 sensors. These sensed currents are then fed back into the analog-to-digital converter channels of the controller. A 1000 pulse-per-revolution incremental encoder coordinated with an absolute encoder determines the speed and rotor position. The control and diagnosis logic is implemented in a digital signal processor TMS320F28379d at a sampling rate of 1e-05 seconds. Notably, the proposed diagnostic approach is rigorously assessed using the fundamental drive structure of the SRM without

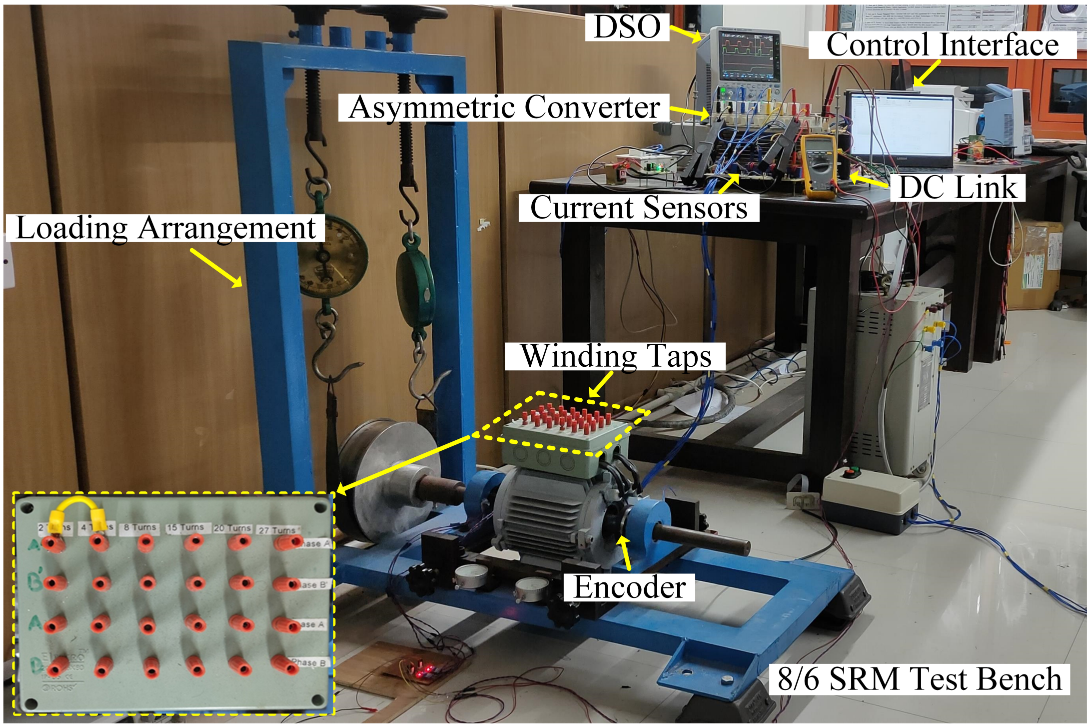

Figure 4.11: Experimental setup.

necessitating any supplementary hardware components.

A comprehensive analysis of the experimental outcomes obtained under CCC and APC is presented. SRM is energized using a DC link voltage of 72 V, and an injection frequency of 10 kHz is employed for the entirety of the experimental validation. Pertinent parameters such as the applied load torque and the operational speed are explicitly cited wherever necessary to facilitate thorough explanations.

4.3.2 Diagnosis of ITSC in CCC mode

At a speed reference (N_{ref}) of 380 rpm, the SRM is operated with a light load torque (T_{load}) of 0.4 Nm. In this situation, the motor draws a current of 4 A per phase, effectively fulfilling the torque requirement illustrated in Figure 4.12. As shown, two-phase currents (A & D) and rotor position are monitored for the healthy condition. For a closer examination, a single electrical cycle spanning 60° is presented, with an excitation duration per phase of 15° and an injection duration of 5°, depicted within the enlarged window labeled as zoom window-1. This detailed view reveals that both phase currents exhibit identical peak values ($i_{peak(h)}$) of 0.34 A. This characteristic is explicitly demonstrated for phase A in the focused view labeled as zoom window-2 within Figure 4.12. As elaborated earlier, the predetermined threshold value (i_t) essential for the diagnosis methodology is set to 1.4 times the peak value observed during normal winding conditions. This selection considers a safety factor to ensure the fault flags are not erroneously triggered during healthy operations.

Figure 4.13 presents the scenario of an ITSC in which approximately 4% of a phase

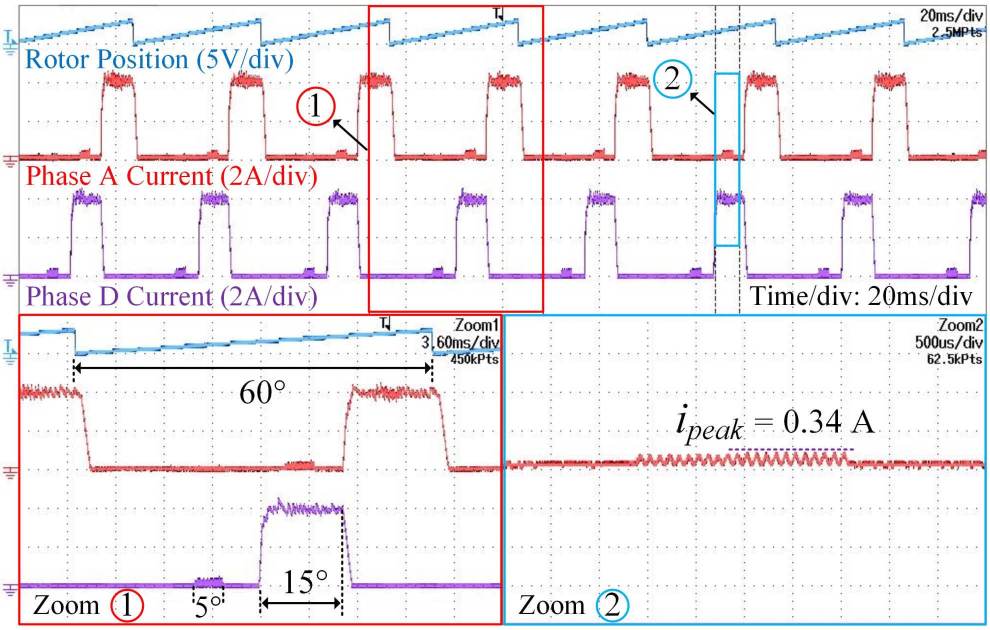

Figure 4.12: Healthy operation of SRM depicting rotor position, phase A & D currents with high frequency pulse currents in CCC mode.

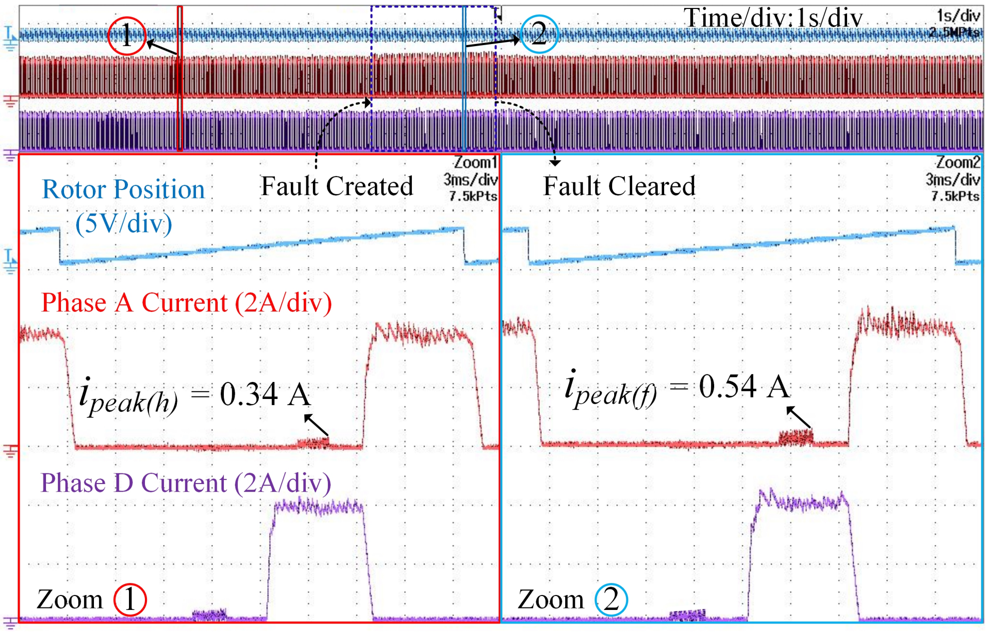

Figure 4.13: Healthy and faulty operation depicting the variation in peak value of high frequency pulse current in the faulty phase A.

winding, specifically in phase A, experiences a short-circuit, amounting to four turns over one of the poles. The blue dashed region denotes the duration the SRM undergoes the ITSC event. Under the conditions of ITSC during closed-loop operations, the reference current is elevated to meet the load requirements. Consequently, both the healthy and faulty phase currents experience an increase in magnitude. However, this increase in phase currents remains relatively moderate for minor short circuits. This effect is demonstrated in the zoomed-in windows labeled as zoom window-2 and zoom window-1 within Figure

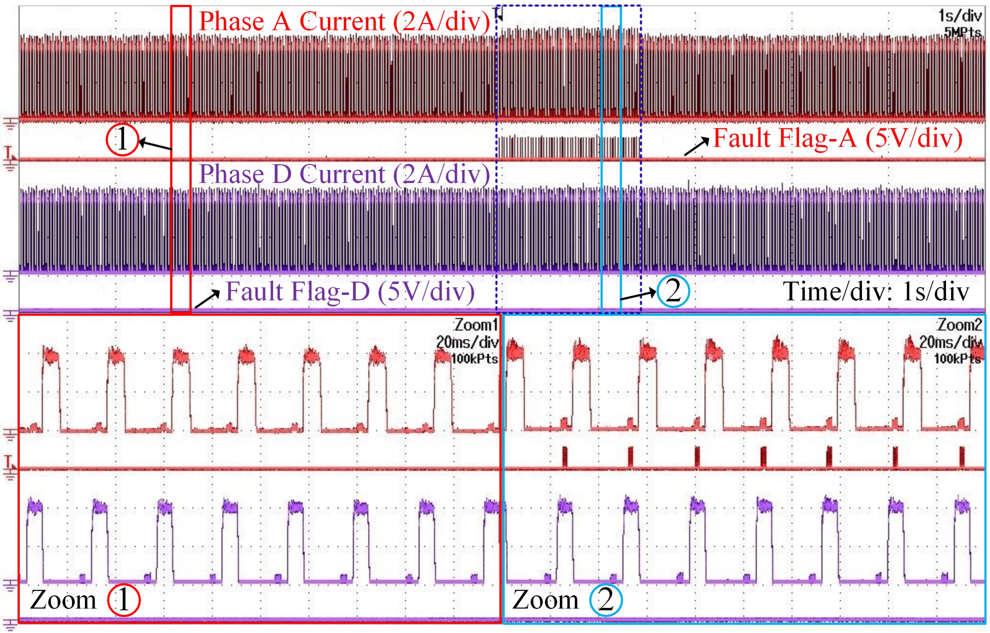

Figure 4.14: Phase currents and fault flags for two phases (A & D) under healthy and faulty (ITSC of 4 turns over a pole) conditions.

4.13, illustrating the slight uptick in phase A and D currents, respectively, during ITSC compared to healthy operating conditions. With current being directly regulated in CCC, the impact of ITSC on the faulty phase current is subtly discernible when control precision is high. During the chopping period, the current overshoots the hysteresis band due to fluctuations in inductance, exemplified by the behavior of phase A current. The peak value ($i_{peak(f)}$) of the pulse current in the faulty phase A experiences an increase, rising significantly to 0.54 A from its value under healthy winding conditions. As the number of short-circuited turns intensify, leading to reduced inductance, this peak value experiences further augmentation, as indicated in Figure reference to Figure 4.2(b). For instance, for an ITSC involving 15 turns over a pole, this value rises to around 0.6 A. This escalation in peak value helps gauge the severity of ITSC in SRMs. Conversely, no discernible alteration is noted in the peak value of the pulse current within the adjacent healthy phase D. Even for minor short-circuits, the change in peak value is significant, which helps easy diagnosis of ITSC. This characteristic highlights the increased sensitivity of the proposed method towards detecting minor ITSC events.

The diagnosis of ITSC and the subsequent identification of the faulty phase involve comparing the peak current values and a predetermined threshold value established within the DSP. Moreover, fault flags are formulated for each phase, adhering to the logic delineated in Figure 4.10. Figure 4.14 presents the phase currents of two adjacent phases (A and D) alongside their respective fault flags. Due to the channel limitations of the oscilloscope, the phase currents and flags are showcased only for these two specific phases. The observations made within this demonstration apply to other phases as well. As the fault is instigated by shorting four turns in phase A, the corresponding fault flag for this particular phase transitions to a high state (3.3 V). Conversely, the flag associated with the adjacent phase *D* remains in a low state (0 V) throughout, affirming the presence of a healthy winding condition. The impact of the fault on one phase does not dominantly influence the others. It is worth noting that the fault flag for the problematic phase subsequently reverts to a low state once the fault is rectified. The conditions before and after the fault are visually presented in the zoomed-in windows labeled as zoom window-1 and zoom window-2 within Figure 4.14 to facilitate a clear understanding. The motor is subjected to an elevated load torque of 2 Nm while maintaining the reference speed at 380 rpm To assess the effectiveness of the proposed technique across diverse loading conditions. This variation in load aims to validate the robustness of the method under different operating conditions. As the motor is subjected to this intensified load, it draws an approximate current of 8 A, as shown in Figure 4.15. A fault of the same magnitude is intentionally created in phase *A*. As a result of this fault occurrence, the corresponding fault flag experiences a transition to a high state, as depicted within the enlarged zoom window-1.

4.3.3 Immunity of Fault Indicator under Load/Speed Fluctuation

In the context of designing a fault diagnosis system, ensuring reliability is of paramount importance. The developed fault indicator must demonstrate consistent performance even in the presence of load and speed fluctuations within the motor. Its responsiveness should exclusively activate when the motor encounters actual faults.

The motor is subjected to an abrupt transition in load torque, shifting from 0.4 Nm to 3 Nm, and subsequently reverting to its initial operational state. This load variation

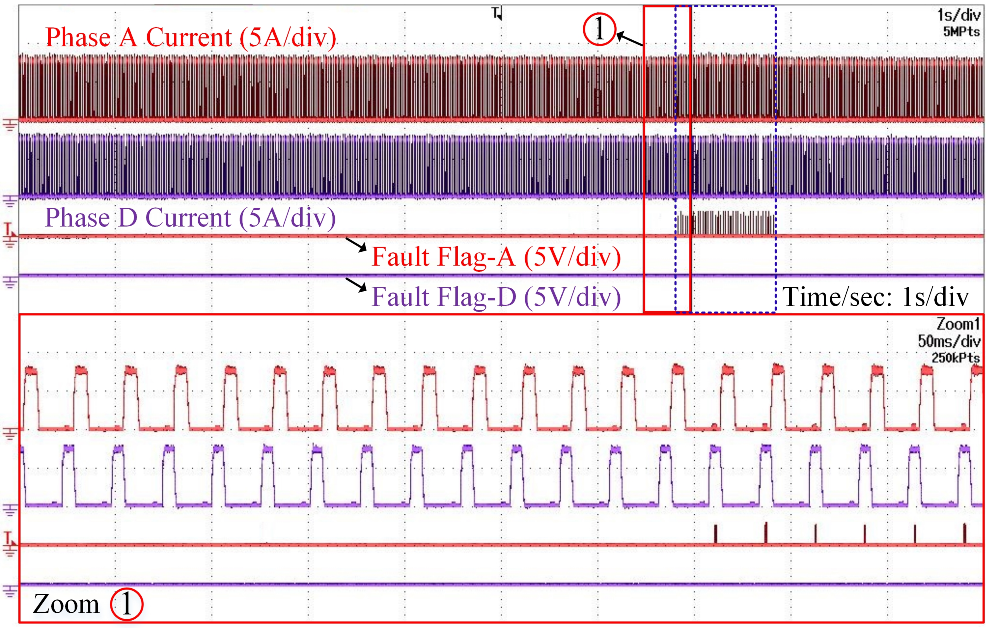

Figure 4.15: Phase currents and fault flags for two phases (*A* & *D*) under healthy and faulty conditions at a higher load torque of 2 Nm.

prompts an instantaneous shift in current from 4 A to 10 A, which then returns to 4 A according to the torque demand. Remarkably, throughout this dynamic operational cycle, the fault indicator or the peak of the pulse currents in each phase remain constant, as depicted in Figure 4.16. This persistence in indicator values compels the associated fault flags to remain at a low state, thereby signifying fault-free performance. The peak value remains the same as the injection voltage experiences the same unsaturated inductance within the injection width. Consequently, the fault indicator effectively remains decoupled from variations in load torque applied to the motor.

Under closed-loop control, the motor speed experiences fluctuations in response to varying loads, as illustrated in Figure 4.17. Specifically, the load torque exerted on the motor is transitioned from 2 Nm to 0.4 Nm. Notably, how the load is relieved differs from an abrupt step change; rather, it is gradually released due to the implementation of a mechanical loading arrangement, as visualized in Figure 4.11 within the test rig. This load-induced speed fluctuation is visualized in zoom window 1 and zoom window 2 within Figure 4.17, with speed varying between 238 rpm and 434 rpm. An intriguing observation is that the peak values of the pulse currents maintain a value of 0.34 A throughout this speed range. However, the number of pulses within the defined injection duration diminishes at higher speeds. With no change in the fault indicator, the fault flags remain low, representing the fault-free operation.

4.3.4 Diagnosis of ITSC amid Load and Speed Transients

The robustness of the proposed methodology during transitional stages involving fluctuations in both load and speed has been empirically validated. During a transition period where the torque demand escalates from 0.4 Nm to 3 Nm while maintaining a speed

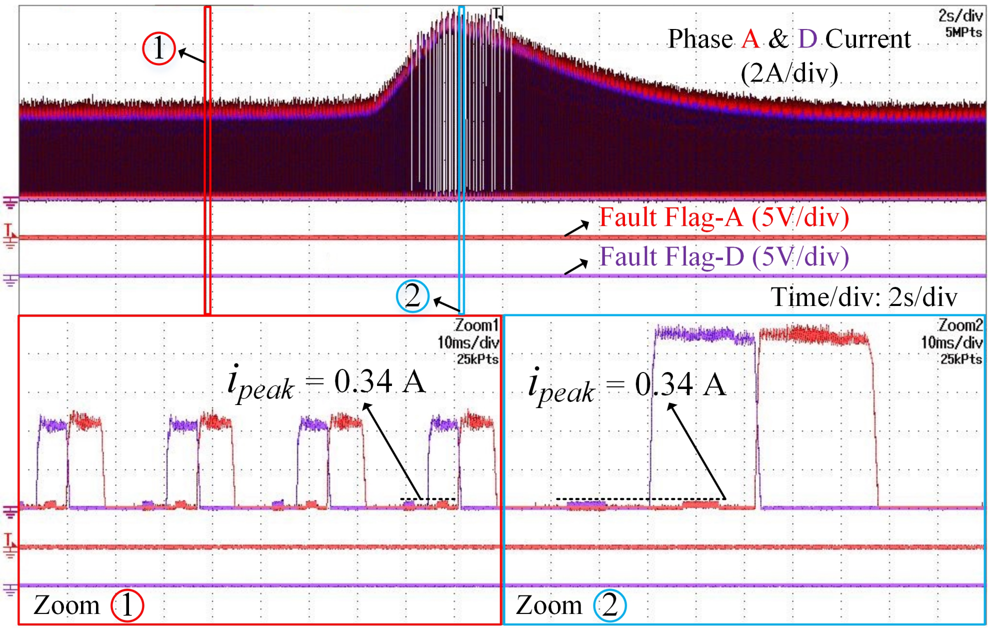

Figure 4.16: Immunity of the fault indicator under load variation from 0.4 Nm to 3 Nm.

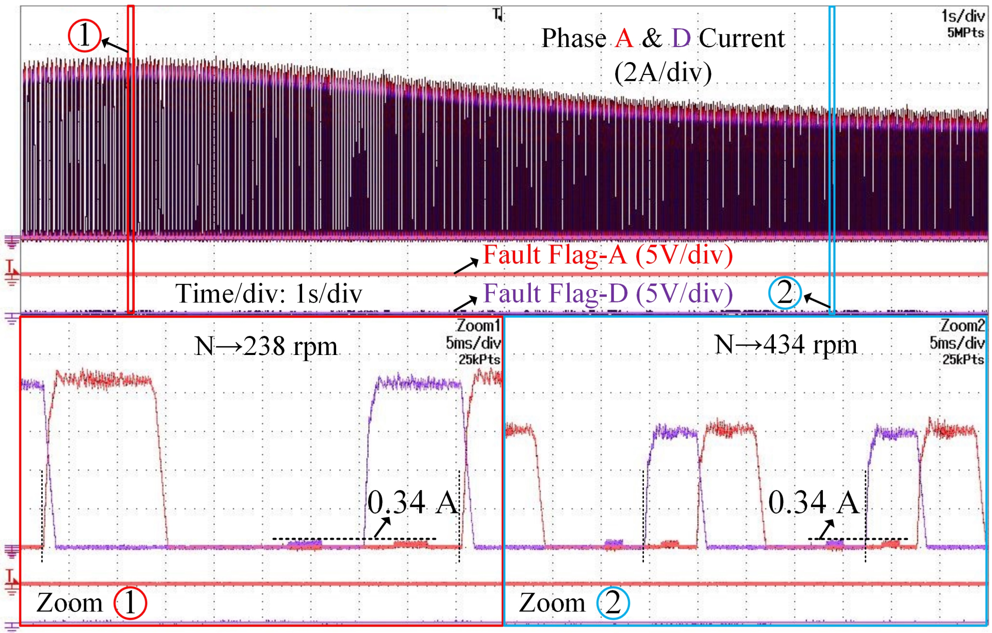

Figure 4.17: Immunity of the fault indicator under speed fluctuation due to load variation from 2 Nm to 0.4 Nm.

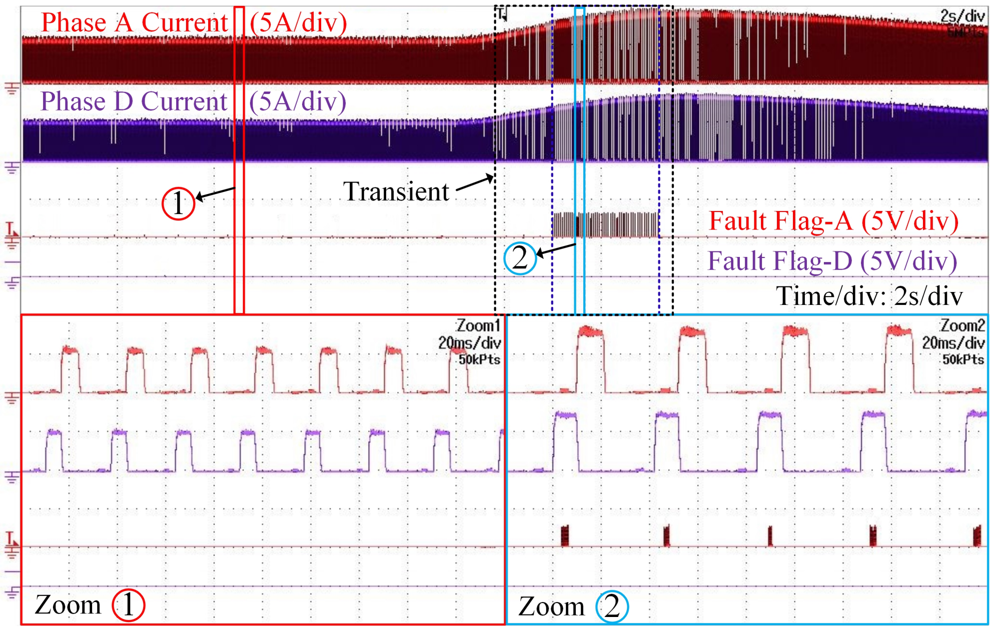

Figure 4.18: Fault diagnosis amid load transient with change in load torque from 0.4 Nm to 3 Nm at the speed reference of 380 rpm.

reference of 380 rpm, an ITSC event is deliberately introduced. Specifically, four turns within a pole of phase A are short-circuited, as portrayed in Figure 4.18. The activation of the fault flag for the corresponding faulty phase serves as a clear indicator of the occurrence of ITSC.

Furthermore, to evaluate the performance during speed transients, the reference speed varies from 300 rpm to 660 rpm while keeping the load torque constant at 0.4 Nm, as evidenced in Figure 4.19. Like before, during the transitional phase between the initial and final reference speeds, four turns within phase *A* are momentarily short-circuited. In this context, the fault flag associated with phase *A* is triggered, signalling an augmentation in the magnitude of the pulse current within this specific phase. It substantiates the effectiveness of the method in accurately diagnosing ITSCs, even under transient conditions.

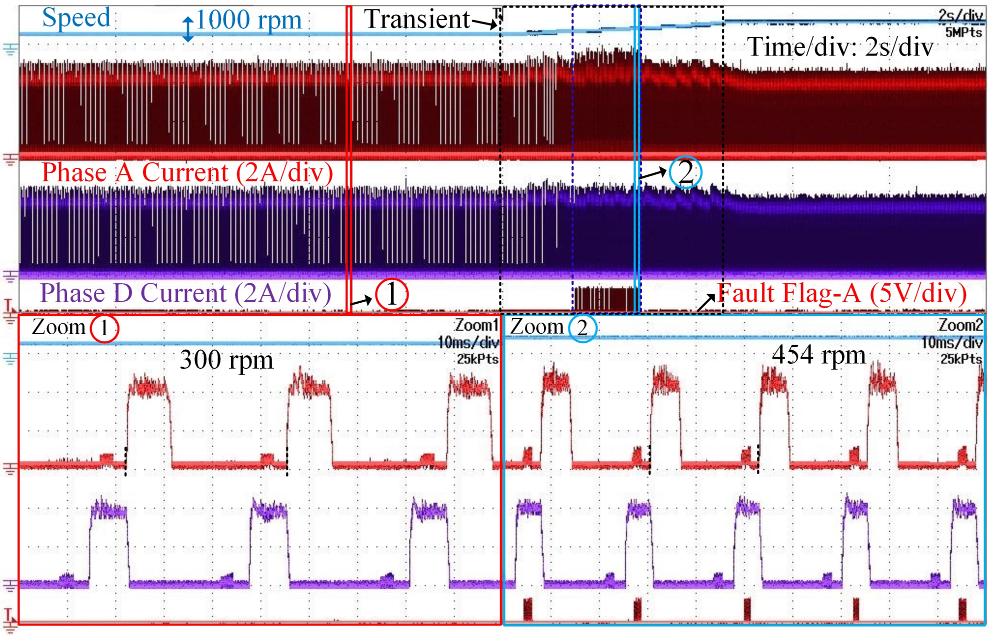

Figure 4.19: Fault diagnosis amid speed transient with change in speed from 300 rpm to 660 rpm at the load torque of 0.4 Nm.

4.3.5 Diagnosis of ITSC in APC mode

Operating the SRM at its rated speed of 1200 rpm entails applying a full DC link voltage of 72 V. Under such high-speed conditions, the conventional chopping process, which transitions the control mode from CCC to APC, is not feasible. Depicted in Figure 4.20, the APC mode of operation is showcased in both healthy and faulty scenarios. Notably, the diagnostic methodology remains consistent with the discussion presented earlier. An ITSC event involving four turns is deliberately introduced within phase *A*. The manifestation of this fault is marked by the fault flag transitioning to a high state. Additionally, a substantial shift in the magnitude of the current within the faulty phase is evident. This shift is perceptible in the detailed views provided in zoom window-1 and zoom window-2 within Figure 4.20, which effectively portray the conditions before and after the fault occurrence. Intriguingly, there is no observable fluctuation in the flag corresponding to the adjacent healthy phase *D*. This collective evidence attests to the adaptability and efficiency of the proposed method even when the motor is operated at higher speeds, irrespective of the control techniques employed.

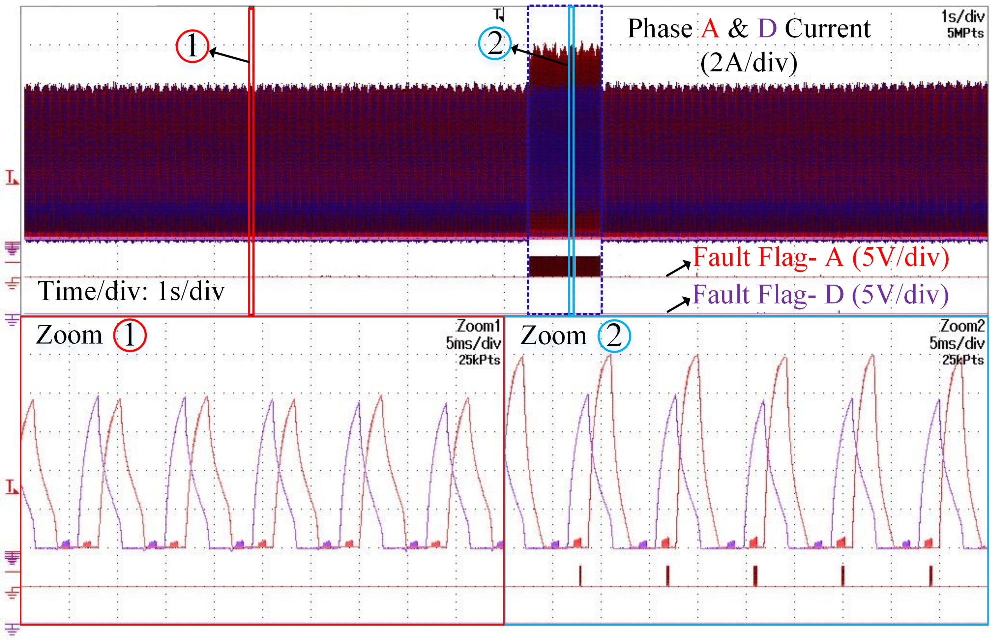

Figure 4.20: Phase currents and fault flags for two phases (A & D) under healthy and faulty (ITSC of 4 turns over a pole) conditions in APC mode.

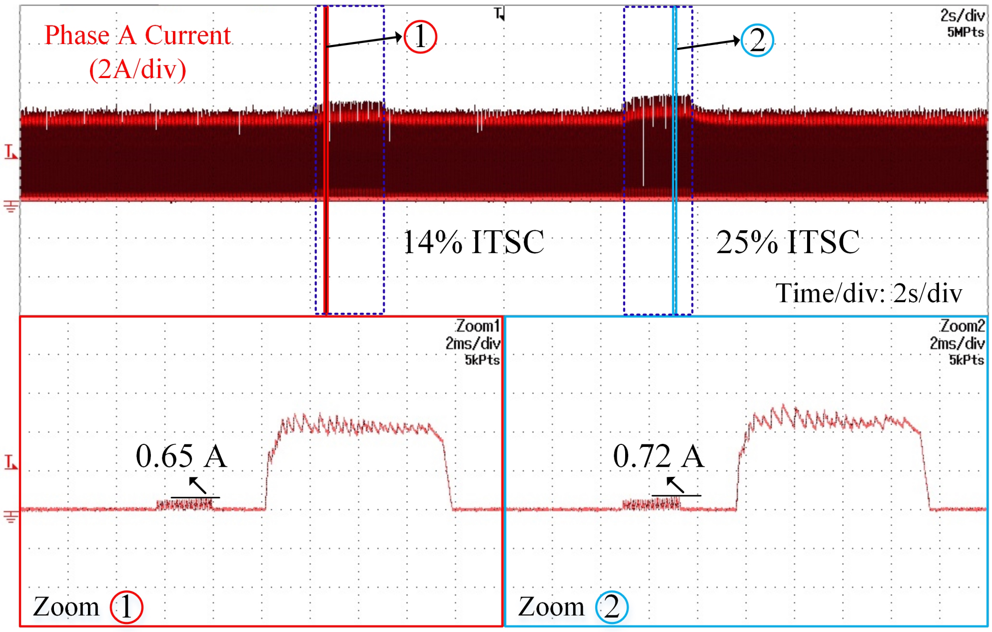

Figure 4.21: Peak values of the high frequency pulse current for 14% and 25% ITSC in phase A.

4.3.6 Fault Severity

Figure 4.21 illustrates the peak magnitudes of high-frequency pulse currents associated with 14% and 25% ITSCs within phase A. This representation serves as a means to approximate the severity of the fault occurrences. The peak value increases with the increasing number of shorted turns. For instance, the peak current attains values of 0.65 A and 0.72 A for ITSCs of 14% and 25%, respectively. Comparatively, as stated earlier, the peak current values for both a healthy winding and a 4% ITSC stood at 0.34 A and 0.54 A, respectively. This comparison of peak values affirms the capability of this diagnosis to not only detect the presence of ITSCs but also to differentiate their degrees of severity. Furthermore, for easy comprehension, the severity index (SI) is formulated, which is given as

$$SI = \frac{i_{peak(ITSC)} - i_{peak(h)}}{i_{peak(h)}}, \tag{4.7}$$

where $i_{peak(ITSC)}$ and $i_{peak(h)}$ are the peak values for faulty and healthy conditions. Fig. 4.22 illustrates the severity plot that helps estimate the number of shorted turns. For ITSC, with SI falling between 0.8 and 1, the percentage of shorted turns can be estimated to be around 10 - 20%.

4.4 Loss & Torque investigation due to Injection

The introduction of high-frequency pulses for diagnostic purposes leads to supplementary losses and unwanted torque in the motor. This study delves into the analysis of copper losses and the resultant torque generated during the defined injection span of 5°. By disregarding the influence of back electromotive force and accounting for a negligible winding resistance (R_{ph}=0.6 Ω), alongside the presumption of minimal perturbation in inductance within the injection region, the pulse current $i_{pulse}(t)$ can be mathematically expressed as follows:

$$i_{pulse}(t) = \begin{cases} \frac{V_{dc}\times t}{L(\theta_1-\theta_2)}, & \text{for } 0 \rightarrow DT. \\ \frac{V_{dc}\times(2DT-t)}{L(\theta_1-\theta_2)}, & \text{for } DT \rightarrow 2DT. \\ 0, & \text{for } 2DT \rightarrow T. \end{cases} \tag{4.8}$$

where T is the pulse period (shown in Fig. 4.8), D is the duty ratio, V_{dc} is the dc link voltage, and $L(\theta_1$-$\theta_2)$ is the inductance within injection width. The average current in

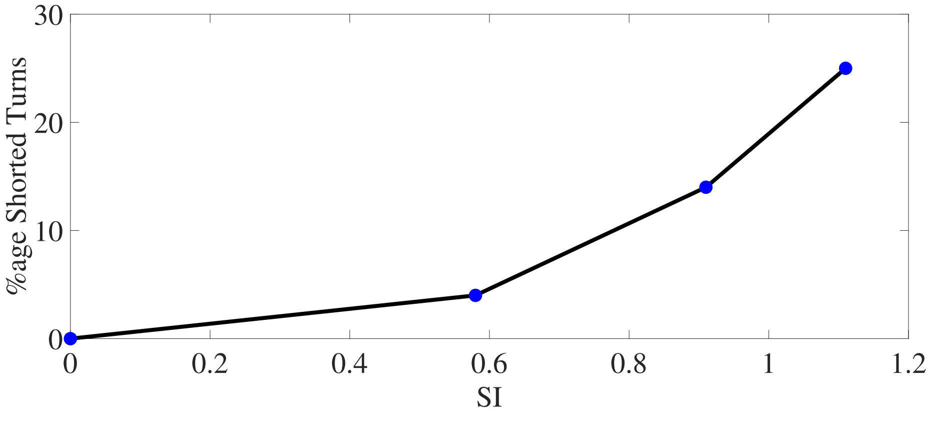

Figure 4.22: Severity plot between percentage shorted turns and severity index.

time T can be articulated as

$$I_{av} = \frac{\int_0^T i_{pulse}(t)dt}{T} = D^2 \frac{V_{dc}}{L(\theta_1 - \theta_2)} T. \tag{4.9}$$

Considering the injection width for one of the phases (phase A) between 34°-39°, the RMS current can be evaluated as

$$I_{rms} = \sqrt{\frac{1}{5}\int_{34}^{39} [D^2 \frac{V_{dc}}{L(\theta_1 - \theta_2)} T]^2 d\theta}. \tag{4.10}$$

Therefore, the copper loss within 34°-39° can be denoted as

$$P_c = \frac{V_{dc}^2 T^2 D^4 R_{ph}}{5} \int_{34}^{39} \frac{1}{L^2(\theta_1 - \theta_2)} d\theta. \tag{4.11}$$

The expression in (4.11) indicates that the copper loss (P_c) can be minimized by strategically choosing the injection frequency and pulse duty ratio while keeping other variables constant. Opting for a higher injection frequency and decreasing the duty ratio reduces the amplitude of pulse currents. In healthy conditions, the peak pulse current value is 0.34 A per phase when the injection frequency is set to 10 kHz, and the duty ratio is maintained below 0.5. Consequently, it can be inferred that such a pulse current magnitude, especially when compared to the load current within a narrower injection window, exerts a relatively minor impact on the overall losses.

Also, the maximum torque (T_m) generated as a result of injection in every pulse period can be represented as

$$T_m = \frac{1}{2}(\frac{V_{dc}}{L(\theta_1 - \theta_2)} DT)^2 \frac{dL(\theta_1 - \theta_2)}{d\theta}. \tag{4.12}$$

Although injection is done in the region where the rate of change in inductance is minimal, moreover, selecting a higher injection frequency and lowering the duty ratio ensures further minimization of the unwanted torque.

4.5 Conclusions

This chapter introduces a novel diagnostic approach for identifying ITSCs in SRMs. The proposed method involves the injection of high-frequency pulses into the motor phases around their respective unaligned rotor positions. The chapter delves into the foundational background and meticulously outlines the formulation, followed by experimental validation. The core concept revolves around translating variations in inductance due to ITSCs through the application of high-frequency pulses. The method strategically utilizes the low torque flat inductance zone around the respective unaligned rotor position. This region exhibits minimal inductance alterations, minimizing the undesired torque generation during the pulse injection. Moreover, the injection frequency within a confined width is selected to ensure that the magnitude of the ensuing pulse current does not lead to substantial motor losses. Since diagnostic pulses are introduced into the phases during non-active torque production intervals, the method operates independently of the control mechanism. As a result, it remains adaptable for SRMs operating under various control strategies. This method exhibits higher sensitivity for detecting even minor ITSCs and boasts robust reliability when subjected to load and speed fluctuations. The technique has a good transient response and works efficiently under load/speed variations during the transition period. The method offers fast diagnosis without necessitating complex computations employing a basic comparative logic approach within the time domain. Importantly, the technique requires no supplementary hardware beyond the foundational drive structure, thus offering an efficient and streamlined approach to diagnosis.

Chapter 5

Conclusion & Future Scope

5.1 Conclusions

Chapter 1 of the thesis discusses the importance of the requirement of the fault management system for the reliable operation of electric machines. The basics of SRMs, their comparison with the conventional motors and possible faults are presented in detail. An exhaustive literature on short circuit faults and their consequences on the performance of SRM has been included. The need for diagnosis techniques for ITSCs in SRMs that account for 21% of all electrical faults is also highlighted. Also, in-depth literature has been incorporated regarding the comparative study of the available techniques for ITSCs in traditional motors like IMs and PMSMs, highlighting their features and research gaps in the techniques available for SRMs. The thesis objectives have been drawn to fill the research gaps and develop sophisticated diagnosis techniques for ITSCs to make SRM technology more reliable and adaptable. Chapter 2 of the thesis deals with the first objective, which targets a diagnosis technique for ITSCs in SRMs for low and medium-speed applications operating under chopped current control. The effect of the ITSCs on the performance of SRM operating under CCC mode has been portrayed in detail using FEM and experimental analysis. The background of the proposed method based on monitoring post turn-off current in the flat inductance zone around aligned rotor positions has been thoroughly discussed. The easy implementation and robustness of the proposed method under different operating and transient conditions have been validated by experimentation on the test rig of 8/6 SRM. The technique offers higher sensitivity regarding the least severity detected (ITSCs of 4% shorted turns in a phase). Chapter 3 of the thesis deals with the second objective, which targets a diagnosis technique for ITSCs in SRMs independent of control strategies. The technique has been developed employing an additional circuitry that injects a high-frequency voltage signal into the idle phases. Utilizing the auxiliary circuit and idle phase for injection decouples the diagnosis technique from the control. The proposed method has been validated and demonstrated experimentally for CCC and APC; however, as it decoupled from current profiling, it can also be applied to SRMs operating on advanced control techniques. The method offers superior performance, be it severity (ITSC of 2 turns is detected) and reliability under different operating and transient conditions, but at the price of increased complexity and cost to the traditional SRM drive. Chapter 4 of the thesis deals with the third objective and focuses on eliminating the complexity involved in the second objective without compromising the features of any sophisticated fault diagnosis system. The fault is diagnosed by analyzing the behavior of the pulsed current injected by operating the phases at a high frequency in the flat inductance zone around the unaligned rotor positions. The proposed technique applies to SRMs independent of control strategies. Also, the robustness of the proposed scheme has been demonstrated experimentally by subjecting the motor to abrupt speed/load change, proving its higher reliability. It also offers a higher sensitivity to ITSCs of fewer turns. No additional hardware is used for diagnosis and decision-making, reducing the complexity and cost.

5.2 Future Scope

The thesis proposes three diagnosis strategies for ITSCs in SRMs to make the technology more reliable and adaptable in various safety-critical applications. The three methods discussed in the thesis have capabilities that can be further exploited to harness other important outcomes. The future scope of the work is discussed here.

All three proposed methods discussed in the thesis have been formulated to translate the variation in inductance due to ITSCs in SRMs. As mentioned, the effect of eccentricity faults on the inductance is quite opposite to that of ITSCs depicted in Figure 4.6. It can be observed that the inductance of the faulty phase due to eccentricity increases compared to the healthy motor. These faults (static, dynamic & mixed eccentricity) can be identified using the three proposed methods, which are explained here:

1) The post turn-off phase currents are monitored for diagnosing the ITSC, as discussed in Chapter 2. The decay time of the phase currents in the flat inductance zone, which reduces due to the increase in inductance due to ITSCs, is evaluated in terms of pulses for the duration equivalent to the decay time. However, with the increase in the inductance due to eccentricity, the target decay time will reduce compared to the healthy condition. The effect on the decay time is quite the opposite for both eccentricity and ITSCs; hence, eccentricity faults can be easily identified using the proposed technique.

2) A high-frequency voltage signal is injected into the negative torque region of inactive phases to translate the inductance variation, as discussed in Chapter 3. The peak value of the high-frequency current increases due to the reduction in the inductance of the phase suffering from ITSC. However, due to eccentricity, the peak of the high-frequency current corresponding to the faulty phase would reduce due to a reduction in inductance. Therefore, the method can be applied to SRMs to identify eccentricity defects effectively.

3) The motor phases are switched at a high frequency around their respective unaligned rotor positions to diagnose the ITSC, as discussed in Chapter 4. Also, it can be observed from Figure 4.6 that there is no variation in the inductance due to the eccentricity fault around the unaligned rotor positions. However, with a minor change in logic, operating

the phases at a high frequency in their negative torque region can be used to identify eccentricity faults.

The proposed methods have been analyzed and validated for ITSCs in SRMs, and the fault indicators have been devised accordingly. The behavior of the fault indicators under other fault conditions and multiple fault scenarios needs to be analyzed to identify and distinguish the type of faults. It would help the SRMs to be more reliable and adaptable in various safety-critical applications.

The proposed techniques discussed in Chapters 3 & 4 can also be extended and accompanied by the sensor-less techniques based on signal injection, making the sensor-less techniques tolerant to faults, thereby enhancing the fault resilience of SRMs.

References

[1] R. Krishnan, *Switched Reluctance Motor Drives: Modeling, Simulation, Analysis, Design, and Applications*, ser. Industrial Electronics. CRC Press, 2017.

[2] T. Miller, *Switched Reluctance Motors and Their Control*, ser. Monographs in electrical and electronic engineering. Magna Physics, 1993.

[3] K. Chau, *Electric Vehicle Machines and Drives: Design, Analysis and Application*, ser. IEEE Press. Wiley, 2015.

[4] C. Gan, Y. Chen, R. Qu, Z. Yu, W. Kong, and Y. Hu, "An overview of fault-diagnosis and fault-tolerance techniques for switched reluctance machine systems," *IEEE Access*, vol. 7, pp. 174 822–174 838, 2019.

[5] B. Lequesne, S. Gopalakrishnan, and A. Omekanda, "Winding short circuits in the switched reluctance drive," *IEEE Transactions on Industry Applications*, vol. 41, no. 5, pp. 1178–1184, 2005.

[6] N. Ali, Q. Gao, C. Xu, P. Makys, and M. Stulrajter, "Fault diagnosis and tolerant control for power converter in srm drives," *The Journal of Engineering*, vol. 2018, no. 13, pp. 546–551, 2018.

[7] J. F. Marques, J. O. Estima, N. S. Gameiro, and A. J. Marques Cardoso, "A new diagnostic technique for real-time diagnosis of power converter faults in switched reluctance motor drives," *IEEE Transactions on Industry Applications*, vol. 50, no. 3, pp. 1854–1860, 2014.

[8] G. Han, H. Chen, and G. Guan, "Generalised fault diagnostic method for power transistors in asymmetric half-bridge power converter of srm drive," *IET Electric Power Applications*, vol. 13, no. 2, pp. 168–180, 2019.

[9] J. Gan, K. Chau, C. Chan, and J. Jiang, "A new surface-inset, permanent-magnet, brushless dc motor drive for electric vehicles," *IEEE Transactions on Magnetics*, vol. 36, no. 5, pp. 3810–3818, 2000.

[10] J. Nerg, M. Rilla, V. Ruuskanen, J. Pyrhönen, and S. Ruotsalainen, "Direct-driven interior magnet permanent-magnet synchronous motors for a full electric sports car," *IEEE Transactions on Industrial Electronics*, vol. 61, no. 8, pp. 4286–4294, 2014.

[11] K. T. Chau, C. C. Chan, and C. Liu, "Overview of permanent-magnet brushless drives for electric and hybrid electric vehicles," *IEEE Transactions on Industrial Electronics*, vol. 55, no. 6, pp. 2246–2257, 2008.

[12] S. Sadeghi, L. Guo, H. A. Toliyat, and L. Parsa, "Wide operational speed

range of five-phase permanent magnet machines by using different stator winding configurations," *IEEE Transactions on Industrial Electronics*, vol. 59, no. 6, pp. 2621–2631, 2012.

[13] K. Kiyota, H. Sugimoto, and A. Chiba, "Comparing electric motors: An analysis using four standard driving schedules," *IEEE Industry Applications Magazine*, vol. 20, no. 4, pp. 12–20, 2014.

[14] A. Chiba and K. Kiyota, "Review of research and development of switched reluctance motor for hybrid electrical vehicle," in *2015 IEEE Workshop on Electrical Machines Design, Control and Diagnosis (WEMDCD)*, 2015, pp. 127–131.

[15] J. Lin, N. Schofield, and A. Emadi, "External-rotor $6-10$ switched reluctance motor for an electric bicycle," *IEEE Transactions on Transportation Electrification*, vol. 1, no. 4, pp. 348–356, 2015.

[16] D. Gerada, A. Mebarki, N. L. Brown, C. Gerada, A. Cavagnino, and A. Boglietti, "High-speed electrical machines: Technologies, trends, and developments," *IEEE Transactions on Industrial Electronics*, vol. 61, no. 6, pp. 2946–2959, 2014.

[17] D. G. Dorrell, A. M. Knight, M. Popescu, L. Evans, and D. A. Staton, "Comparison of different motor design drives for hybrid electric vehicles," in *2010 IEEE Energy Conversion Congress and Exposition*, 2010, pp. 3352–3359.

[18] K. Kiyota and A. Chiba, "Design of switched reluctance motor competitive to 60-kw ipmsm in third-generation hybrid electric vehicle," *IEEE Transactions on Industry Applications*, vol. 48, no. 6, pp. 2303–2309, 2012.

[19] E. Bostanci, M. Moallem, A. Parsapour, and B. Fahimi, "Opportunities and challenges of switched reluctance motor drives for electric propulsion: A comparative study," *IEEE Transactions on Transportation Electrification*, vol. 3, no. 1, pp. 58–75, 2017.

[20] S. Vukosavic and V. Stefanovic, "Srm inverter topologies: a comparative evaluation," *IEEE Transactions on Industry Applications*, vol. 27, no. 6, pp. 1034–1047, 1991.

[21] S. Gopalakrishnan, A. Omekanda, and B. Lequesne, "Classification and remediation of electrical faults in the switched reluctance drive," *IEEE Transactions on Industry Applications*, vol. 42, no. 2, pp. 479–486, 2006.

[22] C. Stephens, "Fault detection and management system for fault-tolerant switched reluctance motor drives," *IEEE Transactions on Industry Applications*, vol. 27, no. 6, pp. 1098–1102, 1991.

[23] V. Sharma, S. Murthy, and B. Singh, "Analysis of switched reluctance motor drive under fault conditions," in *Conference Record of 1998 IEEE Industry Applications Conference. Thirty-Third IAS Annual Meeting (Cat. No.98CH36242)*, vol. 1, 1998, pp. 553–562 vol.1.

[24] C. Gan, J. Wu, S. Yang, Y. Hu, W. Cao, and J. Si, “Fault diagnosis scheme for open-circuit faults in switched reluctance motor drives using fast fourier transform algorithm with bus current detection,” *IET Power Electronics*, vol. 9, no. 1, pp. 20–30, 2016.

[25] L. Xiao, H. Sun, F. Gao, S. Hou, and L. Li, “A new diagnostic method for winding short-circuit fault for srm based on symmetrical component analysis,” *Chinese Journal of Electrical Engineering*, vol. 4, no. 1, pp. 74–82, 2018.

[26] P. Bogusz, M. Korkosz, and J. Prokop, “Current harmonics analysis as a method of electrical faults diagnostic in switched reluctance motors,” in *2007 IEEE International Symposium on Diagnostics for Electric Machines, Power Electronics and Drives*, 2007, pp. 426–431.

[27] B. Ilhem, B. Amar, A. Lebaroud, and R. Fares, “Automatic fault diagnosis of fault tolerant power converter for switched reluctance motor based on time-frequency technique,” in *2014 16th International Power Electronics and Motion Control Conference and Exposition*, 2014, pp. 1234–1240.

[28] H. Chen, C. Fang, J. Dong, S. Lu, V. Pires, J. Martins, and M. P. Aguirre, “Diagnosis of interturn short-circuit of srm based on ratio of current components,” *IEEE Transactions on Transportation Electrification*, vol. 9, no. 2, pp. 3319–3327, 2023.

[29] C. Gan, J. Wu, S. Yang, Y. Hu, and W. Cao, “Wavelet packet decomposition-based fault diagnosis scheme for srm drives with a single current sensor,” *IEEE Transactions on Energy Conversion*, vol. 31, no. 1, pp. 303–313, 2016.

[30] S. R. Khayam Hoseini, E. Farjah, T. Ghanbari, and H. Givi, “Extended kalman filter-based method for inter-turn fault detection of the switched reluctance motors,” *IET Electric Power Applications*, vol. 10, no. 8, pp. 714–722, 2016.

[31] H.-S. Ro, D.-H. Kim, H.-G. Jeong, and K.-B. Lee, “Tolerant control for power transistor faults in switched reluctance motor drives,” *IEEE Transactions on Industry Applications*, vol. 51, no. 4, pp. 3187–3197, 2015.

[32] D. S. B. Fonseca and A. J. M. Cardoso, “On-line inter-turn short-circuit fault diagnosis in switched reluctance motors,” *2019 IEEE International Electric Machines & Drives Conference (IEMDC)*, pp. 198–202, 2019.

[33] G. Han, H. Chen, X. Shi, and Y. Wang, “Phase current reconstruction strategy for switched reluctance machines with fault-tolerant capability,” *IET Electric Power Applications*, vol. 11, no. 3, pp. 399–411, 2017.

[34] N. S. Gameiro and A. J. Marques Cardoso, “A new method for power converter fault diagnosis in srm drives,” *IEEE Transactions on Industry Applications*, vol. 48, no. 2, pp. 653–662, 2012.

[35] H. Torkaman, E. Afjei, and P. Yadegari, “Static, dynamic, and mixed eccentricity faults diagnosis in switched reluctance motors using transient finite element method and experiments,” *IEEE Transactions on Magnetics*, vol. 48, no. 8, pp. 2254–2264, 2012.

[36] P. Zhang, K. Li, S. Yu, and D. Yu, “A novel fault diagnosis technique of interturn short-circuit fault for srm in current chopper mode,” *IEEE Transactions on Industrial Electronics*, vol. 69, no. 3, pp. 3037–3046, 2022.

[37] N. Ali, Q. Wang, Q. Gao, and K. Ma, “Fast detection of power transistor faults in srm drives based on transient pulse injection,” *IEEE Journal of Emerging and Selected Topics in Power Electronics*, pp. 1–1, 2023.

[38] J. Faiz and S. Pakdelian, “Diagnosis of static eccentricity in switched reluctance motors based on mutually induced voltages,” *IEEE Transactions on Magnetics*, vol. 44, no. 8, pp. 2029–2034, 2008.

[39] W. Yang, B. Gou, Y. Lei, and J. Wang, “Short switch fault diagnosis method for power converter using a model-based approach in switched reluctance motor drives,” *The Journal of Engineering*, vol. 2019, no. 16, pp. 2137–2141, 2019.

[40] H.-U. Shin and K.-B. Lee, “Fault diagnosis method for power transistors in switched reluctance machine drive system,” in *2016 IEEE 8th International Power Electronics and Motion Control Conference (IPEMC-ECCE Asia)*, 2016, pp. 2481–2486.

[41] G. Han, H. Chen, and X. Shi, “Modelling, diagnosis, and tolerant control of phase-to-phase fault in switched reluctance machine,” *IET Electric Power Applications*, vol. 11, no. 9, pp. 1527–1537, 2017.

[42] J. F. Marques, J. O. Estima, N. S. Gameiro, and A. J. Marques Cardoso, “A new diagnostic technique for real-time diagnosis of power converter faults in switched reluctance motor drives,” *IEEE Transactions on Industry Applications*, vol. 50, no. 3, pp. 1854–1860, 2014.

[43] H. Torkaman and E. Afjei, “Comprehensive detection of eccentricity fault in switched reluctance machines using high-frequency pulse injection,” *IEEE Transactions on Power Electronics*, vol. 28, no. 3, pp. 1382–1390, 2013.

[44] C. Caicedo-Narvaez, Y. Li, L. Maharjan, E. Cosoroaba, B. Fahimi, M. Kiani, and M. Moallem, “Thermal signature analysis of an 8/6 switched reluctance motor under inter-turn short circuit fault,” in *2018 IEEE International Conference on Industrial Technology (ICIT)*, 2018, pp. 1859–1864.

[45] J.-H. Jung, J.-J. Lee, and B.-H. Kwon, “Online diagnosis of induction motors using mcsa,” *IEEE Transactions on Industrial Electronics*, vol. 53, no. 6, pp. 1842–1852, 2006.

[46] J. Sottile, F. Trutt, and J. Kohler, “Condition monitoring of stator windings in

induction motors. ii. experimental investigation of voltage mismatch detectors," *IEEE Transactions on Industry Applications*, vol. 38, no. 5, pp. 1454–1459, 2002.

[47] H. Henao, C. Demian, and G.-A. Capolino, "A frequency-domain detection of stator winding faults in induction machines using an external flux sensor," in *Conference Record of the 2002 IEEE Industry Applications Conference. 37th IAS Annual Meeting (Cat. No.02CH37344)*, vol. 3, 2002, pp. 1511–1516 vol.3.

[48] J. CusidÓCusido, L. Romeral, J. A. Ortega, J. A. Rosero, and A. GarcÍaGarcia Espinosa, "Fault detection in induction machines using power spectral density in wavelet decomposition," *IEEE Transactions on Industrial Electronics*, vol. 55, no. 2, pp. 633–643, 2008.

[49] C. H. De Angelo, G. R. Bossio, S. J. Giaccone, M. I. Valla, J. A. Solsona, and G. O. Garcia, "Online model-based stator-fault detection and identification in induction motors," *IEEE Transactions on Industrial Electronics*, vol. 56, no. 11, pp. 4671–4680, 2009.

[50] A. Alloui, K. Laadjal, M. Sahraoui, and A. J. Marques Cardoso, "Online interturn short-circuit fault diagnosis in induction motors operating under unbalanced supply voltage and load variations, using the stlsp technique," *IEEE Transactions on Industrial Electronics*, vol. 70, no. 3, pp. 3080–3089, 2023.

[51] S. Bachir, S. Tnani, J.-C. Trigeassou, and G. Champenois, "Diagnosis by parameter estimation of stator and rotor faults occurring in induction machines," *IEEE Transactions on Industrial Electronics*, vol. 53, no. 3, pp. 963–973, 2006.

[52] V. Nguyen, D. Wang, J. Seshadrinath, S. Nadarajan, and V. Vaiyapuri, "Fault severity estimation using nonlinear kalman filter for induction motors under inter-turn fault," in *IECON 2016 - 42nd Annual Conference of the IEEE Industrial Electronics Society*, 2016, pp. 1488–1493.

[53] V. Nguyen, D. Wang, J. Seshadrinath, A. Ukil, M. S. Krishna, S. Nadarajan, and V. Vaiyapuri, "A method for incipient interturn fault detection and severity estimation of induction motors under inherent asymmetry and voltage imbalance," *IEEE Transactions on Transportation Electrification*, vol. 3, no. 3, pp. 703–715, 2017.

[54] M. B. K. Bouzid, G. Champenois, N. M. Bellaaj, L. Signac, and K. Jelassi, "An effective neural approach for the automatic location of stator interturn faults in induction motor," *IEEE Transactions on Industrial Electronics*, vol. 55, no. 12, pp. 4277–4289, 2008.

[55] J. Seshadrinath, B. Singh, and B. K. Panigrahi, "Vibration analysis based interturn fault diagnosis in induction machines," *IEEE Transactions on Industrial Informatics*, vol. 10, no. 1, pp. 340–350, 2014.

[56] R. R. Kumar, V. Randazzo, G. Cirrincione, M. Cirrincione, E. Pasero, A. Tortella, and

M. Andriollo, "Induction machine stator fault tracking using the growing curvilinear component analysis," *IEEE Access*, vol. 9, pp. 2201–2212, 2021.

[57] A. K. Das, S. Das, A. K. Pradhan, B. Chatterjee, and S. Dalai, "Rpcnnet: A deep learning approach to sense minor stator winding interturn fault severity in induction motor under variable load condition," *IEEE Sensors Journal*, vol. 23, no. 4, pp. 3965–3972, 2023.

[58] J. Hang, S. Ding, J. Zhang, M. Cheng, W. Chen, and Q. Wang, "Detection of interturn short-circuit fault for pmsm with simple fault indicator," *IEEE Transactions on Energy Conversion*, vol. 31, no. 4, pp. 1697–1699, 2016.

[59] J. Hang, J. Zhang, M. Xia, S. Ding, and W. Hua, "Interturn fault diagnosis for model-predictive-controlled-pmsm based on cost function and wavelet transform," *IEEE Transactions on Power Electronics*, vol. 35, no. 6, pp. 6405–6418, 2020.

[60] S. Moon, H. Jeong, H. Lee, and S. W. Kim, "Interturn short fault diagnosis in a pmsm by voltage and current residual analysis with the faulty winding model," *IEEE Transactions on Energy Conversion*, vol. 33, no. 1, pp. 190–198, 2018.

[61] K.-H. Kim, "Simple online fault detecting scheme for short-circuited turn in a pmsm through current harmonic monitoring," *IEEE Transactions on Industrial Electronics*, vol. 58, no. 6, pp. 2565–2568, 2011.

[62] H. Jeong, S. Moon, and S. W. Kim, "An early stage interturn fault diagnosis of pmsms by using negative-sequence components," *IEEE Transactions on Industrial Electronics*, vol. 64, no. 7, pp. 5701–5708, 2017.

[63] J. Hang, W. Sun, Q. Hu, X. Ren, and S. Ding, "Integration of interturn fault diagnosis and fault-tolerant control for pmsm drive system," *IEEE Transactions on Transportation Electrification*, vol. 8, no. 2, pp. 2825–2835, 2022.

[64] M. A. Mazzoletti, G. R. Bossio, C. H. De Angelo, and D. R. Espinoza-Trejo, "A model-based strategy for interturn short-circuit fault diagnosis in pmsm," *IEEE Transactions on Industrial Electronics*, vol. 64, no. 9, pp. 7218–7228, 2017.

[65] J. Zhang, Y. Wang, K. Zhu, Y. Zhang, and Y. Li, "Diagnosis of interturn short-circuit faults in permanent magnet synchronous motors based on few-shot learning under a federated learning framework," *IEEE Transactions on Industrial Informatics*, vol. 17, no. 12, pp. 8495–8504, 2021.

[66] Q. Song, M. Wang, W. Lai, and S. Zhao, "On bayesian optimization-based residual cnn for estimation of inter-turn short circuit fault in pmsm," *IEEE Transactions on Power Electronics*, vol. 38, no. 2, pp. 2456–2468, 2023.

[67] Q. Wu and S. Nandi, "Fast single-turn sensitive stator inter-turn fault detection of induction machines based on positive and negative sequence third harmonic

components of line currents," in *2008 IEEE Industry Applications Society Annual Meeting*, 2008, pp. 1–8.

[68] W. Thomson and M. Fenger, "Current signature analysis to detect induction motor faults," *IEEE Industry Applications Magazine*, vol. 7, no. 4, pp. 26–34, 2001.

[69] A. M. da Silva, R. J. Povinelli, and N. A. O. Demerdash, "Induction machine broken bar and stator short-circuit fault diagnostics based on three-phase stator current envelopes," *IEEE Transactions on Industrial Electronics*, vol. 55, pp. 1310–1318, 2008.

[70] S. M. A. Cruz and A. J. M. Cardoso, "Multiple reference frames theory: a new method for the diagnosis of stator faults in three-phase induction motors," *IEEE Transactions on Energy Conversion*, vol. 20, pp. 611–619, 2005.

[71] S. Cheng, P. Zhang, and T. G. Habetler, "An impedance identification approach to sensitive detection and location of stator turn-to-turn faults in a closed-loop multiple-motor drive," *IEEE Transactions on Industrial Electronics*, vol. 58, no. 5, pp. 1545–1554, 2011.

[72] P. Neti and S. Nandi, "Stator interturn fault detection of synchronous machines using field current and rotor search-coil voltage signature analysis," *IEEE Transactions on Industry Applications*, vol. 45, no. 3, pp. 911–920, 2009.

[73] H. Henao, C. Demian, and G.-A. Capolino, "A frequency-domain detection of stator winding faults in induction machines using an external flux sensor," *IEEE Transactions on Industry Applications*, vol. 39, no. 5, pp. 1272–1279, 2003.

[74] T. M. Wolbank, K. A. Loparo, and R. Wohrnschimmel, "Inverter statistics for online detection of stator asymmetries in inverter-fed induction motors," *IEEE Transactions on Industry Applications*, vol. 39, pp. 1102–1108, 2003.

[75] F. Briz, M. Degner, A. Zamarron, and J. Guerrero, "Online stator winding fault diagnosis in inverter-fed ac machines using high-frequency signal injection," *IEEE Transactions on Industry Applications*, vol. 39, no. 4, pp. 1109–1117, 2003.

[76] B. Mirafzal, R. J. Povinelli, and N. A. O. Demerdash, "Interturn fault diagnosis in induction motors using the pendulous oscillation phenomenon," *IEEE Transactions on Energy Conversion*, vol. 21, no. 4, pp. 871–882, 2006.

[77] C. H. De Angelo, G. R. Bossio, S. J. Giaccone, M. I. Valla, J. A. Solsona, and G. O. Garcia, "Online model-based stator-fault detection and identification in induction motors," *IEEE Transactions on Industrial Electronics*, vol. 56, no. 11, pp. 4671–4680, 2009.

[78] R. Tallam, T. Habetler, and R. Harley, "Continual on-line training of neural networks with applications to electric machine fault diagnostics," in *2001 IEEE 32nd Annual*

Power Electronics Specialists Conference (IEEE Cat. No.01CH37230), vol. 4, 2001, pp. 2224–2228 vol. 4.

[79] M. S. Ballal, Z. J. Khan, H. M. Suryawanshi, and R. L. Sonolikar, “Adaptive neural fuzzy inference system for the detection of inter-turn insulation and bearing wear faults in induction motor,” *IEEE Transactions on Industrial Electronics*, vol. 54, no. 1, pp. 250–258, 2007.

[80] W. Xu-hong and H. Yi-gang, “Fuzzy neural network based on-line stator winding turn fault detection for induction motors,” in *2007 2nd IEEE Conference on Industrial Electronics and Applications*, 2007, pp. 2461–2464.

[81] K.-H. Kim, “Simple online fault detecting scheme for short-circuited turn in a pmsm through current harmonic monitoring,” *IEEE Transactions on Industrial Electronics*, vol. 58, no. 6, pp. 2565–2568, 2011.

[82] J. Rosero, L. Romeral, J. Cusido, A. Garcia, and J. Ortega, “On the short-circuiting fault detection in a pmsm by means of stator current transformations,” in *2007 IEEE Power Electronics Specialists Conference*, 2007, pp. 1936–1941.

[83] J. Chai, J. Wang, K. Atallah, and D. Howe, “Performance comparison and winding fault detection of duplex 2-phase and 3-phase fault-tolerant permanent magnet brushless machines,” in *2007 IEEE Industry Applications Annual Meeting*, 2007, pp. 566–572.

[84] C. Bianchini, E. Fornasiero, T. N. Matzen, N. Bianchi, and A. Bellini, “Fault detection of a five-phase permanent-magnet machine,” in *2008 34th Annual Conference of IEEE Industrial Electronics*, 2008, pp. 1200–1205.

[85] M. Awadallah, M. Morcos, S. Gopalakrishnan, and T. Nehl, “A neuro-fuzzy approach to automatic diagnosis and location of stator inter-turn faults in csi-fed pm brushless dc motors,” *IEEE Transactions on Energy Conversion*, vol. 20, no. 2, pp. 253–259, 2005.

[86] H. Chen, G. Han, W. Yan, S. Lu, and Z. Chen, “Modeling of a switched reluctance motor under stator winding fault condition,” *IEEE Transactions on Applied Superconductivity*, vol. 26, no. 4, pp. 1–6, 2016.

[87] A. Miremadi, H. Torkaman, and A. Siadatan, “Maximum current point tracking for stator winding short circuits diagnosis in switched reluctance motor,” in *4th Annual International Power Electronics, Drive Systems and Technologies Conference*, 2013, pp. 83–87.

Chapter A

Appendix

A.1 Threshold determination

The thresholds for identifying the fault using the proposed techniques discussed in Chapters 3 & 4 have been decided empirically by performing FEM analysis. The threshold factor (y) in Chapter 3 is defined by analyzing the high-frequency currents produced in the winding due to injection. The currents for healthy and ITSC of 2 turns are presented in Figure A.1. The peak values for healthy and faulty conditions ($i_{peak(h)}$ and $i_{peak(f1)}$) are 8.1 mA and 5.3 mA, respectively. The percentage change in the peak values for the case mentioned is around 50%. This deviation is large enough to decide a threshold factor. We have set a threshold value of 20% more than the peak value for healthy winding conditions. Therefore, the value of the threshold factor (y) is 1.2. 3.2 V is the peak value appearing for the healthy case in the experimental analysis under CCC, and the threshold voltage is set to 3.8 V, which is approximately 1.2 times 3.2 V. The threshold value can be defined at the time of installation of the diagnosis system in the drive after testing that SR motor. Similarly, the threshold value in Chapter 4 is defined by analyzing the high-frequency currents produced in the winding due to injection in the finite element analysis of the test motor. The currents for healthy and ITSC of 4 turns are presented in Figure A.2. The peak values for healthy and faulty conditions ($i_{peak(h)}$ and $i_{peak(f)}$) are 0.33 A and 0.52 A, respectively. The percentage change in the peak values for the case mentioned is around 50%. This deviation is large enough to decide a threshold factor. We have set a threshold

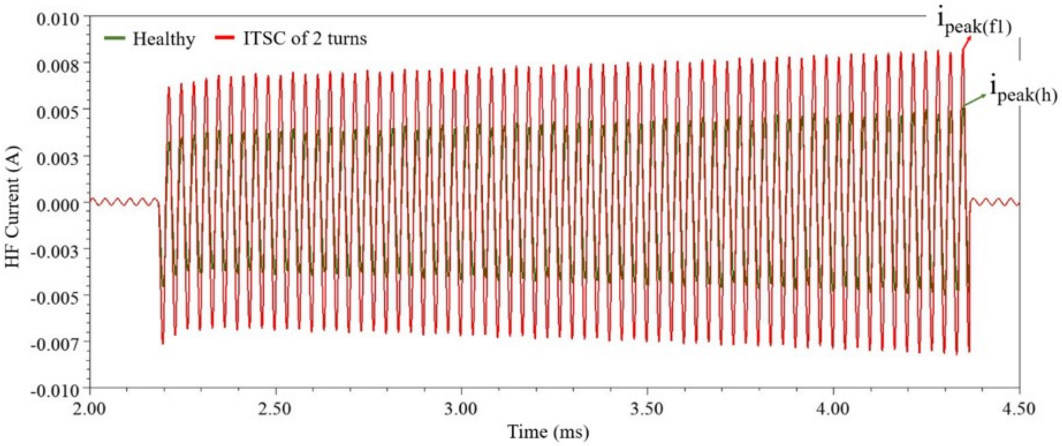

Figure A.1: High-frequency current for healthy and ITSC of 2 turns.

value of 40% more than the peak value for healthy winding conditions. The threshold value can be defined at the time of installation of the diagnosis system after the finite element analysis of the motor.

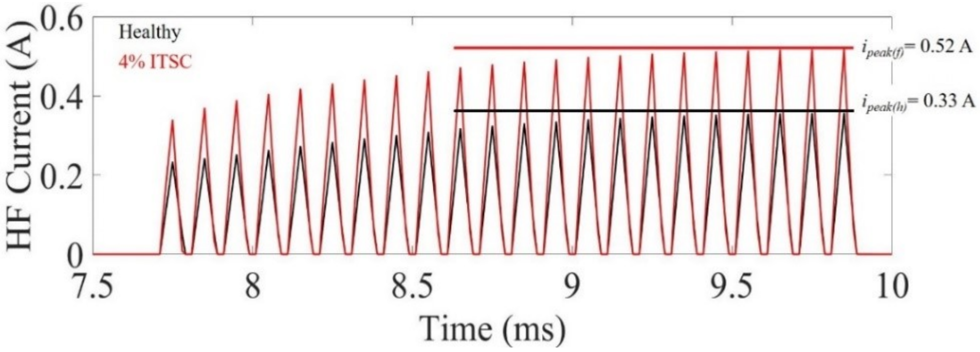

Figure A.2: High-frequency current for healthy and ITSC of 4 turns.

A.2 Simplified fault flags

It can be observed that the fault flags in Chapter 3 & 4 keep toggling between 0 & 1 for the entire fault duration. A simplified phase fault flags can be displayed in various ways, such as using light-emitting diodes, SR flip-flops, or a moving average. In this representation, a high state (3V) indicates faulty period, while a low state (0V) signifies normal, fault-free operation. To simplify the fault flag for our test motors, the moving average of the phase fault flags demonstrated earlier have been evaluated. This simplified

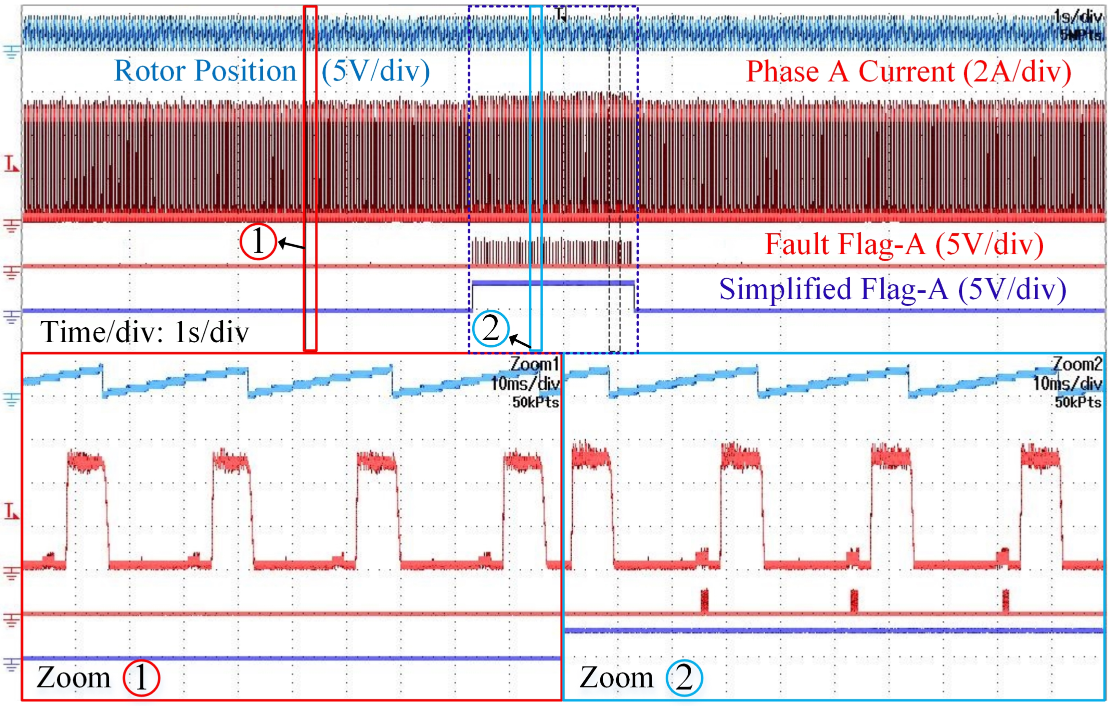

Figure A.3: Simplified fault flag acquiring a high state (3 V) during the entire fault duration and a low state (0 V) for fault-free operation.

flag is shown in Figure A.3. Notably, this simplified flag remains in the high state as long as the fault persists and switches to zero once the fault has been cleared.